

ISSET JOURNAL OF EARTHQUAKE TECHNOLOGY

Vol. 48

No. 1

March 2011

CONTENTS

| No. | Paper | Page |
|------------|---|-------------|
| 513 | Deformation of a Uniform Half-Space with Rigid Boundary due to a Long Tensile Fault Jagdish Singh, Meenal Malik and Mahabir Singh | 1 |
| 514 | Health Assessment of Structures Exposed to Seismic Excitations Ajoy Kumar Das and Achintya Haldar | 11 |
| 515 | Investigation and Analysis of Seismic Wave Parameters of Seismic Gap, Seismic Belt and Foreshock Wenlong Liu, Yucheng Liu, Yonglin Xu, Chun Zhang, Huan Zhang, Weidong Shen and Weixing Zhong | 29 |

Financial Assistance from AICTE and DST, New Delhi for the Publication of ISET Journals for 2010–2011 is duly acknowledged.

DEFORMATION OF A UNIFORM HALF-SPACE WITH RIGID BOUNDARY DUE TO A LONG TENSILE FAULT

Jagdish Singh*, Meenal Malik** and Mahabir Singh***

*Department of Mathematics

Maharshi Dayanand University, Rohtak-124001

**Department of Applied Sciences

Matu Ram Institute of Engineering and Management, Rohtak-124001

***Controller of Examinations

Deenbandhu Chhotu Ram University of Science and Technology, Murthal, Sonapat-139031

ABSTRACT

The Airy stress function for a long tensile fault of arbitrary dip and finite width buried in a homogeneous, isotropic, perfectly elastic half-space with rigid boundary is obtained. This Airy stress function is used to derive closed-form analytical expressions for the stresses at an arbitrary point of the half-space with rigid boundary caused by a long vertical tensile fault of finite width. The variation of the stress fields with distance from the fault and depth is studied numerically.

KEYWORDS: Half-Space, Long Tensile Fault, Airy Stress Function, Rigid Boundary

INTRODUCTION

Steketee (1958) first made use of the elastic theory of dislocations to obtain the displacement and stress fields of a strike-slip fault. Following this fundamental study, numerous theoretical formulations describing the deformation of an isotropic, homogeneous, semi-infinite medium have been developed. Okada (1985) presented analytical expressions for the surface displacements, strains and tilts due to inclined shear and tensile faults in a half-space for both point and finite rectangular sources. Okada (1992) extended these results to internal deformation.

The tensile-fault representation has several very important geophysical applications, such as modelling of the deformation field due to a dyke injection in the volcanic region, mine collapse, or fluid-driven cracks. Moreover, several studies have shown that a large number of earthquake sources cannot be represented by the double-couple source mechanism which models a shear fault. Dziewonski and Woodhouse (1983) obtained the 'centroid-moment tensor' solutions for 201 moderate and large earthquakes and observed that the shallow earthquakes north of New Guinea and along the Solomon Islands showed systematic and substantial departures from the double-couple mechanism. Barker and Langston (1983) observed that the inversion of long-period teleseismic P and SH waves, for the 25 and 27 May 1980 Mammoth Lakes, California, earthquakes, yielded moment tensors with large non-double-couple components. According to Julian (1983) and Sipkin (1986), the non-double-couple mechanism might be due to the tensile failure under high fluid pressure. Therefore, it is important to study the elastic field of a tensile dislocation. For a complete description of the elastic field of an earthquake source, using the elastic dislocation theory, it is necessary to consider all the three components, namely, strike-slip, dip-slip and tensile. While the strike-slip and dip-slip cases have been discussed extensively in the seismological literature, tensile dislocation has received comparatively less attention.

Maruyama (1964) obtained surface displacements due to vertical and horizontal rectangular tensile faults in a semi-infinite Poisson solid. Davis (1983) derived an expression of the vertical displacement due to an inclined tensile fault in a half-space and showed that this model can approximate well a tensile crack, just as shear dislocations are successfully used to approximate the deformation fields by shear cracks. Yang and Davis (1986) obtained closed analytical expressions for the displacements, strains and stresses due to a rectangular inclined tensile fault in an elastic half-space.

Singh and Garg (1986) obtained integral expressions for the Airy stress function in an unbounded medium due to various two-dimensional sources. Beginning with these results, Rani et al. (1991) obtained closed-form analytical expressions for the Airy stress function, displacements and stresses in a homogeneous, isotropic, perfectly elastic half-space due to an arbitrary line source. By integrating over

the width of the fault, Rani and Singh (1992) obtained expressions for the Airy stress function, displacements and stresses in a uniform half-space due to a long dip-slip fault of finite width. Recently Piombo et al. (2007) studied the displacement, strain and stress fields due to shear and tensile dislocations in a viscoelastic half-space.

It is useful to consider the effect of material discontinuities on the elastic field due to a tensile dislocation. The simplest model to consider the effect of a material discontinuity is that of a tensile dislocation in an elastic half-space (say, medium 1 with rigidity μ_1) in contact with another elastic half-space (say, medium 2 with rigidity μ_2). If $m = \mu_1/\mu_2$, the two particular cases of special interest are for $m = 0$ and $m \rightarrow \infty$. In the case of $m = 0$, we have a tensile dislocation in an elastic half-space with free boundary, as discussed by Singh and Singh (2000). On the other hand, when $m \rightarrow \infty$, we have the case of tensile dislocation in an elastic half-space with a rigid boundary, as considered in the present study. This implies that our model consists of a tensile dislocation in an elastic half-space in contact with a rigid half-space. This model is useful when the medium on the other side of the material discontinuity is very hard. High-rigidity layers are generally present at depths below a volcanic edifice, covered by much softer volcanic-sedimentary layers composed of a mixture of ash, mud and lava (Bonafede and Revalta, 1999).

The aim of the present paper is to study the two-dimensional deformation of a uniform half-space with rigid boundary caused by a long tensile fault of finite width. Beginning with the closed-form expression for the Airy stress function for an arbitrary line source in a uniform half-space given by Rani et al. (1991) and following Singh and Singh (2000), we obtain Airy stress function for a long tensile fault of arbitrary dip and finite width and the expressions for the stresses at any point of the half-space with rigid boundary caused by a long vertical tensile fault. Analytic integration over the width of the fault yields the desired Airy stress function, and the expressions for the stresses at any point of the half-space follow immediately.

THEORY

Let the Cartesian coordinates be denoted by (x_1, x_2, x_3) , with the x_3 -axis oriented vertically downward. We consider a two-dimensional approximation, in which the displacement components u_1 , u_2 and u_3 are independent of x_1 such that $\partial/\partial x_1 \equiv 0$. Under this assumption, the plane-strain problem ($u_1 = 0$) can be solved in terms of the Airy stress function U such that

$$\tau_{22} = \frac{\partial^2 U}{\partial x_3^2} \quad (1a)$$

$$\tau_{33} = \frac{\partial^2 U}{\partial x_2^2} \quad (1b)$$

$$\tau_{23} = -\frac{\partial^2 U}{\partial x_2 \partial x_3} \quad (1c)$$

and

$$\nabla^2 \nabla^2 U = 0 \quad (2)$$

where τ_{22} , τ_{33} and τ_{23} are the components of stress and

$$\nabla^2 \equiv \frac{\partial^2}{\partial x_2^2} + \frac{\partial^2}{\partial x_3^2} \quad (3)$$

As shown by Singh and Garg (1986), the Airy stress function U_0 for a line source parallel to x_1 -axis and passing through the point $(0, 0, h)$ in an infinite medium can be expressed in the form

$$U_0 = \int_0^\infty \left[(L_0 + M_0 k |x_3 - h|) \sin kx_2 + (P_0 + Q_0 k |x_3 - h|) \cos kx_2 \right] k^{-1} e^{-k|x_3 - h|} dk \quad (4)$$

where the source coefficients L_0 , M_0 , P_0 and Q_0 are independent of the variable k . Singh and Garg (1986) and Singh and Rani (1991) have obtained these source coefficients for various seismic sources.

For a line source parallel to the x_1 -axis and acting at the point $(0, 0, h)$ of the half-space $x_3 \geq 0$, a suitable solution of the bi-harmonic equation (i.e., Equation (2)) is of the form

$$U = U_0 + \int_0^\infty [(L + Mkx_3) \sin kx_2 + (P + Qkx_3) \cos kx_2] k^{-1} e^{-kx_3} dk \quad (5)$$

where U_0 is given by Equation (4); and L , M , P and Q are unknowns to be determined from the boundary conditions. We assume that the surface of the half-space $x_3 \geq 0$ is with a rigid boundary. Therefore, the boundary conditions are

$$u_2 = u_3 = 0 \text{ at } x_3 = 0 \quad (6)$$

We have (Sokolnikoff, 1956)

$$2\mu u_2 = -\frac{\partial U}{\partial x_2} + \frac{1}{2\alpha} \int \nabla^2 U dx_2 \quad (7a)$$

and

$$2\mu u_3 = -\frac{\partial U}{\partial x_3} + \frac{1}{2\alpha} \int \nabla^2 U dx_3 \quad (7b)$$

with

$$\alpha = \frac{\lambda + \mu}{\lambda + 2\mu} = \frac{1}{2(1 - \sigma)} \quad (8)$$

Using Equations (5)–(7), we get

$$L = -(L_0 + M_0 kh) e^{-kh} \quad (9a)$$

$$M = -M_0 e^{-kh} \quad (9b)$$

$$P = -(P_0 + Q_0 kh) e^{-kh} \quad (9c)$$

and

$$Q = -Q_0 e^{-kh} \quad (9d)$$

On putting the values of L , M , P and Q from Equations (9a)–(9d) in Equation (5) and integrating, the Airy stress function at any point of the half-space is obtained as

$$U = L_0 \left[\tan^{-1} \frac{x_2}{|x_3 - h|} - \tan^{-1} \frac{x_2}{(x_3 + h)} \right] + M_0 \left[\frac{x_2 |x_3 - h|}{R^2} - \frac{x_2 (x_3 + h)}{S^2} \right] + P_0 \log \left(\frac{S}{R} \right) + Q_0 \left[\frac{|x_3 - h|^2}{R^2} - \frac{(x_3 + h)^2}{S^2} \right] \quad (10)$$

where

$$R^2 = x_2^2 + (x_3 - h)^2 \quad (11a)$$

$$S^2 = x_2^2 + (x_3 + h)^2, \quad x_3 \neq h \quad (11b)$$

Following Singh and Singh (2000), the Airy stress function due to a tensile dislocation on an inclined plane can be expressed in the form,

$$U = U_{\text{VTF}} \sin^2 \delta - U_{\text{VDS}} \sin 2\delta + U_{\text{HTF}} \cos^2 \delta \quad (12)$$

where δ is the dip angle of fault. Further, with ds as the width of the line fault,

$$U_{\text{VTF}} = bdsU_{22} \quad (13)$$

is the Airy stress function for a vertical tensile fault (i.e., $\delta = 90^\circ$) with dislocation in the x_2 -direction,

$$U_{\text{VDS}} = bdsU_{23} \quad (14)$$

is the Airy stress function for a vertical dip-slip fault,

$$U_{\text{HTF}} = bdsU_{33} \quad (15)$$

is the Airy stress function for a horizontal tensile fault (i.e., $\delta = 0^\circ$) with dislocation in the x_3 -direction, and

$$U_{ij} = U_{ji} = \lambda \delta_{ij} \frac{\partial U_k}{\partial y_k} + \mu \left(\frac{\partial U_j}{\partial y_i} + \frac{\partial U_i}{\partial y_j} \right) \quad (16)$$

where U_i denotes the Airy stress function at an arbitrary point $P(x_2, x_3)$ for a unit concentrated force acting at the point $Q(y_2, y_3)$ in the x_i -direction.

On using the values of the source coefficients L_0 , M_0 , P_0 and Q_0 given in Appendix, Equations (10) and (12) yield the Airy stress function due to a long tensile fault of arbitrary dip δ as

$$U = \frac{\mu bds}{2\pi(1-\sigma)} \left[\log \left(\frac{S}{R} \right) + \cos 2\delta \left\{ \frac{(x_3 - h)^2}{R^2} - \frac{(x_3 + h)^2}{S^2} \right\} - \sin 2\delta \left\{ \frac{x_2(x_3 - h)}{R^2} + \frac{x_2(x_3 + h)}{S^2} \right\} \right] \quad (17)$$

where σ denotes Poisson's ratio and μ denotes rigidity. This equation gives the Airy stress function for a line tensile dislocation located at the point $(0, h)$. However, if the line source is located at an arbitrary point (y_2, y_3) , x_2 and h in Equation (17) should be replaced by $(x_2 - y_2)$ and y_3 , respectively. We thus obtain

$$U = \frac{\mu bds}{2\pi(1-\sigma)} \left[\log \left(\frac{S}{R} \right) + \cos 2\delta \left\{ \frac{(x_3 - y_3)^2}{R^2} - \frac{(x_3 + y_3)^2}{S^2} \right\} - \sin 2\delta \left\{ \frac{(x_2 - y_2)(x_3 - y_3)}{R^2} + \frac{(x_2 - y_2)(x_3 + y_3)}{S^2} \right\} \right] \quad (18)$$

with

$$R^2 = (x_2 - y_2)^2 + (x_3 - y_3)^2 \quad (19a)$$

and

$$S^2 = (x_2 - y_2)^2 + (x_3 + y_3)^2 \quad (19b)$$

From Figure 1, we put $y_2 = s \cos \delta$ and $y_3 = s \sin \delta$ into Equation (18) and integrate over s between the limits (s_1, s_2) . We thus obtain the following expression for the Airy stress function for a long tensile fault of finite width $L = s_2 - s_1$:

$$U = (x_2 \sin \delta - x_3 \cos \delta) \tan^{-1} \left[\frac{s - (x_2 \cos \delta + x_3 \sin \delta)}{(x_2 \sin \delta - x_3 \cos \delta)} \right] - (x_2 \sin \delta + x_3 \cos \delta) \tan^{-1} \left[\frac{s - (x_2 \cos \delta - x_3 \sin \delta)}{(x_2 \sin \delta + x_3 \cos \delta)} \right] \Bigg|_{s_1}^{s_2} \quad (20)$$

where

$$f(s) \Big|_{s_1}^{s_2} = f(s_2) - f(s_1) \quad (21)$$

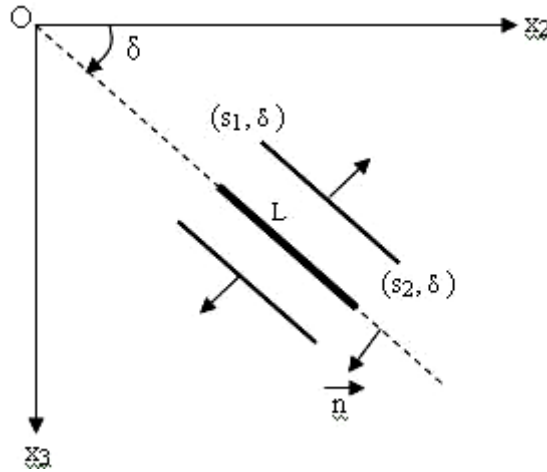


Fig. 1 Geometry of a long tensile fault of width $L = s_2 - s_1$ (the Cartesian coordinates of a point on the fault are (y_2, y_3) and its polar coordinates (s, δ) , where δ is the dip angle and $s_1 \leq s \leq s_2$)

From Equations (1) and (21), the following expressions for stress components due to a vertical tensile fault (i.e., $\delta = 90^\circ$) are obtained

$$\tau_{22} = \frac{\mu b}{2\pi(1-\sigma)} \left[\frac{4x_2^6 x_3 + 4x_2^4 x_3 (2x_3^2 - s^2) + 4x_2^2 x_3 (x_3^4 + 2x_3^2 s^2 - 3s^4)}{\left[(x_2^2 + (s^2 - x_3^2))^2 + 4x_2^2 x_3^2 \right]^2} \right]_{s_1}^{s_2} \quad (22)$$

$$\tau_{23} = \frac{\mu b}{2\pi(1-\sigma)} \left[\frac{x_2^5 (20x_3^2 - 4s^2) + x_2^3 (8x_3^2 s^2 - 8s^4 - 16x_3^4) + x_2 (4x_2^2 s^4 + 4x_3^4 s^2 - 4s^6 - 4x_3^6)}{\left[(x_2^2 + (s^2 - x_3^2))^2 + 4x_2^2 x_3^2 \right]^2} \right]_{s_1}^{s_2} \quad (23)$$

$$\tau_{33} = \frac{\mu b}{2\pi(1-\sigma)} \left[\frac{4x_2^4 x_3 (3s^2 + x_3^2) + 8x_2^2 x_3 (s^4 - 2x_3^2 s^2 + x_3^4) + 4x_3 (3x_3^2 s^4 - 3x_3^4 s^2 + x_3^6 - s^6)}{\left[(x_2^2 + (s^2 - x_3^2))^2 + 4x_2^2 x_3^2 \right]^2} \right]_{s_1}^{s_2} \quad (24)$$

NUMERICAL RESULTS

To study the two-dimensional stress fields around a long vertical tensile fault of finite width L in a uniform half-space with rigid boundary, we put $s_1 = 0$ and $s_2 = L$, and assume $\sigma = 0.25$. For numerical calculations, we define the following dimensionless quantities:

$$Y = \frac{x_2}{L} \quad (25a)$$

$$Z = \frac{x_3}{L} \quad (25b)$$

$$P_{ij} = \frac{\pi L}{\mu b} \tau_{ij} \quad (25c)$$

Thus, Y is the dimensionless distance from the fault trace, Z is the dimensionless depth, and P_{22} , P_{23} and P_{33} are the dimensionless stresses.

From Equations (22)–(25c), we obtain

$$P_{22} = \frac{8Y^2Z[Y^4 + Z^4 + 2Z^2 + 2Y^2Z^2 - 2Y^2 - 3]}{3\left[\left\{Y^2 + (1 - Z^2)\right\}^2 + 4Y^2Z^2\right]^2} \quad (26)$$

$$P_{23} = \frac{8Y[5Y^4Z^2 - Y^4 + 2Y^2Z^2 - Y^2 - 4Y^2Z^4 + Z^4 - Z^6 - 1]}{3\left[\left\{Y^2 + (1 - Z^2)\right\}^2 + 4Y^2Z^2\right]^2} \quad (27)$$

$$P_{33} = \frac{8Z[3Y^4 + Y^4Z^2 + 2Y^2 - 4Y^2Z^2 + 2Y^2Z^4 + Z^6 - 3Z^4 + 3Z^2 - 1]}{3\left[\left\{Y^2 + (1 - Z^2)\right\}^2 + 4Y^2Z^2\right]^2} \quad (28)$$

DISCUSSION

Figures 2(a)–2(c) show the variations of the dimensionless stresses P_{22} , P_{23} and P_{33} , respectively, with dimensionless distance from the fault in the cases of $x_3 = 0.1L$, $0.3L$ and $0.5L$. The patterns of P_{22} and P_{23} are similar with the only difference that P_{22} changes its sign from negative (i.e., compressive stress) to positive (i.e., tensile stress) for some values of x_2 lying between L and $2L$. Both are zero at $x_2 = 0$. P_{33} has non-zero values at $x_2 = 0$ and it also changes its sign for some values of x_2 lying between 0 and L . All the three stresses tend to zero for the large values of x_2 . The variation of stress P_{22} with distance from the fault (see Figure 2(a)) for $x_3 = 0.1L$ is similar to that for P_{22} at $x_3 = 0$, as in Singh and Singh (2000), but for large values of depth, the pattern near the origin is significantly different due to the rigid boundaries.

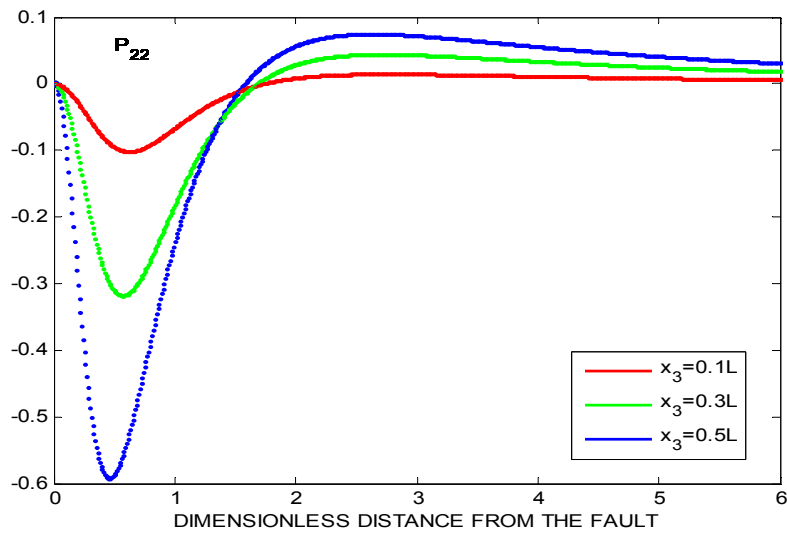
Figures 3(a)–3(c) show the variations of the dimensionless stresses P_{22} , P_{23} and P_{33} , respectively, with depth at $x_2 = 0.3L$, $0.8L$ and $1.3L$. The variations of the normal and shear stresses are smooth for the large values of x_3 . These variations are noteworthy near the fault, particularly at $x_3 = L$. The patterns of the stresses P_{22} and P_{23} in Figures 3(a) and 3(b) respectively are similar to those obtained by Singh and Singh (2000), except for the behaviour of stress components very near the origin.

ACKNOWLEDGEMENTS

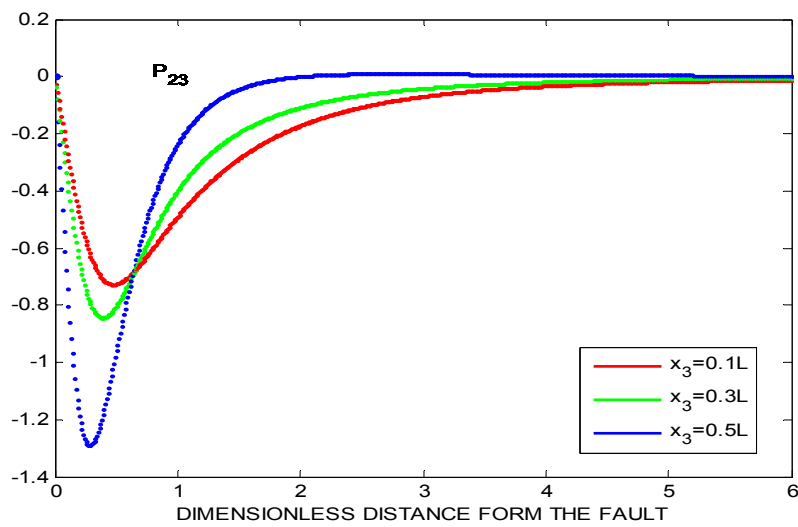
The authors are grateful to Professor Sarva Jit Singh for his valuable suggestions. The authors are thankful to the referees for their comments, which led to an improvement in the presentation of the paper.

APPENDIX: VALUES OF SOURCE COEFFICIENTS

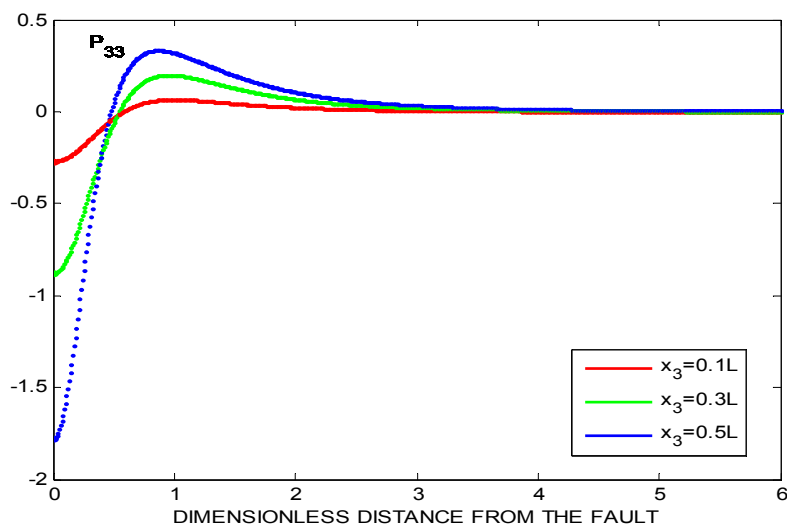
The values of source coefficients L_0 , M_0 , P_0 and Q_0 in three different cases are given below, where the upper sign is for $x_3 > h$, the lower sign is for $x_3 < h$, b is the magnitude of the displacement dislocation, and ds is the width of the line fault.



(a)

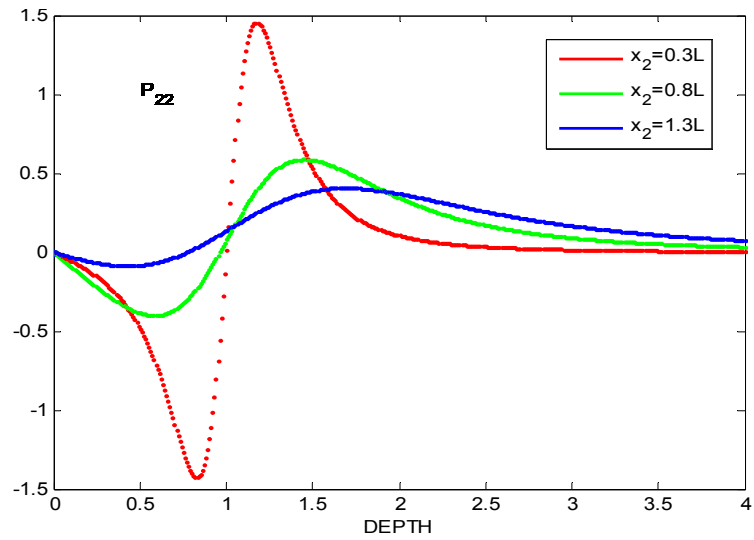


(b)

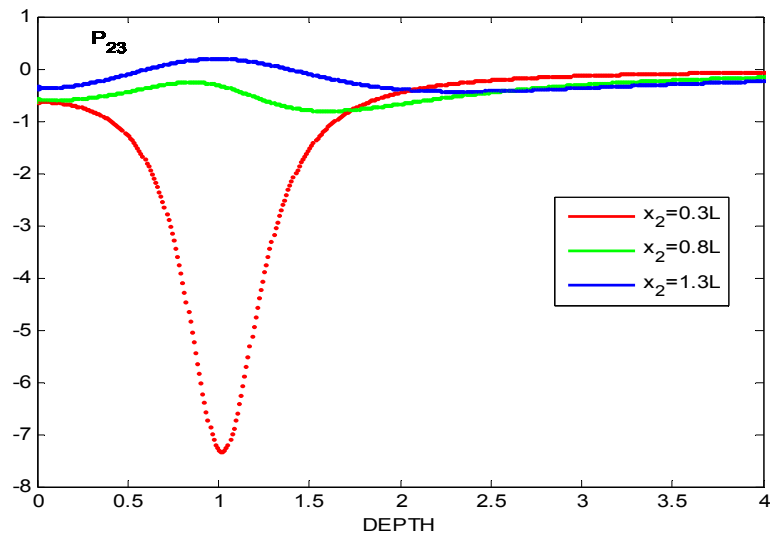


(c)

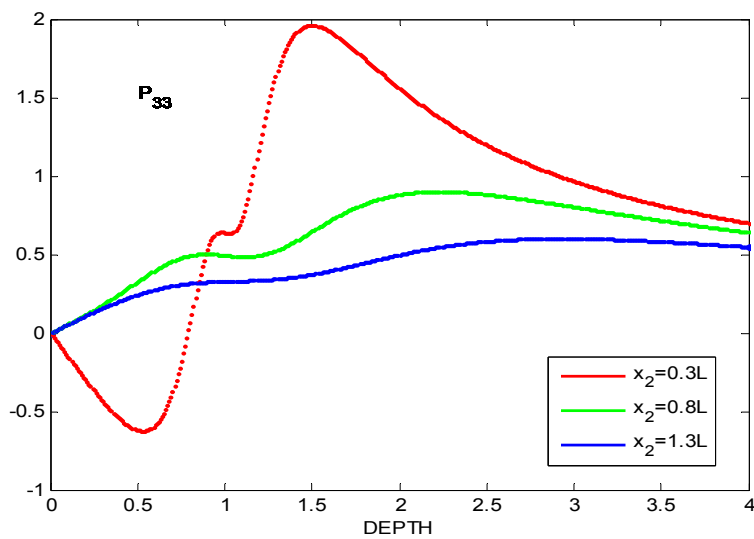
Fig. 2 Variations of the dimensionless (a) normal stress P_{22} , (b) shear stress P_{23} , (c) normal stress P_{33} , with distance from the fault for $x_3 = 0.1L, 0.3L$ and $0.5L$



(a)



(b)



(c)

Fig. 3 Variations of the dimensionless (a) normal stress P_{22} , (b) shear stress P_{23} , (c) normal stress P_{33} , with depth for $x_2 = 0.3L, 0.8L$ and $1.3L$

1. Vertical Dip-Slip Fault

$$L_0 = P_0 = Q_0 = 0 \quad (\text{A.1})$$

$$M_0 = \pm \frac{\mu b d s}{2\pi(1-\sigma)} \quad (\text{A.2})$$

2. Vertical Tensile Fault

$$L_0 = M_0 = 0 \quad (\text{A.3})$$

$$P_0 = -Q_0 = \frac{\mu b d s}{2\pi(1-\sigma)} \quad (\text{A.4})$$

3. Horizontal Tensile Fault

$$L_0 = M_0 = 0 \quad (\text{A.5})$$

$$P_0 = Q_0 = \frac{\mu b d s}{2\pi(1-\sigma)} \quad (\text{A.6})$$

REFERENCES

1. Barker, J.S. and Langston, C.A. (1983). "A Teleseismic Body-Wave Analysis of the May 1980 Mammoth Lakes, California, Earthquakes", *Bulletin of the Seismological Society of America*, Vol. 73, No. 2, pp. 419-434.
2. Bonafede, M. and Rivalta, E. (1999). "The Tensile Dislocation Problem in a Layered Elastic Medium", *Geophysical Journal International*, Vol. 136, No. 2, pp. 341-356.
3. Davis, P.M. (1983). "Surface Deformation Associated with a Dipping Hydrofracture", *Journal of Geophysical Research*, Vol. 88, No. B7, pp. 5826-5834.
4. Dziewonski, A.M. and Woodhouse, J.H. (1983). "An Experiment in Systematic Study of Global Seismicity: Centroid-Moment Tensor Solutions for 201 Moderate and Large Earthquakes of 1981", *Journal of Geophysical Research*, Vol. 88, No. B4, pp. 3247-3271.
5. Julian, B.R. (1983). "Evidence for Dyke Intrusion Earthquake Mechanisms near Long Valley Caldera, California", *Nature*, Vol. 303, No. 5915, pp. 323-325.
6. Maruyama, T. (1964). "Static Elastic Dislocation in an Infinite and Semi-Infinite Medium", *Bulletin of the Earthquake Research Institute, University of Tokyo*, Vol. 42, No. 2, pp. 289-368.
7. Okada, Y. (1985). "Surface Deformation due to Shear and Tensile Faults in a Half-Space", *Bulletin of the Seismological Society of America*, Vol. 75, No. 4, pp. 1135-1154.
8. Okada, Y. (1992). "Internal Deformation due to Shear and Tensile Faults in a Half-Space", *Bulletin of the Seismological Society of America*, Vol. 82, No. 2, pp. 1018-1040.
9. Piombo, A., Tallarico, A. and Dragoni, M. (2007). "Displacement, Strain and Stress Fields due to Shear and Tensile Dislocations in a Viscoelastic Half-Space", *Geophysical Journal International*, Vol. 170, No. 3, pp. 1399-1417.
10. Rani, S. and Singh, S.J. (1992). "Static Deformation of a Uniform Half-Space due to a Long Dip-Slip Fault", *Geophysical Journal International*, Vol. 109, No. 2, pp. 469-476.
11. Rani, S., Singh, S.J. and Garg, N.R. (1991). "Displacements and Stresses at any Point of a Uniform Half-Space due to Two Dimensional Buried Sources", *Physics of the Earth and Planetary Interiors*, Vol. 65, No. 3-5, pp. 276-282.
12. Singh, M. and Singh, S.J. (2000). "Static Deformation of a Uniform Half-Space due to a Very Long Tensile Fault", *ISSET Journal of Earthquake Technology*, Vol. 37, No. 1-3, pp. 27-38.
13. Singh, S.J. and Garg, N.R. (1986). "On the Representation of Two-Dimensional Seismic Sources", *Acta Geophysica Polonica*, Vol. 34, No. 1, pp. 1-12.

14. Singh, S.J. and Rani, S. (1991). "Static Deformation due to Two-Dimensional Seismic Sources Embedded in an Isotropic Half-Space in Welded Contact with an Orthotropic Half-Space", *Journal of Physics of the Earth*, Vol. 39, No. 5, pp. 599-618.
15. Sipkin, S.A. (1986). "Interpretation of Non-Double-Couple Earthquake Mechanisms Derived from Moment Tensor Inversion", *Journal of Geophysical Research*, Vol. 91, No. B1, pp. 531-547.
16. Sokolnikoff, I.S. (1956). "Mathematical Theory of Elasticity", McGraw-Hill Book Company, New York, U.S.A.
17. Steketee, J.A. (1958). "On Volterra's Dislocations in a Semi-Infinite Elastic Medium", *Canadian Journal of Physics*, Vol. 36, No. 2, pp. 192-205.
18. Yang, M. and Davis, P.M. (1986). "Deformation due to a Rectangular Tension Crack in an Elastic Half-Space", *Bulletin of the Seismological Society of America*, Vol. 76, No. 3, pp. 865-881.

HEALTH ASSESSMENT OF STRUCTURES EXPOSED TO SEISMIC EXCITATIONS

Ajoy Kumar Das and Achintya Haldar

Department of Civil Engineering & Engineering Mechanics
University of Arizona
Tucson, AZ 85721, U.S.A.

ABSTRACT

The health assessment of existing infrastructure just after an earthquake is a very important but challenging task. Even engineered structures can suffer significant damage(s) due to seismic excitations. To ensure public safety and to maintain the economic activities of the surrounding communities, structural health needs to be assessed promptly following an earthquake. Two novel structural health assessment procedures are under development at the University of Arizona. They are known as the modified iterative least-squares with unknown input (MILS-UI) and generalized iterative least-squares extended Kalman filter with unknown input (GILS-EKF-UI) techniques. These procedures are finite-element based time domain system identification (SI) techniques, which are capable of identifying structures at the element level by using only the dynamic response information. These procedures have been extensively verified by using the numerically simulated and laboratory measured response information, as obtained for the defect-free and defective frames under sinusoidal and impulsive excitations. The health assessment of the same defect-free and defective frames by using the numerically simulated response information under seismic excitations is presented here.

KEYWORDS: Earthquake Ground Motion, Finite Element, System Identification, Structural Health Assessment

INTRODUCTION

The health assessment of an engineered civil infrastructure just after strong earthquakes is very important for quickly developing post-disaster mitigation plans in the most economical way, without exposing the public to excessive risk. The mitigation plans may include opening them to public with or without some restrictions of their uses, inspecting them more frequently, repairing the identified defective members, or of replacing the whole structure. As recommended in many standards and practiced widely, visual inspections are primarily used to assess structural health and to develop the remedial actions as necessary. However, a visual inspection does not consider structural performance at the current deteriorated state. Thus, it cannot provide a quantitative assessment of the structural health. This deficiency reduces its effectiveness to assess structural health in many different ways, including the importance of a member in the overall structural integrity, redundancy in the load transfer path, load carrying capacity of the member during the ground excitations, lack of accessibility to inspect the member or the defects that may be hidden behind the obstructions, and the prior history of damage that might have been caused during the installation and/or due to the accidental loads. Also, visual inspections may require an excessive amount of resources in some cases, for example, in inspecting a bridge over a river.

Damages that change structural behaviour may not always be visible with the naked eye. During the 1994 Northridge earthquake, welds got fractured in the moment-resisting steel frames. Similarly, welds got fractured during the 1989 Loma Prieta earthquake, but those remained undetected for a long period, thus exposing the users of these buildings to an additional risk. If the locations of defective spots are known, we have technological sophistication to inspect them, when we use localized experimental techniques, such as acoustic, ultrasonic, magnetic-field, radio-graphs, eddy-current, thermal-field methods. These techniques can also be used to inspect different types of structures, including the marine offshore structures, aerospace structures, etc. However, they may not be appropriate to inspect a complex civil infrastructure consisting of high-rise buildings, long-span bridges with complex arrangements, industrial structures, etc., since the locations of defects are unknown in such cases. An objective nondestructive procedure is therefore urgently needed for the rapid assessment of structural health.

Numerous damage detection philosophies have been developed during the last three decades. They are effectively summarized in several state-of-the-art papers (Lew et al., 1991; Ghanem and Shinozuka, 1995; Shinozuka and Ghanem, 1995; Doebling et al., 1996; Housner et al., 1997; Humar et al., 2006; Kerschen et al., 2006; Worden et al., 2007; Worden et al., 2008; Ahmed, 2009). Due to its many advantages, structural health assessment (SHA) using dynamic response information has recently become very popular in the research community. Its basic philosophy is based on the concept that the damage(s) that cause changes in the structural dynamical behaviour or responses can be characterized by using an inverse identification procedure, known as the system identification (SI) technique. There are three basic components in a vibration-based SI technique, namely, (i) input time-varying loading or excitation, (ii) the system that needs to be identified, assuming that it can be represented by a series of equations in terms of its parameters, such as mass, stiffness and damping properties, and (iii) the output structural dynamic responses measured by the sensors. The main objective here is to obtain information on the system parameters by using only the output dynamic responses. The information on the input excitation may or may not be necessary. Many vibration-based SI procedures have already been developed; their relative merits and demerits are available in the literature (Wang and Haldar, 1994).

When the dynamic responses of a system are employed for parameter identification, the response information can be processed either in the frequency domain or in the time domain. In general, the frequency-domain procedures are relatively simpler and have, therefore, been widely used in the past. They can assess structural health in the global sense, i.e., they can answer whether the structure is defective or not, but they cannot identify the location or the severity of defects. This prompted the researchers, including the authors and their research team, to detect defects at the local element level by using different time-domain numerical procedures, including the recursive techniques, maximum likelihood techniques, etc. In any case, SHA can be broadly conducted at four different Levels (Rytter, 1993), namely, Level 1 consisting of the determination of the presence of damage in a structure, Level 2 consisting of the determination of geometric location of the damage, Level 3 consisting of the quantification of the severity of the damage, and Level 4 consisting of the prediction of the remaining service life of the structure. Levels 1, 2 and 3 are specifically addressed in this paper. In general, the procedure used should be simple, inexpensive, and easy-to-implement for a quick SHA.

Two novel structural health assessment procedures are under active development by a research team at the University of Arizona, which will satisfy the first three levels of SHA. They are finite-element based time-domain SI techniques, which can assess the health of structures at the element level by using only the noise-contaminated dynamic response information and without using any information on the input excitation, thus increasing the implementation potential of these techniques. These procedures are conceptually based on the minimization of errors in the identified parameters. A least-squares based procedure, called as the iterative least-squares with unknown input (ILS-UI) method, was initially developed by Wang and Haldar (1994) for the situation when dynamic response information is available at all the dynamic degrees of freedom (DDOFs). They considered viscous damping in the governing equations of motion and identified damping for all the members in a structure. Since the changes in damping caused by different levels of defects are not known clearly at present, and to improve the efficiency of the algorithm, a Rayleigh-type (i.e., mass- as well as stiffness-proportional) damping instead of viscous damping can be used without compromising the damage detection capability. This is called as the modified iterative least-squares (MILS-UI) method (Ling and Haldar, 2004; Katkhuda et al., 2005). For a structure consisting of m structural elements, the ILS-UI procedure will identify m damping parameters, but these parameters will be only two if the MILS-UI method is used. The MILS-UI method significantly improves the efficiency of the algorithm, particularly for the large structural systems. Since the response information may not be available at all the DDOFs, particularly for the large real structures, later Wang and Haldar (1997) successfully exploited the ability of the extended Kalman filter (EKF) technique to identify a structure by using the minimum response information, developed a new technique by combining EKF with the ILS-UI method, and called it as the ILS-EKF-UI method. Several improvements were incorporated later into this method to increase its computational efficiency and to make it applicable for the health assessment of real structures. This is now known as the generalized iterative least-squares extended Kalman filter with unknown input (GILS-EKF-UI) method (Katkhuda and Haldar, 2008; Haldar, 2009). It is necessary to emphasize that the EKF-based procedures have been used over the years for structural identification by using their standard form (Hoshiya and Saito, 1984; Koh et al., 1991; Hoshiya and Sutoh, 1993; Oreta and Tanabe, 1993, 1994; Maruyama and Hoshiya, 2001; Corigliano and Mariani, 2004; Ghanem and Ferro, 2006; Wu and Smyth, 2007). Recently, a few

slightly varied forms of the EKF method (Yang et al., 2006, 2007; Ghosh et al., 2007; Zhou et al., 2008; Saha and Roy, 2009) have also been used for SHA. The proposed GILS-EKF-UI procedure uses the standard EKF form for SHA by using the minimum response information.

The ILS-UI and MILS-UI procedures were extensively verified by using the numerically simulated response information for the fixed-ended and simply-supported one-dimensional beams (Vo and Haldar, 2004). In this approach, the computer-generated response information was used to identify the defect-free and defective beams excited by the sinusoidal loading. After the completion of this phase, the health of the beams was successfully assessed by using the experimental responses obtained in a laboratory (Vo and Haldar, 2008a, 2008b). After the verification of the ILS-UI and MILS-UI methods for one-dimensional beams, this study was extended to identify the health of a two-dimensional frame. As will be discussed in more detail later, the responses of steel frame to sinusoidal and impulsive loadings were numerically simulated by using a commercially available computer program. Defects of several types were then introduced in the frame. The MILS-UI and GILS-EKF-UI methods were verified by using the analytical response information (Katkhuda, 2004; Katkhuda et al., 2005; Katkhuda and Haldar, 2006; Haldar and Das, 2010), as obtained for the health assessment of the undamaged and damaged configurations. A one-third scale model of the frame was then built and the health assessment capabilities of the two methods were studied by conducting extensive laboratory investigations for the sinusoidal and impulsive loadings applied at the super-structure. By using the so-obtained experimental response information, the health of the frame was assessed for its undamaged and damaged configurations (Martinez-Flores, 2005; Martinez-Flores and Haldar, 2007; Martinez-Flores et al., 2008; Haldar et al., 2008). Since it was not possible in our laboratory to excite the frame by a seismic loading applied at its base, this paper mainly focuses on the theoretical verification of both methods by using the numerically simulated responses of the frame under a seismic excitation and on the confirmation of the observations already made during the laboratory investigations with other types of loadings. The responses are numerically simulated by using the commercially available ANSYS software. For the ease of presentation, the theoretical concepts behind the MILS-UI and GILS-EKF-UI methods are briefly discussed below.

MATHEMATICAL CONCEPT OF MILS-UI PROCEDURE

The governing differential equations of motion of a linear multi-degree-of-freedom system under an earthquake excitation can be written in matrix notation as

$$[M]\{\ddot{x}(t)\} + [C]\{\dot{x}(t)\} + [K]\{x(t)\} = -[M]\{I\}\{\ddot{u}_g(t)\} \quad (1)$$

where $[M]$ is the global mass matrix, $[C]$ is the viscous damping matrix, $[K]$ is the global stiffness matrix, $\{I\}$ is the unit vector, and $\{\ddot{u}_g(t)\}$ is the ground-acceleration time-history vector. As discussed earlier, in the MILS-UI method, the damping is considered to be (mass- and stiffness-proportional) Rayleigh damping and therefore it can be represented as $(\alpha[M] + \beta[K])$, where α and β are the Rayleigh damping coefficients, and $\{\ddot{x}(t)\}$, $\{\dot{x}(t)\}$ and $\{x(t)\}$ are the vectors containing the dynamic responses in terms of acceleration, velocity and displacement, respectively, relative to the base at the time t . The global mass and stiffness matrices can be formed by using the standard finite element procedure. As in the other SI methods, the mass matrix $[M]$ is assumed to be known. Since it is impractical to know the exact time history of the earthquake ground acceleration soon after the excitation, it is considered to be unknown. The parameters to be identified are the stiffness parameters in $[K]$ and the damping coefficients, α and β . To this end, Equation (1) can be reorganized as

$$[A(t)]_{nm \times h} \{D\}_{h \times 1} = \{F(t)\}_{nm \times 1} \quad (2)$$

For the over-determined system represented by Equation (2), $[A(t)]$ is a rectangular matrix with the number of rows, nm , greater than the number of columns, h , and is populated with the responses at all the DDOFs in terms of displacement vector $\{x(t)\}$ and velocity vector $\{\dot{x}(t)\}$ at the time t ; $\{D\}$ is a

vector composed of the unknown system parameters (i.e., the stiffness and damping coefficients) to be identified; $\{F(t)\}$ is a vector composed of the unknown input ground excitation and the inertia forces at the time t ; h is the total number of unknown parameters to be identified; nm is equal to $n \times m$; n is the total number of DDOFs; and m is the total number of the time points of the response measurements.

The system parameter vector $\{D\}$ in Equation (2) can be defined as

$$\{D\}_{h \times 1} = [k_1, k_2, \dots, k_{ne}, \beta k_1, \beta k_2, \dots, \beta k_{ne}, \alpha]^T \quad (3)$$

where h is equal to $2ne + 1$; ne is the total number of finite elements; k_i is the stiffness parameter of the i th element and is defined as $E_i I_i / L_i$, where L_i and I_i are respectively the length and the second moment of inertia of the cross-section of the member, and E_i is the Young's modulus of elasticity of the material. To solve for $\{D\}$, the least-square technique is used to minimize the total error Er in the identification of the structure, i.e.,

$$Er = \sum_{r=1}^{n \times m} \left(F_r - \sum_{s=1}^h A_{rs}(t) D_s \right)^2; \quad r = 1, 2, \dots, n \times m \quad (4)$$

To minimize the total error, Equation (4) is differentiated with respect to each one of the D_i parameters as

$$\frac{\partial Er}{\partial D_i} = \sum_{r=1}^{n \times m} \left(F_r - \sum_{s=1}^h A_{rs} D_s \right) A_{ri} = 0; \quad i = 1, 2, \dots, h \quad (5)$$

Equation (5) gives h simultaneous equations, the solution of which will give the estimation of all the h unknown parameters. The unknown parameters can be evaluated as

$$\{D\}_{h \times 1} = \left([A]_{h \times nm}^T [A]_{nm \times h} \right)^{-1} [A]_{h \times nm}^T \{F\}_{nm \times 1} \quad (6)$$

The system parameter vector $\{D\}$ can be solved, provided the force vector $\{F(t)\}$ and matrix $[A(t)]$ are known. However, since the input ground excitation is not known, the force vector $\{F(t)\}$ in Equation (2) becomes an unknown. The MILS-UI method solves for the vector $\{D\}$ by starting an iterative process, where the unknown input seismic excitation is assumed to be zero at all time points (Katkuda et al., 2005). This assumption guarantees a non-singular solution of Equation (2), without compromising the convergence or the accuracy of the method. It is observed that the method is not sensitive to this initial assumption. It may be emphasized that the fully populated square matrix $[A]^T [A]$ has full rank and does have an inverse. In Equation (6), $\left([A]^T [A] \right)^{-1} [A]^T$ is called as the pseudo inverse of matrix $[A]$.

The major drawback of the MILS-UI procedure is that it requires responses to be observed at all DDOFs. This may not be possible for large structures with numerous DDOFs. Also, the presence of noise in the measured responses is not explicitly addressed by the MILS-UI method. To increase the implementation potential of this method, so that it is able to identify large complicated structural systems, the GILS-EKF-UI method is proposed below.

MATHEMATICAL CONCEPT OF GILS-EKF-UI PROCEDURE

The basic objective of the GILS-EKF-UI method is to identify large structural systems by using only the noise-contaminated response measured at a small part of the structure. This will be discussed in more detail in the section on verification, for the situation when the health of a two-dimensional frame shown in Figure 1 needs to be assessed. The finite-element representation of the frame is shown in Figure 2(a). Responses are measured only at a small part of the frame, denoted hereafter as the substructure and shown

in Figure 2(b). The substructure consists of three nodes, i.e., Nodes 1, 2, and 3, and two elements, i.e., Beam 1 and Column 4. Our task is to identify the whole frame by using the responses measured at the three nodes. It will be shown that the GILS-EKF-UI method can be used for this purpose. It may be pointed out that in a real inspection accelerometers are used to measure the responses. The required information on velocity and displacement time histories is then obtained by successively integrating the measured acceleration time histories (Vo and Haldar, 2003). The issues related to noise-contaminated acceleration time histories have been discussed by Vo and Haldar (2003).



Fig. 1 Three-story experimental frame

The Kalman filter (KF)-based methodologies (Jazwinski, 1970; Maybeck, 1979; Welch and Bishop, 1995) can be used if response information is not available at all the DDOFs; however, in order to implement these methodologies, the information on input excitation and the initial state vector must be available. The extended Kalman filter method with weighted global iteration (EKF-WGI) proposed by Hoshiya and Saito (1984) also requires similar information; however, it can only identify mildly nonlinear systems. In any case, with the requirements of additional information, the basic KF-based formulation will not satisfy the main objective of this study. To circumvent this situation, the desirable features of the MILS-UI and EKF methods are integrated and a two-stage approach is proposed, leading to the development of the GILS-EKF-UI method. In Stage 1, based on the available response information, a substructure is considered that will satisfy all the requirements of the MILS-UI method. At the completion of Stage 1, the time history of the unknown excitation force, the Rayleigh-damping coefficients, and the stiffness parameters of all the elements in the substructure will be available. The information obtained on damping will be applicable to the whole structure. Further, the stiffness parameters identified for the substructure can be judiciously used to develop the initial state vector of the stiffness parameters for the whole structure. The generated information will thus satisfy all the requirements to implement the EKF-based concept, and therefore in Stage 2, the whole structure can be identified by using only a limited noise-contaminated response information.

The location and size of substructure are to be selected based on the available measured responses. For economic reasons, the size of substructure should be kept to a minimum. The past maintenance history of the structure being inspected or the experience of inspectors in dealing with a particular type of structure may also help in selecting the location of the substructure appropriately. However, the defect predictability of the method improves significantly, if the substructure is located close to the defect. Multiple substructures at different locations are expected to work better, since at least one of them is likely to be close to the location of defect. As in all engineering problems, engineering judgment is expected to improve the damage predictability of the method. Although for a class of problems, substructuring can be automated, but this option is not considered while developing a general-purpose procedure.

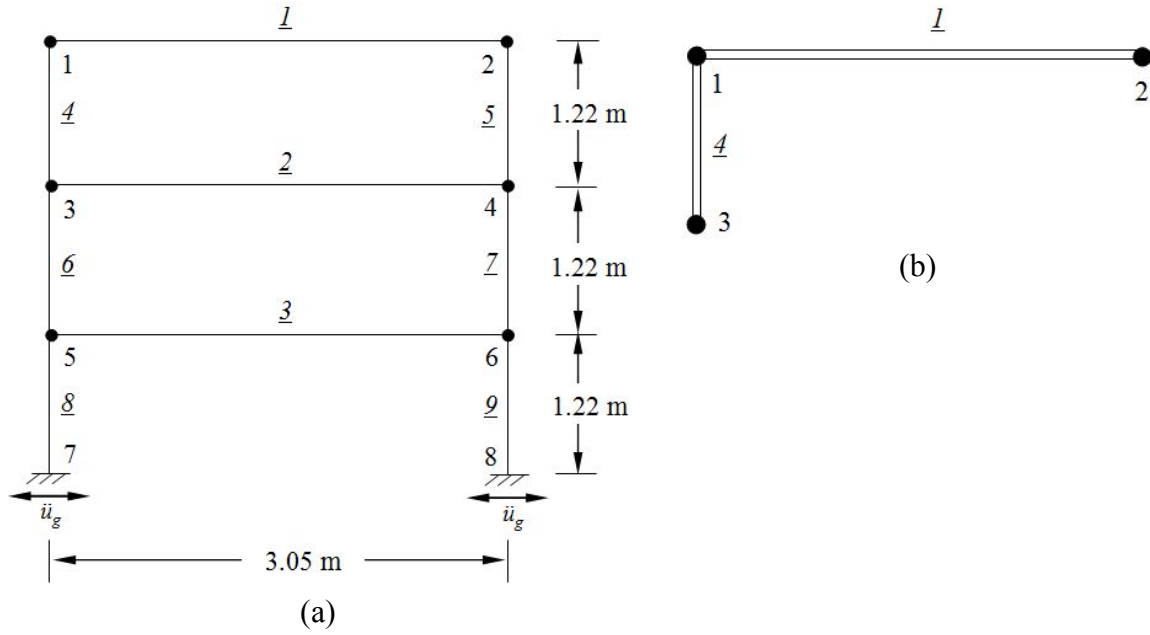


Fig. 2 (a) Finite-element representation of the experimental frame; (b) Substructure for the GILS-EKF-UI method

In order to apply the GILS-EKF-UI method, the state vector can be defined as

$$\{Z(t)\} = \begin{Bmatrix} \{Z_1(t)\} \\ \{Z_2(t)\} \\ \{Z_3(t)\} \end{Bmatrix} = \begin{Bmatrix} \{X(t)\} \\ \{\dot{X}(t)\} \\ \{\tilde{K}\} \end{Bmatrix} \quad (7)$$

where $\{Z(t)\}$ is the state vector at the time t , $\{X(t)\}$ and $\{\dot{X}(t)\}$ are the displacement and velocity vectors, respectively, at the time t for the whole structure, and $\{\tilde{K}\}$ is a vector containing the stiffness parameters of the whole structure that needs to be identified. The stiffness parameter for the i th member, defined earlier for the MILS-UI method as $k_i = E_i I_i / L_i$, will remain the same. The structural system is considered to be time invariant during the identification process; hence, the stiffness parameters k_1, k_2, \dots will remain unchanged during this period. During the updating process, the derivatives of the state vector are necessary. For seismic excitation, those can be shown to be

$$\begin{aligned} \{\dot{Z}(t)\} &= \begin{Bmatrix} \{\dot{Z}_1(t)\} \\ \{\dot{Z}_2(t)\} \\ \{\dot{Z}_3(t)\} \end{Bmatrix} = \begin{Bmatrix} \{\dot{X}(t)\} \\ \{\ddot{X}(t)\} \\ \{0\} \end{Bmatrix} \\ &= \begin{bmatrix} \{\dot{X}(t)\} \\ -[M]^{-1} \left([K]\{X(t)\} + (\alpha[M] + \beta[K])\{\dot{X}(t)\} + [M]\{I\}\{\ddot{u}_g\} \right) \\ \{0\} \end{bmatrix} \end{aligned} \quad (8)$$

To consider the error in the initial state vector $\{Z_{t_0}\}$, it is considered to be Gaussian with the mean vector $\{\hat{Z}_{t_0}\}$ and the constant error covariance matrix $[P_{t_0}]$, and denoted as $\{Z_{t_0}\} \sim N(\{\hat{Z}_{t_0}\}, [P_{t_0}])$.

To consider uncertainty in the measured responses, the observational vector $\{Y_{t_k}\}$ at the time t_k can be expressed as

$$\{Y_{t_k}\} = [H]\{Z_{t_k}(t_k)\} + \{V_{t_k}\} \quad (9)$$

where $[H]$ is a matrix containing information on the measured responses and $\{V_{t_k}\}$ is the observational noise vector. The vector $\{V_{t_k}\}$ is generally assumed to be Gaussian white noise with zero vector as the mean vector and $[R_{t_k}]$ as the covariance matrix, and denoted as $\{V_{t_k}\} \sim N(\{0\}, [R_{t_k}])$. All the other parameters are same as defined earlier.

1. Stage 1

The substructure used in this study to identify the whole frame is shown in Figure 2(b). The information on the measured response of the frame will satisfy the minimum requirements for implementing the MILS-UI method. A successful completion of Stage 1 will produce information on the stiffness parameters of the two members, i.e., one beam and one column, the unknown excitation and the two Rayleigh damping coefficients. In order to develop the initial state vector of the whole frame, the initial stiffness parameters of all the beams in the frame will be assumed to have the same value as identified for the beam in the substructure. Similarly, all the columns will be assigned the same stiffness parameter as identified for the column in the substructure. With this, the information necessary to implement Stage 2 will become available.

2. Stage 2

With the initial state vector $\{\hat{Z}_0(t_0/t_0)\}$ having been defined at the completion of Stage 1, Stage 2 is initiated with the following steps.

2.1 Step 1: Define the Initial Covariance Matrix

The initial error covariance matrix $[P(t_0/t_0)]$ contains the information on the errors in the measured responses and in the initial estimate of the stiffness parameters of the elements. This is generally expressed as (Hoshiya and Saito, 1984; Wang and Haldar, 1997)

$$[P(t_0/t_0)] = \begin{bmatrix} [P_x(t_0/t_0)] & [0] \\ [0] & [P_k(t_0/t_0)] \end{bmatrix} \quad (10)$$

where $[P_x(t_0/t_0)]$ is a $2n \times 2n$ matrix, which contains the initial covariance matrices of displacement and velocity and is assumed to have a value of 1.0 in the diagonals, and $[P_k(t_0/t_0)]$ is a $ne \times ne$ diagonal matrix, which contains the initial covariance matrix of $\{\tilde{K}\}$. Here, n and ne are the total number of DDOFs and the total number of elements in the whole structure, respectively. Hoshiya and Saito (1984) pointed out that the diagonals in $[P_k(t_0/t_0)]$ should be large positive numbers to accelerate the convergence and recommended the value of 1000 for this purpose.

2.2 Step 2: Prediction Phase

In the context of EKF, the predicted state $\{\hat{Z}(t_{k+1}/t_k)\}$ and its error covariance $[P(t_{k+1}/t_k)]$ for the next time increment is evaluated as

$$\{\hat{Z}(t_{k+1}/t_k)\} = \{\hat{Z}(t_k/t_k)\} + \int_{t_k}^{t_{k+1}} f[\{\hat{Z}(t/t_k)\}, t] dt \quad (11)$$

and

$$\left[P(t_{k+1}/t_k) \right] = \left[\Phi \left[t_{k+1}, t_k; \left\{ \hat{Z}(t_k/t_k) \right\} \right] \right] \cdot \left[P(t_k/t_k) \right] \cdot \left[\Phi \left[t_{k+1}, t_k; \left\{ \hat{Z}(t_k/t_k) \right\} \right] \right]^T \quad (12)$$

where the integral in Equation (11) contains the first derivative of the state vector; $\left[\Phi \left[t_{k+1}, t_k; \left\{ \hat{Z}(t_k/t_k) \right\} \right] \right]$ is the state transfer matrix from the time t_k to t_{k+1} and can be written in an approximate form as

$$\left[\Phi \left[t_{k+1}, t_k; \left\{ \hat{Z}(t_k/t_k) \right\} \right] \right] = [I] + \Delta t \cdot \left[F \left[t_k; \left\{ \hat{Z}(t_k/t_k) \right\} \right] \right] \quad (13)$$

In this equation, $[I]$ is a unit matrix and

$$\left[F \left[t_k; \left\{ \hat{Z}(t_k/t_k) \right\} \right] \right] = \left[\frac{\partial f \left[\left\{ Z(t_k) \right\}, t_k \right]}{\partial Z_j} \right]_{\left\{ Z(t_k) \right\} = \left\{ \hat{Z}(t_k/t_k) \right\}} \quad (14)$$

where Z_j is the j th component of the vector $\left\{ Z(t_k) \right\}$.

2.3 Step 3: Estimation of Kalman Gain

The Kalman gain matrix is estimated in the following way:

$$\left[K \left[t_{k+1}; \left\{ \hat{Z}(t_{k+1}/t_k) \right\} \right] \right] = \left[P(t_{k+1}/t_k) \right] \cdot \left[M \left[t_{k+1}; \left\{ \hat{Z}(t_{k+1}/t_k) \right\} \right] \right]^T \cdot \left\{ \left[M \left[t_{k+1}; \left\{ \hat{Z}(t_{k+1}/t_k) \right\} \right] \right] \cdot \left[P(t_{k+1}/t_k) \right] \cdot \left[M \left[t_{k+1}; \left\{ \hat{Z}(t_{k+1}/t_k) \right\} \right] \right]^T + \left[R(t_{k+1}) \right] \right\}^{-1} \quad (15)$$

with

$$\left[M \left[t_k; \left\{ \hat{Z}(t_k/t_k) \right\} \right] \right] = \frac{\partial \left[H \left(\left\{ Z(t_k) \right\}, t_k \right) \right]}{\partial Z_j} \quad (16)$$

2.4 Step 4: Updating Phase

Since observations are available at the time t_{k+1} , the updated state $\left\{ \hat{Z}(t_{k+1}/t_{k+1}) \right\}$ is obtained by using the Kalman gain matrix $\left[K \left[t_{k+1}; \left\{ \hat{Z}(t_{k+1}/t_k) \right\} \right] \right]$ and by using the information on the predicted state (via Equation (11)) and the observed state as

$$\left\{ \hat{Z}(t_{k+1}/t_{k+1}) \right\} = \left\{ \hat{Z}(t_{k+1}/t_k) \right\} + \left[K \left[t_{k+1}; \left\{ \hat{Z}(t_{k+1}/t_k) \right\} \right] \right] \cdot \left\{ \left[Y(t_{k+1}) \right] - \left[H \left(\left\{ \hat{Z}(t_{k+1}/t_k) \right\} \right) \right] \right\} \quad (17)$$

The corresponding updated error covariance matrix $\left[P(t_{k+1}/t_{k+1}) \right]$ can be shown to be

$$\begin{aligned} \left[P(t_{k+1}/t_{k+1}) \right] &= \left\{ \left[I \right] - \left[K \left[t_{k+1}; \left\{ \hat{Z}(t_{k+1}/t_k) \right\} \right] \right] \cdot \left[M \left[t_{k+1}; \left\{ \hat{Z}(t_{k+1}/t_k) \right\} \right] \right]^T \right\} \cdot \left[P(t_{k+1}/t_k) \right] \\ &\quad \cdot \left\{ \left[I \right] - \left[K \left[t_{k+1}; \left\{ \hat{Z}(t_{k+1}/t_k) \right\} \right] \right] \cdot \left[M \left[t_{k+1}; \left\{ \hat{Z}(t_{k+1}/t_k) \right\} \right] \right]^T \right\} \\ &\quad + \left[K \left[t_{k+1}; \left\{ \hat{Z}(t_{k+1}/t_k) \right\} \right] \right] \cdot \left[R(t_{k+1}) \right] \cdot \left[K \left[t_{k+1}; \left\{ \hat{Z}(t_{k+1}/t_k) \right\} \right] \right]^T \end{aligned} \quad (18)$$

The prediction and updating will continue for every time increment, i.e., when k is replaced by $k+1$. The process will continue until all the time points are used, i.e., k becomes equal to m , where m represents the total number of discrete time points of the measurements. The iteration process covering all the time points is generally denoted as local iteration. However, the identified parameters obtained through the

local iteration may not be stable and convergent. To obtain the desired results, a weighted global iteration procedure, suggested by Hoshiya and Saito (1984), can be used. To accomplish this, a weight factor w is introduced in the error covariance matrix for the stiffness parameters to be estimated in Equation (10), and the same prediction and updating steps are carried out for all the m time points. Hoshiya and Saito (1984) reported that weight factor played an important role to promote convergence, although it may lead to fluctuations in the state vector in first few iterations. Hoshiya and Saito (1984), Koh et al. (1991), Oreta and Tanabe (1993, 1994) assumed w to be 100. Hoshiya and Sutoh (1993) assumed it to be in the range of 1000 to 10000 in some applications. In a more recent work, Ghosh et al. (2007) assumed w to be 100. In this study w is considered to be 100 or 1000, depending on the application.

The overall process to implement Stage 2 of the GILS-EKF-UI method can be described as follows. Stage 2 is initiated by assuming the initial state vector $\{\hat{Z}_0(t_0/t_0)\}$ and error covariance matrix $[P(t_0/t_0)]$. At the completion of the local iteration, updated information on the corresponding terms, denoted as $\{\hat{Z}^{(1)}(t_m/t_m)\}$ and $[P^{(1)}(t_m/t_m)]$ respectively, will be available. Here, the superscript (1) denotes the first global iteration. To initiate the 2nd global iteration, $\{\hat{Z}^{(2)}(t_0/t_0)\}$ and $[P^{(2)}(t_0/t_0)]$ need to be assumed, say equal to $\{\hat{Z}^{(1)}(t_m/t_m)\}$ and $w[P^{(1)}(t_m/t_m)]$, respectively. On the completion of this iteration, the information on $\{\hat{Z}^{(2)}(t_m/t_m)\}$ and $[P^{(2)}(t_m/t_m)]$ will become available. The global iteration process will continue, until a predetermined convergence criterion is satisfied for the identified structural parameters, i.e., $\left| [K^{(i)}(t_m/t_m)] - [K^{(i-1)}(t_m/t_m)] \right| \leq \varepsilon$, where i represents the global iteration number and ε is the acceptable tolerance level. Since the stiffness parameters in this study are of the order of 100000, ε is considered to be between 10 and 100. In some cases, convergence may not be achieved. In those cases, the minimization of an objective function $\bar{\theta}$ will be necessary (Hoshiya and Saito, 1984). However, this is beyond the scope of this paper. In any case, after the completion of Stage 2, the whole structure is identified by using the response information measured only at the substructure.

EXAMPLE: HEALTH ASSESSMENT OF A 2-D FRAME EXCITED BY EARTHQUAKE GROUND MOTION

A three-story, single-bay, two-dimensional, steel frame shown in Figure 1 is considered to verify the MILS-UI and GILS-EKF-UI methods. The same frame has already been tested in laboratory by exciting it with the sinusoidal and impulsive forces (Martinez-Flores, 2005). The health assessments of defect-free and defective frames by using experimental response information have also been published for this case (Martinez-Flores, 2005; Martinez-Flores and Haldar, 2007; Martinez-Flores et al., 2008).

For completeness in this paper, a brief discussion on the example frame is necessary. This frame has been designed according to the design guidelines of American Institute of Steel Construction's (AISC's) LRFD Manual and scaled to one-third of its actual dimensions to fit the testing facilities. The scaled frame has the bay width of 3.05 m and the story height of 1.22 m. The frame consists of nine members, i.e., six columns and three beams. The steel section of size S4x7.7 has been used for all the beams and columns in order to minimize the effects of fabrication defects and differences in the material properties. Assuming that the bases are fixed, the frame can be represented by 18 DDOFs. The nominal cross-sectional properties of the chosen section are available from any standard steel manual. However, before testing the frame in laboratory, the scenarios considered have been studied analytically in an exhaustive manner. The actual values of cross-sectional area, mass, moment of inertia and damping properties are expected to be different from the nominal values and are therefore determined first as discussed next.

1. Estimation of Actual Cross-Sectional Area

Martinez-Flores (2005) conducted a simple experiment to establish the actual cross-sectional area of the members of the example frame. A test specimen was submerged into a container filled with water, and

by using the information on the displaced water, the average cross-sectional area of the specimen members was estimated to be 14.14 cm^2 . This is less than 3% of the nominal value, and hence, in developing the analytical model the estimated area of 14.14 cm^2 is considered.

2. Estimation of Moment of Inertia

A trial and error method is used to calculate the actual moment of inertia of the structural members. The defect-free frame was excited by a sinusoidal load and acceleration time history was recorded at the top of the frame at Node 2. By using the fast Fourier transform (FFT), the first two natural frequencies were estimated to be $f_1 = 9.76 \text{ Hz}$ and $f_2 = 34.12 \text{ Hz}$. A theoretical finite-element model of the frame was also developed by considering the area of the elements same as that estimated experimentally. The Young's modulus of elasticity of the material was taken as $123.3 \times 10^9 \text{ N/m}^2$. The moment of inertia of the elements was changed so that there was matching between the first two natural frequencies of the experimental and theoretical models. Reasonably good matching was observed between the experimental and theoretical frequencies, when the nominal moment of inertia was reduced by 6%. Therefore, the actual moment of inertia is estimated to be 94% of the nominal moment of inertia, i.e., equal to $0.94 \times 253.9 = 238.7 \text{ cm}^4$.

3. Estimation of Mass

As mentioned above, all the beams and columns have the same cross-sectional area. Hence, to estimate their mass, they are simply weighed and the mass is estimated to be 11.5 kg/m .

4. Estimation of Damping

The logarithmic decrement method is employed to evaluate the amount of viscous damping present in the frame and the damping coefficient ξ for the frame is estimated based on the rate of decay of the oscillatory response of the structure (Clough and Penzien, 1993). The frame was excited by an impulsive load and the acceleration time history at the roof at Node 1 was recorded. This time history was then post-processed and integrated twice to obtain the displacement time history. Assuming damping to be same in the first two modes and following the procedure suggested by Clough and Penzien (1993), the corresponding (problem-specific) Rayleigh damping coefficients are estimated.

5. Generation of Theoretical Responses and Health Assessment of the Frame

The actual stiffness values, $k_i = E_i I_i / L_i$, $i = 1, 2, \dots$, are found to be 96500 N-m for all the beams and 241250 N-m for all the columns. To simulate the gravity load, a uniformly distributed load of 3675 N/m is applied on all the floor beams. The first two natural frequencies of the frame are estimated to be 2.0915 and 7.3063 Hz , and the Rayleigh damping coefficients α and β are estimated to be 0.245404 and 0.000406786 , respectively. The analytical responses of the defect-free frame have been evaluated by using ANSYS, Version 11, a commercially available computer program, for excitation by the recorded acceleration time history of 1994 El Centro earthquake shown in Figure 3.

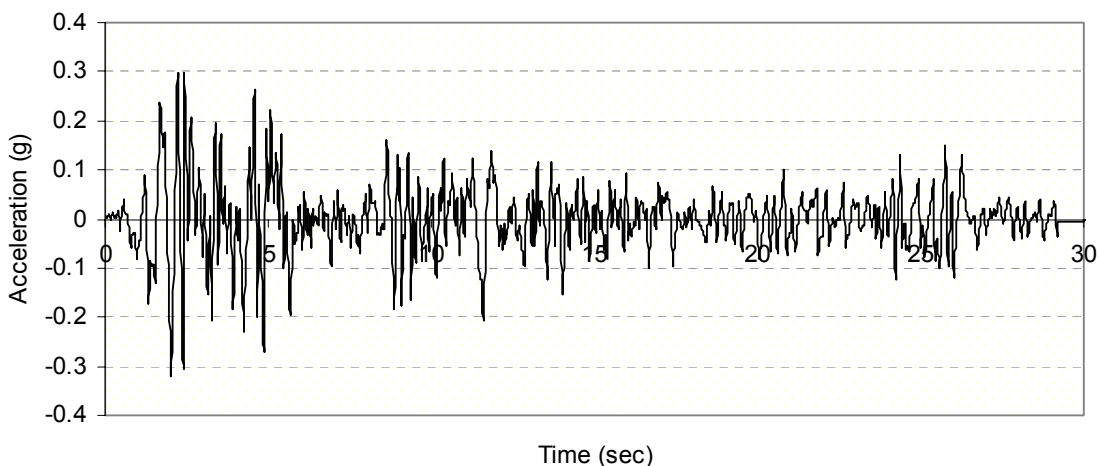


Fig. 3 1994 El Centro earthquake acceleration time history

The displacement, velocity, and acceleration time histories are calculated at each DDOF for the time increment of 0.00025 s for a total duration of 3 s. To consider the defective state of the frame, three scenarios of this state are considered. For the purpose of discussion and on referring to Figure 2(a), these scenarios are (i) Beam 1 is broken, (ii) Beam 2 is broken, and (iii) Beam 3 is broken. To obtain analytical responses for these scenarios, the moment of inertia of the broken beams is considered to be 0.1% of that in the defect-free state. Again, ANSYS, Version 11 is used to estimate the responses at all DDOFs under the same seismic excitation for each scenario. Once the responses have been obtained for both defect-free and defective states, those are considered to be the measured responses and the information on input seismic excitation is completely ignored for the purpose of structural health assessment. It is important to note that the initial finite element representation of the defect-free frame is not changed for the defective states. Therefore, the task is whether the MILS-UI and GILS-EKF-UI methods can identify the locations and severity of defects.

6. Health Assessment of Defect-Free Frame Using the MILS-UI Method

Although theoretical responses are available for a longer duration, the responses between 1.52 and 2.37 s with a sampling interval of 0.01 s are used. While using the responses for all the 18 DDOFs, the stiffness parameters for all the nine members of the defect-free frame are identified by using the MILS-UI method. The identified stiffness parameters are summarized in Table 1. On comparing the identified stiffness parameters with their expected or analytical values, the errors in the identification are found to be very small, i.e., of the order of 0.002%, for all the members. Since the stiffness parameters did not change among all the members, the frame is identified to be defect-free. This indicates that the MILS-UI method accurately identifies the defect-free state of the frame for the seismic excitation considered.

Table 1: Stiffness Parameter Identification for Defect-Free Frame Using MILS-UI Method

| Member <i>i</i> | Stiffness Parameter $k_i (= E_i I_i / L_i)$ Values | | |
|--------------------|--|---------------------|--------------|
| | Nominal (N-m) | Identified (N-m) | Error (%) |
| (1) | (2) | (3) | (4) |
| 1 | 96500 | 96498 | -0.002 |
| 2 | 96500 | 96498 | -0.002 |
| 3 | 96500 | 96498 | -0.002 |
| 4 | 241250 | 241244 | -0.002 |
| 5 | 241250 | 241244 | -0.002 |
| 6 | 241250 | 241244 | -0.002 |
| 7 | 241250 | 241244 | -0.002 |
| 8 | 241250 | 241244 | -0.002 |
| 9 | 241250 | 241244 | -0.002 |

7. Health Assessment for Defective Frame Using the MILS-UI Method

After successfully identifying the defect-free frame, the three scenarios of the defective state of the frame are considered one at a time. For a broken member, its stiffness parameter is supposed to be zero, with the understanding that it is impractical to obtain a zero value for this parameter numerically. Similar to the case of defect-free frame, on using the responses for all the 18 DDOFs between 1.52 and 2.37 s with the sampling interval of 0.01 s, the stiffness parameters for all the members are identified for the three defective states by using the MILS-UI method. The results of identification are summarized in Table 2.

For all the three scenarios of the defective state, the identified stiffness parameters for the broken members are found to be of the order of 100 N-m, as compared to the value of 96500 N-m for the defect-free state of the frame. The stiffness parameters for the other members did not change significantly, thereby indicating the location of the defect. For the three scenarios of the defective state, it is thus found that the MILS-UI method correctly identifies the locations and severity of the defects in the case of seismic excitations.

Table 2: Stiffness Parameter Identification for Broken Members Using MILS-UI Method

| Member <i>i</i> | Stiffness Parameter k_i ($= E_i I_i / L_i$) Values (N-m) | | | |
|--------------------|---|---------------|---------------|---------------|
| | Nominal | Identified | | |
| | | Broken Beam 1 | Broken Beam 2 | Broken Beam 3 |
| (1) | (2) | (3) | (4) | (5) |
| 1 | 96500 | <u>100</u> | 96588 | 96571 |
| 2 | 96500 | 96560 | <u>101</u> | 96574 |
| 3 | 96500 | 96562 | 96595 | <u>100</u> |
| 4 | 241250 | 241400 | 241473 | 241430 |
| 5 | 241250 | 241400 | 241473 | 241430 |
| 6 | 241250 | 241405 | 241488 | 241436 |
| 7 | 241250 | 241405 | 241488 | 241436 |
| 8 | 241250 | 241406 | 241491 | 241440 |
| 9 | 241250 | 241406 | 241491 | 241440 |

8. Health Assessment for Defect-Free Frame Using GILS-EKF-UI Method

While considering the substructure shown in Figure 2(b) and using only the responses at its 9 DDOFs, the whole defect-free frame is identified by using the GILS-EKF-UI method. Based on the prior experience, the sampling interval is considered to be 0.00025 s to implement the procedure. By using the responses between 1.52 and 2.37 s, the substructure of the defect-free frame is first identified and the results are shown in Table 3(a). These results indicate that the stiffness parameters of the beam and column in the substructure are identified quite accurately in Stage 1. The unknown input ground acceleration is also identified accurately, as shown in Figure 4.

By using the information generated in Stage 1 (based on the responses at 9 DDOFs), the whole frame is identified in Stage 2. The different amounts of noises in the measured responses are considered by changing the diagonal terms of the covariance matrix $[R_{t_k}]$. The results corresponding to the diagonal values of 10^{-2} and 10^{-4} are summarized in Table 3(b) (see Columns 3 and 4, respectively). As expected, the errors in the identification are observed to go up with an increase in the noise level in the responses.

It is obvious that the total number of responses used to identify a structure will determine the accuracy in the predictions. For seismic excitations, the horizontal responses are expected to control the structural behavior and therefore the stiffness parameters are identified again by additionally considering the horizontal responses at Nodes 4, 5 and 6 (in addition to the responses at the 9 DDOFs of the substructure). The identified stiffness parameters for all the members are given in Table 3(b) (see Columns 5 and 6 for the diagonal terms of 10^{-2} and 10^{-4} , respectively, in the covariance matrix $[R_{t_k}]$). The corresponding maximum errors in the stiffness parameter identification are found to be 3.6% and 3.05%, respectively. This exercise clearly indicates the value of considering additional responses; the cost may go up but predictability will be improved. Further, it is observed that the identified stiffness parameters do not change significantly from member to member, which indicates that the frame is defect-free.

9. Health Assessment for Defective Frame Using GILS-EKF-UI Method

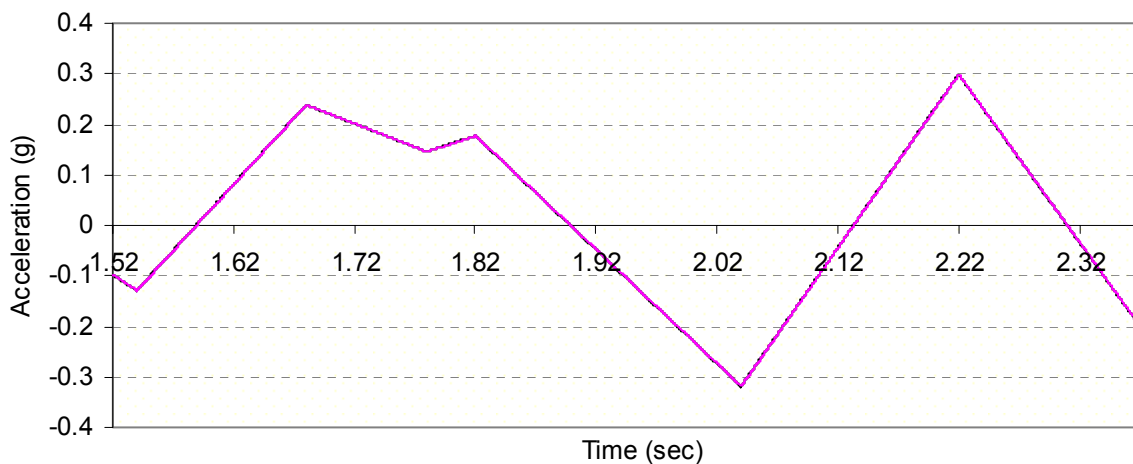
Considering the same three scenarios of the defective state as discussed earlier and the responses measured between 1.52 and 2.37 s with the sample interval of 0.00025 s, the frame is identified. It may be noted that for the first scenario, the substructure contains the defect. Table 4(a) shows that the identified results for Stage 1 are very accurate for all the three scenarios. The results for the identified stiffness parameters for the whole frame, as obtained by using the responses at the 12 DDOFs, are shown in Table 4(b). In some cases, the identified stiffness parameters for the broken members are observed to be negative, and in all cases, they are very small, thus indicating the locations and severity of defects. The identified results for the first scenario clearly indicate that the defect has been identified more accurately. This observation suggests that the proximity of the defect to the substructure may be an important defect identification parameter. This needs to be investigated more extensively. In any case, the locations and

severity of the defects in all the three cases have been identified correctly for the seismic excitations also. This study thus confirms that the GILS-EKF-UI method is robust and that this can identify structural health for different types of excitations.

Table 3: Stiffness Parameter Identification for Defect-Free Frame Using GILS-EKF-UI Method: (a) Stage 1—Substructure Identification; (b) Stage 2—Identification of Whole Structure

| (a) | | | |
|-----------------|--|------------------|-----------|
| Member <i>i</i> | Stiffness Parameter $k_i (= E_i I_i / L_i)$ Values | | |
| | Nominal (N-m) | Identified (N-m) | Error (%) |
| (1) | (2) | (3) | (4) |
| 1 | 96500 | 96498 | -0.002 |
| 4 | 241250 | 241244 | -0.002 |

| (b) | | | | | |
|-----------------|--|--|--|--|--|
| Member <i>i</i> | Stiffness Parameter $k_i (= E_i I_i / L_i)$ Values (N-m) | | | | |
| | Nominal | Identified | | | |
| | | 9 DDOFs | | 12 DDOFs | |
| | | Diagonal $[R_{t_k}]$ Value = 10^{-2} | Diagonal $[R_{t_k}]$ Value = 10^{-4} | Diagonal $[R_{t_k}]$ Value = 10^{-2} | Diagonal $[R_{t_k}]$ Value = 10^{-4} |
| (1) | (2) | (3) | (4) | (5) | (6) |
| 1 | 96500 | 102005 | 96946 | 97216 | 96225 |
| 2 | 96500 | 84888 | 94334 | 95123 | 96893 |
| 3 | 96500 | 111356 | 79379 | 98044 | 94840 |
| 4 | 241250 | 250776 | 229117 | 241853 | 237739 |
| 5 | 241250 | 277351 | 238014 | 245891 | 239033 |
| 6 | 241250 | 118007 | 182932 | 233237 | 242091 |
| 7 | 241250 | 176952 | 208766 | 249935 | 248598 |
| 8 | 241250 | 172766 | 496563 | 238373 | 247199 |
| 9 | 241250 | 431023 | 165941 | 239774 | 240178 |



— Theoretical Seismic Excitation — Identified Seismic Excitation

Fig. 4 Theoretical and identified seismic excitations

Table 4: Stiffness Parameter Identification for Broken Members Using GILS-EKF-UI Method: (a) Stage 1—Substructure Identification; (b) Stage 2—Identification of Whole Structure

| (a) | | | | | | | |
|--------------------|--|---------------------|--------------|---------------------|--------------|---------------------|--------------|
| Member <i>i</i> | Stiffness Parameter $k_i (= E_i I_i / L_i)$ Values | | | | | | |
| | Nominal (N-m) | Broken Beam 1 | | Broken Beam 2 | | Broken Beam 3 | |
| | | Identified (N-m) | Error (%) | Identified (N-m) | Error (%) | Identified (N-m) | Error (%) |
| (1) | (2) | (3) | (4) | (5) | (6) | (7) | (8) |
| 1 | 96500 | 100 | -99.896 | 96498 | -0.002 | 96498 | -0.002 |
| 4 | 241250 | 241410 | 0.066 | 241244 | -0.002 | 241245 | -0.002 |

| (b) | | | | | | | |
|---|--|---|---|---|---|---|--------|
| Member <i>i</i> | Stiffness Parameter $k_i (= E_i I_i / L_i)$ Values | | | | | | |
| | Nominal | (N-m) | | | | | |
| | | Identified | | | | | |
| | | Broken Beam 1 | | Broken Beam 2 | | Broken Beam 3 | |
| Diagonal $[R_k]$ Value = 10^{-2} | | Diagonal $[R_k]$ Value = 10^{-4} | Diagonal $[R_k]$ Value = 10^{-2} | Diagonal $[R_k]$ Value = 10^{-4} | Diagonal $[R_k]$ Value = 10^{-2} | Diagonal $[R_k]$ Value = 10^{-4} | |
| (1) | (2) | (3) | (4) | (5) | (6) | (7) | (8) |
| 1 | 96500 | -66 | 442 | 94845 | 94798 | 98561 | 95194 |
| 2 | 96500 | 96733 | 95985 | 1030 | 1034 | 93255 | 98702 |
| 3 | 96500 | 97431 | 96235 | 94740 | 94778 | 2415 | -2104 |
| 4 | 241250 | 243439 | 236935 | 235530 | 234816 | 243379 | 236311 |
| 5 | 241250 | 243945 | 237021 | 233756 | 233889 | 253192 | 233666 |
| 6 | 241250 | 236679 | 240039 | 233788 | 236803 | 227883 | 245882 |
| 7 | 241250 | 242972 | 245101 | 248438 | 245556 | 253281 | 240446 |
| 8 | 241250 | 226651 | 250292 | 245453 | 249306 | 230783 | 250677 |
| 9 | 241250 | 253244 | 234827 | 244920 | 241031 | 235759 | 248391 |

CONCLUSIONS

Conceptual bases for the two vibration-based structural health assessment procedures, denoted as MILS-UI and GILS-EKF-UI methods, under development by the research team at the University of Arizona have been presented. Both procedures were analytically and experimentally verified in the past for the sinusoidal and impulsive excitations. They have been analytically verified for the seismic excitations by using the numerically generated response information in this paper to establish their robustness. Both methods are finite-element based and use dynamic response information to identify the defective elements. The MILS-UI method is considered to be more appropriate for the SHA of small systems. Since the GILS-EKF-UI method can assess structural health by using the responses measured at limited locations in the structure, it is considered to be more appropriate for large structural systems. This study also indicates that the selection of the location of the substructure is an important parameter to identify defects. Hence, for large structural systems, multiple substructures may be necessary. This needs to be investigated further. Nevertheless, this study confirms the robustness of both the procedures and indicates great implementation potential of these procedures to assess the structural health of real structures.

REFERENCES

1. Ahmed, N.H. (2009). "Dynamic State Estimation Techniques for Identification of Parameters of Finite Element Structural Models", Ph.D. Thesis, Department of Civil Engineering, Indian Institute of Science, Bangalore.
2. Clough, R.W. and Penzien, J. (1993). "Dynamics of Structures", McGraw-Hill, Inc., New York, U.S.A.
3. Corigliano, A. and Mariani, S. (2004). "Parameter Identification in Explicit Structural Dynamics: Performance of the Extended Kalman Filter", *Computer Methods in Applied Mechanics and Engineering*, Vol. 193, No. 36-38, pp. 3807–3835.
4. Doebbling, S.W., Farrar, C.R., Prime, M.B. and Shevitz, D.W. (1996). "Damage Identification and Health Monitoring of Structural and Mechanical Systems from Changes in Their Vibration Characteristics: A Literature Review", Report LA-13070-MS, Los Alamos National Laboratory, Los Alamos, U.S.A.
5. Ghanem, R. and Ferro, G. (2006). "Health Monitoring for Strongly Non-linear Systems Using the Ensemble Kalman Filter", *Structural Control and Health Monitoring*, Vol. 13, No. 1, pp. 245–259.
6. Ghanem, R. and Shinozuka, M. (1995). "Structural-System Identification. I: Theory", *Journal of Engineering Mechanics*, ASCE, Vol. 121, No. 2, pp. 255–264.
7. Ghosh, S.J., Roy, D. and Manohar, C.S. (2007). "New Forms of Extended Kalman Filter via Transversal Linearization and Applications to Structural System Identification", *Computer Methods in Applied Mechanics and Engineering*, Vol. 196, No. 49-52, pp. 5063–5083.
8. Haldar, A. (2009). "Structural Health Assessment Using Noise-Contaminated Minimum Dynamic Response Information" in "Frontier Technologies for Infrastructures Engineering (edited by S.-S. Chen and A.H.-S. Ang)", CRC Press/Balkema, Leiden, The Netherlands.
9. Haldar, A. and Das, A.K. (2010). "Prognosis of Structural Health–Nondestructive Methods", *International Journal of Performability Engineering*, Vol. 6, No. 5, pp. 487–498.
10. Haldar, A., Martinez-Flores, R. and Katkhuda, H. (2008). "Crack Detection in Existing Structures Using Noise-Contaminated Dynamic Responses", *Theoretical and Applied Fracture Mechanics*, Vol. 50, No. 1, pp. 74–80.
11. Hoshiya, M. and Saito, E. (1984). "Structural Identification by Extended Kalman Filter", *Journal of Engineering Mechanics*, ASCE, Vol. 110, No. 12, pp. 1757–1770.
12. Hoshiya, M. and Sutoh, A. (1993). "Kalman Filter—Finite Element Method in Identification", *Journal of Engineering Mechanics*, ASCE, Vol. 119, No. 2, pp. 197–210.
13. Housner, G.W., Bergman, L.A., Caughey, T.K., Chassiakos, A.G., Claus, R.O., Masri, S.F., Skelton, R.E., Soong, T.T., Spencer, B.F. and Yao, J.T.P. (1997). "Structural Control: Past, Present, and Future", *Journal of Engineering Mechanics*, ASCE, Vol. 123, No. 9, pp. 897–971.
14. Humar, J., Bagchi, A. and Xu, H. (2006). "Performance of Vibration-Based Techniques for the Identification of Structural Damage", *Structural Health Monitoring*, Vol. 5, No. 3, pp. 215–241.
15. Jazwinski, A.H. (1970). "Stochastic Processes and Filtering Theory", Academic Press, Inc., New York, U.S.A.
16. Katkhuda, H.N. (2004). "In-Service Health Assessment of Real Structures at the Element Level with Unknown Input and Limited Global Responses", Ph.D. Dissertation, Department of Civil Engineering and Engineering Mechanics, University of Arizona, Tucson, U.S.A.
17. Katkhuda, H. and Haldar, A. (2006). "Defect Identification under Uncertain Blast Loading", *Optimization and Engineering*, Vol. 7, No. 3, pp. 277–296.
18. Katkhuda, H. and Haldar, A. (2008). "A Novel Health Assessment Technique with Minimum Information", *Structural Control and Health Monitoring*, Vol. 15, No. 6, pp. 821–838.
19. Katkhuda, H., Martinez, R. and Haldar, A. (2005). "Health Assessment at Local Level with Unknown Input Excitation", *Journal of Structural Engineering*, ASCE, Vol. 131, No. 6, pp. 956–965.
20. Kerschen, G., Worden, K., Vakakis, A.F. and Golinval, J.-C. (2006). "Past, Present and Future of Nonlinear System Identification in Structural Dynamics", *Mechanical Systems and Signal Processing*, Vol. 20, No. 3, pp. 505–592.

21. Koh, C.G., See, L.M. and Balendra, T. (1991). "Estimation of Structural Parameters in Time Domain: A Substructure Approach", *Earthquake Engineering & Structural Dynamics*, Vol. 20, No. 8, pp. 787–801.
22. Lew, J.-S., Juang, J.-N. and Longman, R.W. (1991). "Comparison of Several System Identification Methods for Flexible Structures", *Proceedings of the AIAA/ASME/ASCE/AHS/ASC 32nd Structures, Structural Dynamics, and Materials Conference*, Baltimore, U.S.A., pp. 2304–2318.
23. Ling, X. and Haldar, A. (2004). "Element Level System Identification with Unknown Input with Rayleigh Damping", *Journal of Engineering Mechanics*, ASCE, Vol. 130, No. 8, pp. 877–885.
24. Martinez-Flores, R. (2005). "Damage Assessment Potential of a Novel System Identification Technique—Experimental Verification", Ph.D. Dissertation, Department of Civil Engineering and Engineering Mechanics, University of Arizona, Tucson, U.S.A.
25. Martinez-Flores, R. and Haldar, A. (2007). "Experimental Verification of a Structural Health Assessment Method without Excitation Information", *Journal of Structural Engineering*, SERC, Vol. 34, No. 1, pp. 33–39.
26. Martinez-Flores, R., Katkhuda, H. and Haldar, A. (2008). "Structural Performance Assessment with Minimum Uncertainty-Filled Information", *International Journal of Performability Engineering*, Vol. 4, No. 2, pp. 121–140.
27. Maruyama, O. and Hoshiya, M. (2001). "System Identification of an Experimental Model by Extended Kalman Filter", *Proceedings of the 8th International Conference on Structural Safety and Reliability (ICOSSAR '01)*, Newport Beach, U.S.A., Paper No. 12-2 (on CD).
28. Maybeck, P.S. (1979). "Stochastic Models, Estimation, and Control: Volume 1", Academic Press, Inc., New York, U.S.A.
29. Oreta, A.W.C. and Tanabe, T. (1993). "Localized Identification of Structures by Kalman Filter", *Structural Engineering/Earthquake Engineering*, JSCE, Vol. 9, No. 4, pp. 217s–225s.
30. Oreta, A.W.C. and Tanabe, T. (1994). "Element Identification of Member Properties of Framed Structures", *Journal of Structural Engineering*, ASCE, Vol. 120, No. 7, pp. 1961–1976.
31. Rytter, A. (1993). "Vibration Based Inspection of Civil Engineering Structures", Ph.D. Thesis, Department of Building Technology and Structural Engineering, Aalborg University, Aalborg, Denmark.
32. Saha, N. and Roy, D. (2009). "Extended Kalman Filters Using Explicit and Derivative-Free Local Linearizations", *Applied Mathematical Modelling*, Vol. 33, No. 6, pp. 2545–2563.
33. Shinozuka, M. and Ghanem, R. (1995). "Structural System Identification. II: Experimental Verification", *Journal of Engineering Mechanics*, ASCE, Vol. 121, No. 2, pp. 265–273.
34. Vo, P.H. and Haldar, A. (2003). "Post-processing of Linear Accelerometer Data in Structural Identification", *Journal of Structural Engineering*, SERC, Vol. 30, No. 2, pp. 123–130.
35. Vo, P.H. and Haldar, A. (2004). "Health Assessment of Beams—Experimental Investigations", *Journal of Structural Engineering*, SERC, Vol. 31, No. 1, pp. 23–30.
36. Vo, P.H. and Haldar, A. (2008a). "Health Assessment of Beams—Theoretical Formulation and Analytical Verification", *Structure and Infrastructure Engineering*, Vol. 4, No. 1, pp. 33–44.
37. Vo, P.H. and Haldar, A. (2008b). "Health Assessment of Beams—Experimental Verification", *Structure and Infrastructure Engineering*, Vol. 4, No. 1, pp. 45–56.
38. Wang, D. and Haldar, A. (1994). "Element-Level System Identification with Unknown Input", *Journal of Engineering Mechanics*, ASCE, Vol. 120, No. 1, pp. 159–176.
39. Wang, D. and Haldar, A. (1997). "System Identification with Limited Observations and without Input", *Journal of Engineering Mechanics*, ASCE, Vol. 123, No. 5, pp. 504–511.
40. Welch, G. and Bishop, G. (1995). "An Introduction to the Kalman Filter", Report TR95-041, Department of Computer Science, University of North Carolina at Chapel Hill, Chapel Hill, U.S.A.
41. Worden, K., Farrar, C.R., Manson, G. and Park, G. (2007). "The Fundamental Axioms of Structural Health Monitoring", *Proceedings of the Royal Society A*, Vol. 463, No. 2082, pp. 1639–1664.

42. Worden, K., Farrar, C.R., Haywood, J. and Todd, M. (2008). "A Review of Nonlinear Dynamics Applications to Structural Health Monitoring", *Structural Control and Health Monitoring*, Vol. 15, No. 4, pp. 540–567.
43. Wu, M. and Smyth, A.W. (2007). "Application of the Unscented Kalman Filter for Real-Time Nonlinear Structural System Identification", *Structural Control and Health Monitoring*, Vol. 14, No. 7, pp. 971–990.
44. Yang, J.N., Lin, S., Huang, H. and Zhou, L. (2006). "An Adaptive Extended Kalman Filter for Structural Damage Identification", *Structural Control and Health Monitoring*, Vol. 13, No. 4, pp. 849–867.
45. Yang, J.N., Pan, S. and Huang, H. (2007). "An Adaptive Extended Kalman Filter for Structural Damage Identifications II: Unknown Inputs", *Structural Control and Health Monitoring*, Vol. 14, No. 3, pp. 497–521.
46. Zhou, L., Wu, S. and Yang, J.N. (2008). "Experimental Study of an Adaptive Extended Kalman Filter for Structural Damage Identification", *Journal of Infrastructure Systems, ASCE*, Vol. 14, No. 1, pp. 42–51.

INVESTIGATION AND ANALYSIS OF SEISMIC WAVE PARAMETERS OF SEISMIC GAP, SEISMIC BELT AND FORESHOCK

Wenlong Liu*, Yucheng Liu**, Yonglin Xu*, Chun Zhang*, Huan Zhang*, Weidong Shen* and Weixing Zhong*

*Earthquake Administration of Shanghai Municipality
Shanghai 200062, China

**Department of Mechanical Engineering, University of Louisiana
Lafayette, LA 70504, U.S.A.

ABSTRACT

Four earthquakes with magnitudes around M 6.0, which occurred in southeastern China since 1970, are studied based on six seismic wave parameters. These parameters include the rupture characteristic L_0/L , primary rupture directions, the ambient shear stress τ , the temporal periodicity of waveform, r , Q values for P-waves, and the width of Fourier spectrum, w . In this study, the six parameters for each earthquake are calculated, compared, and investigated in order to define single foreshocks. Errors caused by the digitization of analog records and application of simplified hypocenter and medium models, as well as the errors generated in measuring earthquake magnitude and hypocentral radius, are estimated and discussed. Primary characteristics of the earthquakes that occurred within the seismogenic zones and seismic belts are presented after processing 510 charts, 135 earthquakes, and 1030 records.

KEYWORDS: Rupture Characteristics, Ambient Stress, Seismic Gap, Seismic Belt, Foreshock

INTRODUCTION

Since the late 1970s, the earthquake activity method has been fully developed in China and used as the most important method for predicting earthquakes. In this method, earthquakes are predicted based on the seismic gap, seismic belt, and foreshock. A seismic gap is a segment of an active fault that has not slipped in an unusually long time, when compared with the other segments along the same structure. A seismic belt is a narrow geographic zone on the Earth's surface, along which most earthquake activity occurs. A foreshock is a minor earthquake preceding a major earthquake.

The seismic gap hypothesis states that earthquake hazard increases with time since the last large earthquake on certain faults or plate boundaries. The applications of the seismic gap theory to earthquake forecasting were fully demonstrated by Kagan and Jackson (1991, 1995) and Lahr and Plafker (1980). In the earthquake activity method, anomalies in the seismic gap and belt have long been considered as possible precursors of the mid-strong earthquakes. Peacock et al. (1988) observed the temporal variations of shear wave splitting in the Anza seismic gap, Southern California, and used the wave splitting to monitor the detailed changes in the build-up of stress before an earthquake. Davies et al. (1981) expected a great earthquake occurring along the Alaska-Aleutian plate boundary within a reasonable span of time, based on a thorough investigation of the Shumagin seismic gap. Kostoglodov et al. (2003) measured the parameters of the Guerrero seismic gap, and based on the results they initiated a reassessment of the seismic potential of Guerrero and other seismic gaps in Mexico. Seismic gaps and belts have also been used for predicting long-term earthquakes in Gansu, China (Gaudemer et al., 1995) and east of Guadeloupe (Dorel, 1981).

The determination of the seismic gap and belt has suffered from subjective arbitrariness, which leads to errors and omissions in the earthquake prediction. Also, the single foreshock of the main shock cannot be identified out of the earthquake sequences, which have occurred before the main shock, by using the seismic activity method (the single foreshock is a conventional term used in seismology). It is known that the abnormal phenomena of the seismic gap, belt and foreshock are the results of the variations of stress conditions and medium characteristics in the hypocenter area. The information on these variations must be carried by the seismic wave. Therefore, by identifying and extracting the information from the seismic wave, an earthquake can be predicted more accurately and its physical mechanism can also be described.

EARTHQUAKE SAMPLES

Since 1970s there have been four earthquakes with magnitudes around 6.0 in southeastern China, which were recorded clearly and completely. Those earthquakes are (a) M 6.0 earthquake near Liyang, Jiangsu province on July 9, 1979, (b) M 5.9 earthquake near Heze, Shandong province on November 7, 1983, (c) M 6.2 earthquake in southern Yellow Sea on May 21, 1984, and (d) M 6.1 and M 6.2 earthquakes in northern Gulf on December 31, 1994 and January 10, 1995, respectively (see Figure 1).



Fig. 1 Distribution of earthquake samples

For each of the above earthquakes, the anomalous seismicity pattern of the earthquake is studied as well as the space-time-range of the earthquake, based on the data given in Zhang et al. (1990a, 1990b) and Chen et al. (2002). In order to investigate the radiation of seismic waves during foreshocks, two foreshocks are selected: (a) the magnitude 4.6 earthquake that occurred in Lishui, Jiangsu province on May 10, 1977 (i.e., the foreshock of the Liyang earthquake), and (b) the magnitude 4.8 earthquake that occurred in Ci County, Hebei province on May 29, 1982 (i.e., the foreshock of the Heze earthquake). It needs to be mentioned that there is no universal quantitative criterion for distinguishing what is anomalous from what is normal, because different regions have different geological features and assume different normal seismicity patterns. Therefore, we have been continuously monitoring the seismic parameters over those areas and taking the values during seismically quiet periods as their normal values. Once we find that one or more parameter values distinctly deviate from their normal values, we consider those as “anomalies” and start to investigate whether those “anomalies” were associated with a potential earthquake.

In selecting the appropriate seismic records and seismograms, we have chosen for digitization the analog data recorded by those seismic observatories, whose epicentral distances were greater than 100 km. The selected data are clear and complete, and vary in appropriate ranges, which is suitable for further analysis. Also, for each of the above earthquakes, in order to determine the rupture characteristics of the earthquake, related seismic records have been read from at least three seismic observatories. Those observatories evenly surround the epicenter, and the field angle of the two farthest observatories and the epicenter is greater than 60° .

1. Applied Methods

1.1 Rupture Characteristics of Medium and Small Earthquakes

Earthquake's rupture characteristics include unilateral rupture or bilateral rupture, and primary rupture direction for the unilateral rupture. Liu et al. (1996) presented a method of using directional function to determine the earthquake's rupture characteristics. This method is described as follows.

We consider an asymmetric bilateral rupture (see Figure 2), whose rupture propagation velocity is v_f , the rupture lengths of the two sides are L_0 and L_π , focal depth h is 0, and the epicentral distance of the seismic observatory is r . The P-wave spectrum of far-field radiation at the seismic observatory is

$$U_r(\omega) = \frac{m_0}{4\pi\rho v_p^3 r} R_\alpha i\omega G(\omega) e^{\frac{i\omega r}{v_p}} \left(\frac{L_0}{L} e^{-ix_0} \frac{\sin x_0}{x_0} + \frac{L_\pi}{L} e^{-ix_\pi} \frac{\sin x_\pi}{x_\pi} \right) \quad (1)$$

where m_0 is the seismic moment, v_p is the P-wave velocity, R_α is the radiation pattern factor, and

$$x_0 = \frac{\omega L_0}{2} \left(\frac{1}{v_f} - \frac{\cos \theta}{v_p} \right) \quad (2a)$$

$$x_\pi = \frac{\omega L_\pi}{2} \left(\frac{1}{v_f} + \frac{\cos \theta}{v_p} \right) \quad (2b)$$

$$R_\alpha = \sin 2\theta \quad (2c)$$

$$L = L_0 + L_\pi \quad (2d)$$

Let the earthquake be recorded by the seismic observatories 1 and 2, and let the epicentral distances of the two observatories be equal to each other (as shown in Figure 2). We assume that the seismogenic fault is a vertical strike-slip fault whose depth is zero, and that both stations are located in the YZ-plane. It is also assumed that the stations 1 and 2 are located on the two lines emanating from the hypocenter along the reverse directions (therefore, the angles between the two stations are θ and $\theta + \pi$, respectively). Then, the ratio between the amplitude spectra obtained from the two observatories can be defined by using a directional function D expressed as

$$D = \left| \frac{U_1(\omega)}{U_2(\omega)} \right| = \left| \frac{e^{-ix_{10}} \sin x_{10} \left(\frac{1}{v_f} + \frac{\cos \theta}{v_p} \right) + e^{-ix_{1\pi}} \sin x_{1\pi} \left(\frac{1}{v_f} - \frac{\cos \theta}{v_p} \right)}{e^{-ix_{20}} \sin x_{20} \left(\frac{1}{v_f} + \frac{\cos \theta}{v_p} \right) + e^{-ix_{2\pi}} \sin x_{2\pi} \left(\frac{1}{v_f} - \frac{\cos \theta}{v_p} \right)} \right| \quad (3)$$

If the field angle between the lines from both observatories to the epicenter is denoted as α ($\neq \pi$), then the ratio between the two amplitude spectra can be defined as a generalized directional function D_G where

$$D_G = \left| \frac{\sin 2\theta \left(\frac{1}{v_f} + \frac{\cos(\theta + \alpha)}{v_p} \right) \left(\frac{1}{v_f} - \frac{\cos(\theta + \alpha)}{v_p} \right)}{\sin 2(\theta + \alpha) \left(\frac{1}{v_f} + \frac{\cos \theta}{v_p} \right) \left(\frac{1}{v_f} - \frac{\cos \theta}{v_p} \right)} \right| \times \left| \frac{e^{-ix_{10}} \sin x_{10} \left(\frac{1}{v_f} + \frac{\cos \theta}{v_p} \right) + e^{-ix_{1\pi}} \sin x_{1\pi} \left(\frac{1}{v_f} - \frac{\cos \theta}{v_p} \right)}{e^{-ix_{20}} \sin x_{20} \left(\frac{1}{v_f} + \frac{\cos(\theta + \alpha)}{v_p} \right) + e^{-ix_{2\pi}} \sin x_{2\pi} \left(\frac{1}{v_f} - \frac{\cos(\theta + \alpha)}{v_p} \right)} \right| \quad (4)$$

From Equation (4), it can be observed that D_G is a function of ω with the parameters α , L_0/L , and θ . As shown in Figure 2 (where the horizontal plane XZ is the fault plane), θ is the azimuth angle between the station 1 and Y-axis (i.e., the vertical direction), and α is the azimuth angle between the observatories 2 and 1. The parameters, L_0/L and θ , can be obtained from field surveying, and once we have those values, a D_G curve can be easily plotted. It needs to be mentioned that in Figure 2, the used coordinate system is not with reference to the geographical coordinates but to the hypocentral coordinates, with the fault plane being a horizontal plane where the rupture propagates along its vertical direction (i.e., the Y-axis). Here, the vertical direction is determined from the hypocentral coordinate system, instead of the geographical coordinate system. The hypocentral coordinate system has been created based on the origin of hypocenter, which is a popular system used in seismology (Giovambattista and Barba, 1997). In determining the primary rupture direction based on the records of two observatories, we first measure the field angle α . Next, we choose six L_0/L values from 0.5 to 1.0 with the increment of 0.1, and 12 values of θ from 0° to 180° with the increment of 15° . Based on these parameters, ($6 \times 12 =$) 72 generalized directional function curves are calculated from Equation (4). The calculated curves are then compared with the curve recorded by the observatory 1 to find the closest calculated curve and the corresponding values of L_0/L and θ . Two candidates for the primary rupture directions can be obtained by adding/subtracting θ to/from the geographic azimuth of the observatory 1, and one of these must be the true primary rupture direction. If the records of more than three observatories are available, we will be able to obtain more than two generalized directional functions D_G and more than four candidates for the primary rupture directions by following this method. The candidate directions and rupture azimuths are counted based on the four quadrants, and the quadrant where most rupture azimuths are located is selected. The average value of the rupture azimuths in the selected quadrant is then calculated and specified as the primary rupture direction of the earthquake.

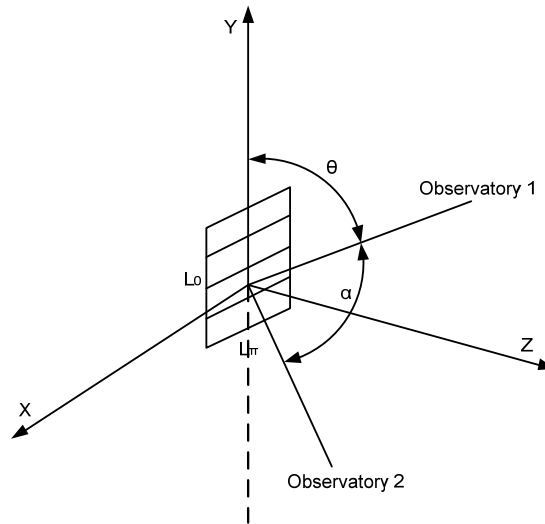


Fig. 2 Asymmetric bilateral rupture (the observatories 1 and 2 are located in the YZ-plane)

1.2 Ambient Shear Stress

The ambient shear stress values can be determined by employing Chen's method (Chen et al., 1977, 1978), because the actual source mechanism of the earthquake samples considered is close to being a horizontal slip. As shown by Chen et al. (1977), the 2-D plane-strain crack mode II can be used to simulate the strike-slip fault and rupture mechanics can be employed to study the earthquake's rupture process to approximate the relationships among the hypocentral parameters and stress conditions as

$$m_s = 2 \log(2r_a) + \frac{1}{1.5} \left(\frac{\log 4(1-\nu)\tau^2\eta}{3(2-\nu)\mu} - 11.8 \right) \quad (5)$$

$$\frac{D}{2r_a} = \frac{4(1-\nu)\tau^2}{3(2-\nu)\pi\mu\tau_y} \quad (6)$$

$$m_0 = \frac{(1-\nu)\pi\tau^2(2r_a)^3}{3(2-\nu)\tau_y} \quad (7)$$

In these equations r_a is the radius of the rupture circle, ν is the Poisson's ratio (= 0.252 for the crust), μ is the shear modulus (= 33 GPa for the crust), τ denotes the ambient shear stress, η denotes the seismic-wave radiation efficiency (taken as 0.05 in this study), D means the average dislocation, τ_y is the yield strength (taken in this study as 200 MPa for the crust), m_0 is the seismic moment, and m_s denotes the surface wave magnitude. Here, the crack mode II is considered to be the sliding or in-plane shear mode, where the crack surfaces slide over one another in a direction perpendicular to the leading edge of the crack.

By using the dislocation model of circular shear to simulate the medium and small strike-slip earthquakes, taking samples from the seismogram, and then by performing the Fourier analyses, the source spectra can be obtained. From each of these spectra, the spectral amplitude in the lower frequency band, $u(\omega)_{\omega \rightarrow 0}$, and the corner frequency f_{ca} can be obtained, and then, the seismic moment m_0 can be determined from

$$u(\omega)_{\omega \rightarrow 0} = \frac{m_0}{4\pi\rho v_p^3 r_e} R_\alpha \quad (8)$$

Here, ρ is the density of the medium (taken in this study as 2.7×10^3 kg/m³ for the crust), r_e is the epicentral distance, the radiation pattern $R_\alpha = \sin 2\theta \cos \varphi$ (if θ and φ are unknown, for small and medium earthquakes we can take the average radiation pattern calculated over the focal sphere), which becomes 4/15 for the P-wave (Venkataraman, 2002), and v_p means the P-wave velocity (taken in this study as 5.7 km/s within the crust; Lidaka et al., 2009). The radius of rupture circle, r_a , can be calculated from the corner frequency f_{ca} since

$$f_{ca} = \frac{0.60}{\left[r_a \left(\frac{1}{v_f} + \frac{\pi}{4v_p} \right) \right]} \quad (9)$$

In Equation (9) the rupture propagation velocity v_f is equal to $0.775 v_s$, where v_s is the S-wave velocity (taken in this study as 3.38 km/s within the crust; Wu et al., 1997). Finally, the ambient shear stress τ can be calculated by using the obtained values of m_0 and r_a in Equation (7). Here, we consider the earthquakes with $M < 3.0$ as "small" earthquakes and the earthquakes with $3.0 < M < 6.0$ as "medium" earthquakes.

1.3 Temporal Periodicity of Waveform

A method for determining the temporal periodicity waveform, r , has been proposed by Feng and Yu (1994). According to this method, a certain number of time instants, t_1, t_2, \dots, t_n , at which the amplitude of displacement or velocity reaches its peak, trough, or zero value, are recorded since the first arrival of P- or S-wave and until one or two wave groups end. The time t_i and the sequence number i are linearly related as

$$t_i = a + b_i \quad (10)$$

where

$$a = \frac{\sum i t_i \sum i - \sum t_i \sum i}{(\sum i)^2 - n \sum i^2} \quad (11)$$

$$b = \frac{n \sum i t_i - \sum t_i \sum i \left(i - \frac{\sum i}{n} \right)}{(\sum i)^2 - n \sum i^2} \quad (12)$$

The errors in these estimates of a and b are expressed in terms of their standard deviations estimated as

$$\sigma_a = \sigma_b \frac{\sqrt{\sum i^2}}{n} \quad (13)$$

$$\sigma_b = \frac{(n-1) \sqrt{\sum \left(t_i - \frac{\sum t_i}{n} \right)^2}}{n(n-2) \sum \left(i - \frac{\sum i}{n} \right)^2} \quad (14)$$

The temporal periodicity of waveform, r , is then calculated by using the least squares method as

$$r = \frac{\sum \left[\left(t_i - \frac{\sum t_i}{n} \right) \left(i - \frac{\sum i}{n} \right) \right]}{\sqrt{\sum \left(t_i - \frac{\sum t_i}{n} \right)^2 \sum \left(i - \frac{\sum i}{n} \right)^2}} \quad (15)$$

More the waveform deviates from the periodic function, more complicated the rupture process is and higher is the unevenness of the medium and stress distributions at the hypocenter, thus leading to a smaller r . This implies that r is a measure of the complexity of the medium and stress field.

1.3.1 Q Values for P Waves

We assume that a seismic observatory has recorded n earthquakes in one area and that the wave spectrum of the i th earthquake is given by

$$Ai(\varpi) = Ai_0(\varpi) G(Ri) I(\varpi) e^{-\frac{\varpi Ri}{2v_p Q}} \quad (16)$$

where $Ai_0(\varpi)$ is the seismic wave spectrum for the hypocenter, $G(Ri)$ represents the geometric spreading, Ri is the hypocentral distance, $I(\varpi)$ is the instrumental frequency characteristic, $e^{-\frac{\varpi Ri}{2v_p Q}}$ represents the absorption by the medium, and v_p is the P-wave velocity. In order to determine the Q value, two frequencies ω_1 and ω_2 are substituted into Equation (16) to find the frequency ratio:

$$\ln \left| \frac{Ai(\omega_1)}{Ai(\omega_2)} \right| = \ln \left| \frac{Ai_0(\omega_1)}{Ai_0(\omega_2)} \right| - \frac{(\omega_1 - \omega_2) Ri}{2v_p Q} \quad (17)$$

In this equation $(\omega_1 - \omega_2) Ri / (2v_p Q)$ is a constant and the $\ln |Ai_0(\omega_1) / Ai_0(\omega_2)|$ value of different recorded earthquakes can also be treated as a constant, if these earthquakes have occurred in the same area and if their magnitudes are close to each other. Thus, the Q values can be directly calculated from Equation (17), which accounts for the features of a different medium before and after the earthquakes.

1.3.2 Width of Fourier Spectrum

The width of Fourier spectrum is defined as the bandwidth. This represents the complexity of seismic waves and is computed for 70% of the maximum spectral amplitude. A wider Fourier spectrum indicates that the seismic waves have more frequency components; therefore, the rupture process should be more complicated and the medium and stress distribution should be more uneven at the hypocenter.

1.4 Data Processing

In this study, the clearly-recorded seismograms with appropriate amplitudes are scanned and digitized through the seismogram digitization and database management system (SDDMS) (Liu et al., 2001). Next, the ranges of the corner frequency f_{ca} for different earthquakes are estimated by using empirical methods, and the window length T is set as 8–10 times the reciprocal of the minimum corner frequency (i.e., $1/(f_{ca})_{\min}$) to improve the resolution of the frequency spectrum. The sampling step size Δt is set as less than $1/(f_{ca})_{\max}$ to avoid the high-frequency aliasing and the resolution is kept as 300 dpi. The digitized records are then connected by lines and re-sampled for an equal time interval. Afterwards, a Hanning window and fast Fourier transform (FFT) are applied to process these records, and the spectra of seismic waves is then obtained after the instrument and medium calibrations. The Hanning window $W(t)$ is taken as

$$W(t) = \begin{cases} \frac{1}{2T} \left(1 + \cos \frac{\pi t}{T} \right) & 0 \leq t \leq T \\ 0 & t < 0 \end{cases} \quad (18)$$

The theoretical frequency characteristic curves of the instruments corresponding to the seismograms are used for the instrument calibration and the characteristic of the medium frequency, $B(\omega)$, is expressed as

$$B(\omega) = 2 \exp \left(-\frac{|\omega| r}{2v_p Q} + i \frac{\omega r}{2\pi v_p Q} \ln \left(\left(\frac{\omega}{\omega_0} \right)^2 - 1 \right) \right) \quad (19)$$

where the low cutoff frequency ω is taken as 0.25 Hz and the quality factor Q is taken as 400. Finally, the rupture characteristics of small earthquakes and the ambient shear stress are determined by the methods illustrated above. The Q values of P-waves are estimated directly from the recorded wave spectrum by applying the methods presented above. The time instants of the peaks and troughs in P- or S-waves are measured from the SDDMS (Liu et al., 2001) and the temporal periodicity waveform is then determined by using Equation (15). Similarly, the width of Fourier spectrum is also obtained from the SDDMS.

2. Analysis of Liyang M 6.0 Earthquake

2.1 Analysis of Rupture Characteristics

Table 1 lists the calculated results of the rupture characteristics of medium and small earthquakes that have occurred before and after the Liyang M 6.0 earthquake. In our study, the earthquakes that have occurred within three years before the main shock are selected to represent the “abnormal” earthquakes that occur during the earthquake preparation process in a seismogenic zone. Further, those earthquakes that have occurred over a long time after the main shock (13 years in the case of Liyang earthquake) are selected to represent the “normal” earthquakes for comparison. It is assumed that this time lag allows the seismogenic zone to return to its normal status after a mid-strong earthquake.

It may be observed in Table 1 that the parameter L_0/L varies from 0.5 to 1.0. Further, it may be mentioned that λ s and σ s denote the azimuths of primary rupture directions and their root-mean-square errors (RMSEs), respectively (λ and σ values are not used, if three or more possible primary rupture directions have been found), and that n is the number of seismic observatories. The certainty factor (CF) of the primary rupture direction is defined as $CF = 1$ when $\sigma \leq 15^\circ$ and only one primary rupture direction

has been determined, CF = II when $15^\circ < \sigma \leq 30^\circ$ and only one primary rupture direction has been determined, and CF = III when two possible primary directions have been found.

Table 1: Rupture Characteristics of Medium and Small Earthquakes That Occurred before and after Liyang M 6.0 Earthquake

| No. | Date | Time | Longitude | Latitude | M_L | L_0/L | λ_1, σ_1 ($^\circ$) | λ_2, σ_2 ($^\circ$) | n | CF |
|----------------------------------|------------|-------|-----------|----------|-------|---------|---------------------------------------|---------------------------------------|-----|-----|
| Before Liyang M 6.0 earthquake | | | | | | | | | | |
| 1 | 1977-05-10 | 11:56 | 119°13' | 31°58' | 4.6 | 0.95 | | | 5 | |
| 2 | 1977-09-10 | 21:35 | 117°56' | 32°59' | 2.8 | 1.0 | 331.4, 22.5 | | 3 | II |
| 3 | 1977-11-08 | 21:05 | 117°30' | 32°00' | 2.6 | 0.87 | 317, 8.7 | | 4 | I |
| 4 | 1977-11-28 | 05:22 | 116°53' | 32°45' | 2.1 | 1.0 | | | 2 | |
| 5 | 1978-01-28 | 13:01 | 117°32' | 32°11' | 2.8 | 1.0 | 205.3, 12.1 | | 3 | I |
| 6 | 1978-01-28 | 13:48 | 117°37' | 32°11' | 3.1 | 0.88 | 290.8, 7.2 | 28.3, 7.2 | 5 | III |
| 7 | 1978-02-16 | 08:42 | 117°32' | 31°59' | 2.8 | 1.0 | | | 2 | |
| 8 | 1978-03-26 | 04:03 | 117°31' | 32°02' | 3.3 | 0.9 | 302.1, 9.4 | | 6 | I |
| 9 | 1978-03-26 | 20:51 | 118°43' | 33°15' | 3.6 | 0.88 | 309.1, 17.7 | | 7 | II |
| 10 | 1978-04-14 | 04:40 | 117°21' | 32°29' | 3.0 | 1.0 | | | 2 | |
| 11 | 1978-05-28 | 14:13 | 117°32' | 32°02' | 3.2 | 0.93 | 186.6, 5 | 116.6, 5 | 5 | III |
| 12 | 1978-06-25 | 04:34 | 119°17' | 31°27' | 3.0 | 1.0 | | | 2 | |
| 13 | 1978-07-06 | 11:44 | 120°57' | 32°43' | 3.7 | 0.93 | 303.4, 17.3 | | 5 | II |
| 14 | 1978-07-17 | 00:48 | 120°50' | 32°45' | 3.9 | 0.78 | 306.7, 19.7 | | 5 | II |
| 15 | 1978-07-17 | 00:52 | 120°59' | 32°46' | 3.3 | 0.73 | 42.7, 13.7 | | 4 | I |
| 16 | 1978-07-27 | 20:30 | 117°27' | 31°57' | 3.1 | 0.90 | 247.4, 15 | 352.4, 0 | 4 | III |
| 17 | 1978-11-24 | 23:38 | 117°27' | 32°22' | 3.3 | 0.70 | 212.7, 25 | | 4 | II |
| 18 | 1978-12-01 | 01:03 | 119°37' | 31°43' | 3.3 | 1.0 | 301, 30 | | 3 | II |
| 19 | 1978-12-19 | 08:07 | 119°00' | 32°22' | 2.8 | 1.0 | | | 2 | |
| 20 | 1978-12-23 | 10:53 | 117°36' | 32°10' | 3.3 | 1.0 | 214.2, 17.3 | | 4 | II |
| 21 | 1979-01-25 | 18:25 | 120°12' | 33°20' | 3.1 | 0.93 | 20.6, 7.5 | | 4 | I |
| 22 | 1979-04-16 | 05:27 | 117°04' | 32°57' | 2.2 | 1.0 | | | 2 | |
| 23 | 1979-04-28 | 09:15 | 121°27' | 32°53' | 3.0 | 1.0 | | | 2 | |
| After Liyang M 6.0 earthquake | | | | | | | | | | |
| 24 | 1992-01-25 | 06:37 | 119°51' | 31°55' | 3.2 | 0.76 | 45.7, 0 | | 6 | I |
| 25 | 1992-03-20 | 23:10 | 120°04' | 32°08' | 2.8 | 0.90 | 199.7, 7.2 | 327.2, 7.2 | 5 | III |
| 26 | 1992-05-29 | 16:33 | 120°38' | 33°29' | 3.3 | 1.0 | | | 2 | |
| 27 | 1992-06-27 | 07:35 | 117°46' | 32°30' | 3.0 | 1.0 | 243.3, 15 | 153.3, 15 | 4 | III |
| 28 | 1992-09-13 | 03:47 | 117°07' | 32°08' | 2.5 | 0.90 | 191.4, 0 | | 3 | I |
| 29 | 1992-10-25 | 17:46 | 120°34' | 32°45' | 3.5 | 1.0 | 135.5, 12 | | 8 | I |

As shown in Table 1, there are 23 earthquakes that have occurred before the Liyang M 6.0 earthquake. Eleven of these (i.e., $\approx 47.8\%$) had the L_0/L values of 1.0, six earthquakes (i.e., $\approx 26.1\%$) had the L_0/L values between 0.90 and 0.99, three earthquakes (i.e., $\approx 13.0\%$) had the L_0/L values between 0.80 and 0.89, and the remaining three earthquakes ($\approx 13.0\%$) had the L_0/L values between

0.70 and 0.79. The average L_0/L value of the 23 earthquakes is 0.93. Among the six earthquakes that occurred after the Liyang earthquake, there were three earthquakes (i.e., 50%) that had the L_0/L values of 1.0, two earthquakes (i.e., $\approx 33.3\%$) had the L_0/L values between 0.90 and 0.99, and one earthquake (i.e., $\approx 16.7\%$) had the L_0/L value between 0.70 and 0.79. The average L_0/L value of these six earthquakes is also 0.93. Thus, there has been no obvious change in the average L_0/L value from that before the Liyang earthquake to that after the earthquake.

In Table 1, the M 4.6 earthquake occurred on May 10, 1977, i.e., two years before the Liyang earthquake, and had the L_0/L value of 0.95, which is very close to that for the unilateral rupture. The epicentral distance of this earthquake was 60 km. Until the occurrence of the Liyang earthquake, no earthquake with magnitude higher than M 4.6 occurred in this area; therefore, the M 4.6 earthquake can be considered as the foreshock of the Liyang earthquake.

Figure 3 shows the primary rupture directions of the small and medium earthquakes on the seismogenic zone that occurred before the Liyang earthquake. Figure 4 displays the primary rupture directions of the other small and medium earthquakes that occurred in the same area. From Figure 3 it can be seen that the primary rupture directions of the earthquakes that occurred before the main shock are concentrated on several directions but most of those are pointing out from the gap. Figure 3 has been drawn manually and it only aims at showing all the directions pointing outwards. It may be seen from Table 1 that these directions are roughly parallel to the nodal planes of the main shock (Chen et al., 1997). However, as shown in Figure 4, the primary rupture directions of the earthquakes that occurred during the normal periods (i.e., the periods during which no earthquakes occurred and no anomalies were observed) are disorganized.

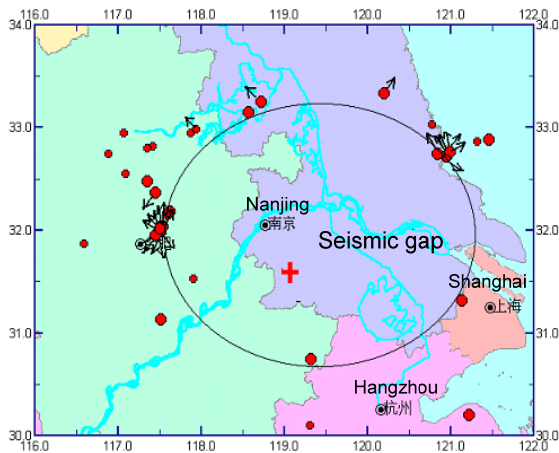


Fig. 3 Primary rupture directions of small and medium earthquakes on the seismogenic zone of the Liyang M 6.0 earthquake

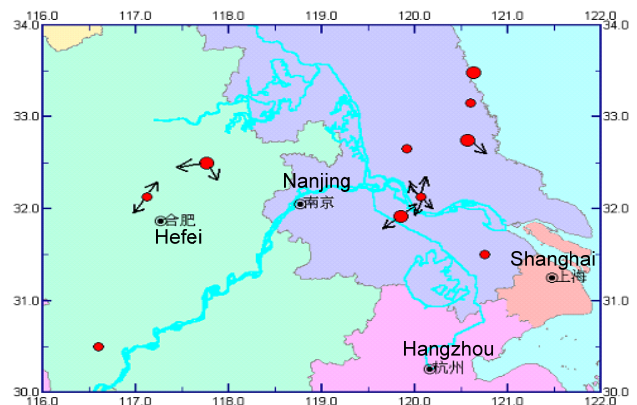


Fig. 4 Primary rupture directions of small and medium earthquakes that occurred during the normal periods in Liyang area

2.2 Calculation of Ambient Shear Stress, Temporal Periodicity of Waveform, Q Value and Width of Fourier Spectrum

The ambient shear stress τ , the temporal periodicity of waveform, r , Q value, and the width of Fourier spectrum, w , of small and medium earthquakes that occurred during the Liyang M 6.0 earthquake sequence are calculated and listed in Table 2. In this table, Q_1 refers to the Q values recorded on those locations where the epicentral distance was less than 130 km, and these values reflect the quality factors of a shallow medium. Q_2 refers to the Q values recorded on those locations where the epicentral distance was between 130 and 300 km, and these values represent the quality factors of a deep medium.

Table 2: τ , r , Q , w of Small and Medium Earthquakes That Occurred during Liyang M 6.0 Earthquake Sequence

| No. | Date | Time | Longitude | Latitude | M_L | τ (bar) | r ($\times 10^{-1}$) | Q_1 | Q_2 | w (Hz) |
|----------------------------------|------------|-------|-----------|----------|-------|-----------------|-----------------------------|-------|-------|-------------|
| Before Liyang M 6.0 earthquake | | | | | | | | | | |
| 1 | 1977-05-10 | 11:56 | 119°13' | 31°58' | 4.6 | 90.3 | 9.97 | | 283 | 0.26 |
| 2 | 1977-09-10 | 21:34 | 117°52' | 32°57' | 2.4 | 2.5 | 9.94 | 106 | | 0.10 |
| 3 | 1977-09-10 | 21:35 | 117°56' | 32°59' | 2.8 | 10.4 | 9.94 | 127 | | 0.10 |
| 4 | 1977-09-13 | 6:44 | 117°54' | 31°32' | 2.1 | 1.7 | 9.97 | 35 | | 0.11 |
| 5 | 1977-09-19 | 15:33 | 119°18' | 30°06' | 2.0 | 2.0 | 9.97 | 290 | | 0.25 |
| 6 | 1977-11-05 | 02:38 | 121°13' | 30°12' | 3.6 | 6.7 | 9.93 | | 299 | 0.66 |
| 7 | 1977-11-08 | 21:05 | 117°30' | 32°00' | 2.6 | 1.4 | 9.94 | 158 | 562 | 0.27 |
| 8 | 1977-11-26 | 17:39 | 119°10' | 31°21' | 2.0 | 0.9 | 9.87 | 153 | | 0.25 |
| 9 | 1977-11-28 | 05:22 | 116°53' | 32°45' | 2.1 | 1.2 | 9.84 | 157 | | 0.11 |
| 10 | 1978-01-05 | 18:41 | 121°08' | 31°19' | 3.0 | 7.0 | 9.98 | | 158 | 0.10 |
| 11 | 1978-01-28 | 13:01 | 117°32' | 32°11' | 2.8 | 8.2 | 9.74 | | 260 | 0.15 |
| 12 | 1978-01-28 | 13:48 | 117°37' | 32°11' | 3.1 | 8.7 | 9.99 | 206 | 176 | 0.18 |
| 13 | 1978-02-12 | 05:30 | 118°34' | 33°09' | 3.4 | 6.8 | 9.96 | | 351 | 0.22 |
| 14 | 1978-02-16 | 08:42 | 117°32' | 31°59' | 2.8 | 9.7 | 9.94 | 77 | 242 | 0.45 |
| 15 | 1978-03-26 | 04:03 | 117°31' | 32°02' | 3.3 | 8.4 | 9.96 | 46 | 275 | 0.20 |
| 16 | 1978-03-26 | 20:51 | 118°43' | 33°15' | 3.6 | 8.3 | 9.84 | | 576 | 0.21 |
| 17 | 1978-04-14 | 04:40 | 117°21' | 32°29' | 3.0 | 10.4 | 9.99 | | 260 | 0.42 |
| 18 | 1978-05-28 | 14:13 | 117°32' | 32°02' | 3.2 | 8.2 | 9.95 | | 381 | 0.27 |
| 19 | 1978-06-25 | 04:34 | 119°17' | 31°27' | 3.0 | 8.4 | 9.97 | | 353 | 0.22 |
| 20 | 1978-07-06 | 11:44 | 120°57' | 32°43' | 3.7 | 37.7 | 9.97 | | 408 | 0.23 |
| 21 | 1978-07-06 | 12:23 | 120°55' | 32°44' | 2.8 | 11.4 | 9.90 | | 353 | 0.10 |
| 22 | 1978-07-17 | 00:48 | 120°50' | 32°45' | 3.9 | 44.0 | 9.91 | | 472 | 0.20 |
| 23 | 1978-07-17 | 00:52 | 120°59' | 32°46' | 3.3 | 11.0 | 9.96 | | 371 | 0.60 |
| 24 | 1978-07-17 | 14:19 | 120°46' | 33°02' | 2.6 | 9.0 | 9.89 | | 371 | 0.60 |
| 25 | 1978-07-22 | 20:45 | 120°57' | 32°42' | 2.7 | 1.3 | 9.86 | | 175 | 0.36 |
| 26 | 1978-07-27 | 20:30 | 117°27' | 31°57' | 3.1 | 9.1 | 9.81 | 161 | 276 | 0.35 |
| 27 | 1978-08-07 | 04:51 | 121°19' | 32°53' | 2.6 | 1.9 | 9.54 | | 188 | 0.10 |
| 28 | 1978-08-27 | 22:32 | 119°22' | 31°36' | 2.1 | 1.9 | 9.83 | 57 | | 0.42 |
| 29 | 1978-10-02 | 04:04 | 120°31' | 32°03' | 2.7 | 1.6 | 9.95 | | 282 | 0.16 |
| 30 | 1978-10-21 | 11:19 | 117°31' | 31°08' | 3.1 | 9.3 | 9.89 | | 261 | 0.10 |
| 31 | 1978-11-05 | 13:12 | 117°05' | 32°33' | 2.7 | 2.0 | 9.99 | | 253 | 0.32 |
| 32 | 1978-11-17 | 22:31 | 119°44' | 31°41' | 2.7 | 2.1 | 9.98 | | 229 | 0.16 |
| 33 | 1978-11-18 | 07:52 | 119°40' | 31°43' | 2.7 | 1.1 | 9.70 | | 203 | 0.14 |
| 34 | 1978-11-24 | 23:38 | 117°27' | 32°22' | 3.3 | 12.4 | 9.98 | 317 | 478 | 1.10 |
| 35 | 1978-12-01 | 01:03 | 119°37' | 31°43' | 3.3 | 10.8 | 9.96 | | 450 | 0.11 |
| 36 | 1978-12-19 | 08:07 | 119°00' | 32°22' | 2.8 | 16.4 | 9.97 | 279 | 469 | 0.41 |
| 37 | 1978-12-23 | 10:53 | 117°36' | 32°10' | 3.3 | 13.7 | 9.98 | 194 | 257 | 0.38 |
| 38 | 1979-01-02 | 18:11 | 116°35' | 31°52' | 2.2 | 9.0 | 9.34 | | | 0.25 |

| | | | | | | | | | | |
|--------------------------------------|------------|-------|---------|--------|-----|------|------|-----|-----|------|
| 39 | 1979-01-25 | 18:25 | 120°12' | 33°20' | 3.1 | 10.4 | 9.97 | | 333 | 0.25 |
| 40 | 1979-02-17 | 02:42 | 117°25' | 32°49' | 2.1 | 9.0 | 9.61 | | | 0.25 |
| 41 | 1979-02-17 | 05:53 | 117°21' | 32°48' | 2.1 | 1.3 | 9.66 | | | 0.88 |
| 42 | 1979-03-07 | 05:08 | 119°19' | 30°45' | 3.9 | 54.6 | 9.88 | | | 0.10 |
| 43 | 1979-04-16 | 05:27 | 117°04' | 32°57' | 2.2 | 3.1 | 9.88 | 219 | | 0.28 |
| 44 | 1979-04-28 | 09:15 | 121°27' | 32°53' | 3.0 | 8.7 | 9.96 | | 230 | 0.39 |
| 45 | 1979-07-08 | 21:25 | 117°30' | 32°01' | 3.2 | 11.4 | 9.98 | | 380 | 0.38 |
| After Liyang <i>M</i> 6.0 earthquake | | | | | | | | | | |
| 46 | 1992-01-25 | 06:37 | 119°51' | 31°55' | 3.2 | 9.3 | 9.96 | | 423 | 0.21 |
| 47 | 1992-03-20 | 23:10 | 120°04' | 32°08' | 2.8 | 10.5 | 9.98 | | 364 | 0.15 |
| 48 | 1992-05-29 | 16:33 | 120°38' | 33°29' | 3.3 | 9.7 | 9.99 | | 417 | 0.14 |
| 49 | 1992-06-27 | 07:35 | 117°46' | 32°30' | 3.0 | 3.4 | 9.97 | | 349 | 0.64 |
| 50 | 1992-09-13 | 03:47 | 117°07' | 32°08' | 2.5 | 2.1 | 9.94 | 161 | 265 | 0.38 |
| 51 | 1992-09-15 | 10:10 | 120°45' | 31°30' | 2.9 | 12.7 | 9.94 | | 493 | 0.32 |
| 52 | 1992-09-23 | 09:37 | 116°36' | 30°30' | 2.6 | 1.4 | 9.97 | | 304 | 1.18 |
| 53 | 1992-10-13 | 17:59 | 120°06' | 33°09' | 2.6 | 1.3 | 9.97 | | 203 | 0.16 |
| 54 | 1992-10-25 | 17:46 | 120°34' | 32°45' | 3.5 | 10.1 | 9.96 | | 383 | 0.16 |

Figure 5 shows the variation of the ambient shear stress during the Liyang earthquake sequence. From Table 2 and Figure 5, it may be observed that before the Liyang *M* 6.0 earthquake, the maximum shear stress was higher and that the ambient shear stress varied more violently. However, after the earthquake, the shear stress value stayed at a lower level and varied smoothly.

The variation of the temporal periodicity of waveform, *r*, is displayed in Figure 6. From this figure and Table 2, it may be seen that the temporal periodicity changed violently during the year preceding the Liyang *M* 6.0 earthquake (i.e., from August 7, 1978 to July 8, 1979) and that the minimum value of *r* is 0.934. However, during other periods, the temporal periodicity varied in the range 0.99±0.1.

The variations of *Q* values and the width of Fourier spectrum, *w*, are plotted in Figures 7–9. From these figures, it may be inferred that there were no obvious differences in the variations of *Q* and *w* before and after the Liyang earthquake. Further, as shown in Table 2, the *Q*₂ values are generally greater than the *Q*₁ values. This suggests that the quality factors of a deep medium are higher than those of a shallow medium.

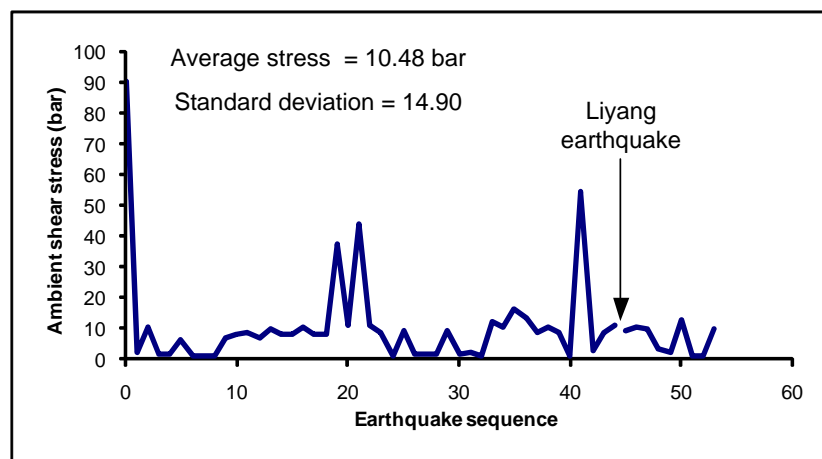


Fig. 5 Ambient shear stress τ of small and medium earthquakes in the Liyang *M* 6.0 earthquake sequence

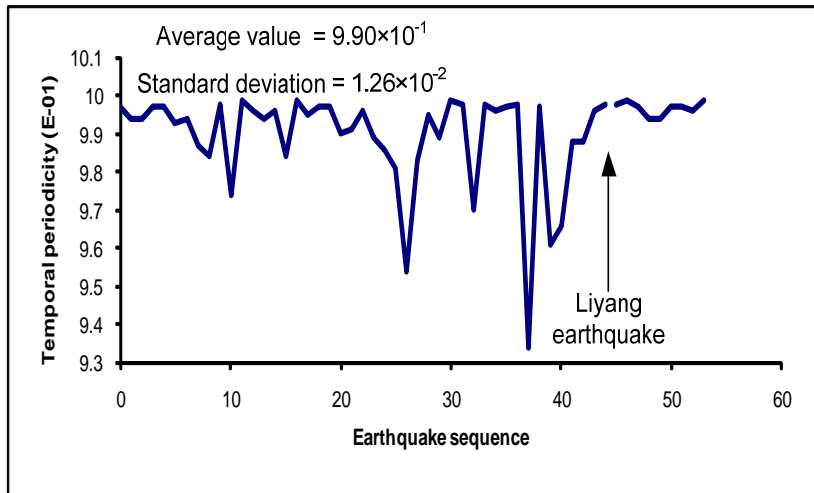


Fig. 6 Temporal periodicity of waveform, r , of small and medium earthquakes in the Liyang M 6.0 earthquake sequence

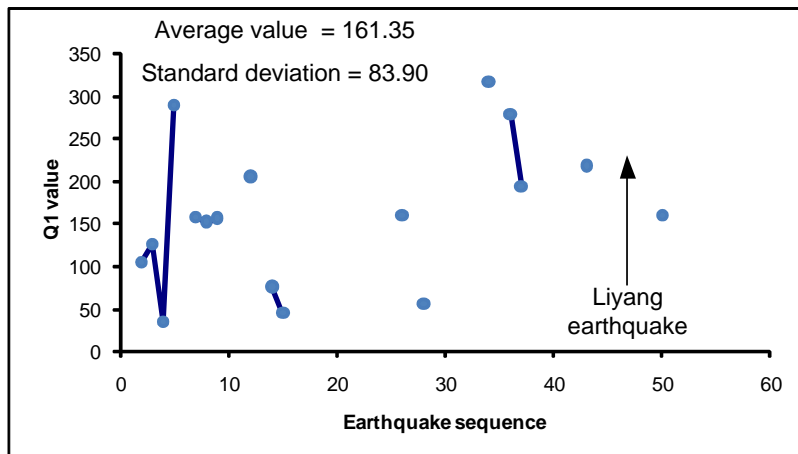


Fig. 7 Q_1 values of the P-waves of small and medium earthquakes in the Liyang M 6.0 earthquake sequence

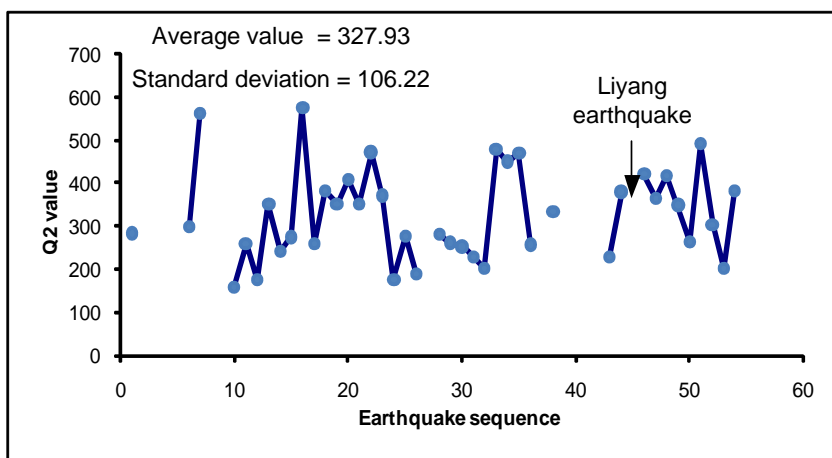


Fig. 8 Q_2 values of the P-waves of small and medium earthquakes in the Liyang M 6.0 earthquake sequence

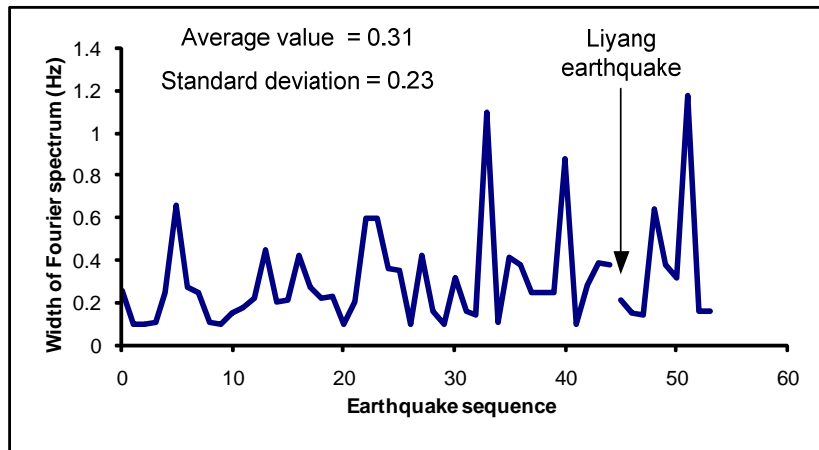


Fig. 9 Fourier spectral width w of small and medium earthquakes in the Liyang M 6.0 earthquake sequence

2.3 Discussion on Liyang M 6.0 Earthquake

Based on the above analyses, the following conclusions are drawn for the Liyang earthquake sequence:

1. The primary rupture directions of the earthquakes that occurred on the seismogenic zone were parallel to the nodal plane of the following main shock. Further, they were either tangent to the zone or pointed towards outside the zone. During the normal periods, the primary rupture directions were disorganized.
2. A few of the high ambient shear stress values and turbulent variations in the shear stress were observed over the year preceding the main shock, and in other times these values were lower and varied smoothly. As shown in Table 2, during the year preceding the Liyang earthquake, the mean stress value was 11.23 bar with the standard deviation of 16.13 bar, while after this earthquake, the mean stress value dropped to 6.72 bar and the standard deviation became 4.84 bar. The median stress value during the year preceding the Liyang earthquake was 9.05 bar and this value was reduced to 8.25 bar during other times.
3. The temporal periodicity of waveform, r , changed violently and several lower values appeared during the year preceding the main shock. The minimum value of r was 0.934. During the normal periods, r varied in the range 0.99 ± 0.01 .
4. The M 4.6 earthquake occurred two years before the Liyang earthquake and its epicentral distance was 60 km. Until the occurrence of the main shock, no earthquake with magnitude higher than M 4.6 had occurred in this area. This earthquake was close to the unilateral rupture and its ambient shear stress value was much higher than that for the other earthquakes; therefore, this earthquake could be considered as the foreshock of the Liyang earthquake. Also, as shown in Figure 5, the ambient shear stress τ ($= 90.3$ bar) for the foreshock was much higher than the stress values for the other earthquakes.
5. No distinct regularity has been found for the variations in the rupture characteristic L_0/L , Q values for P-waves and width of Fourier spectrum before and after the Liyang M 6.0 earthquake.

3. Analysis of Heze M 5.9 Earthquake

3.1 Analysis of Rupture Characteristics

The rupture characteristics of the medium and small earthquakes that occurred before and after the Heze M 5.9 earthquake are listed in Table 3. From this table, the median L_0/L value for the four earthquakes preceding the Heze M 5.9 earthquake is calculated to be 0.91, and the average L_0/L value for the six earthquakes occurring after the Heze earthquake is obtained as 0.89. There is no obvious variation in the L_0/L value in the earthquakes before and after the Heze earthquake. It is also noticed that there are two earthquakes (M_L 4.6 earthquake on January 17, 1982, and M_L 4.8 earthquake on

May 29, 1982) with the L_0/L values of 1.0, which corresponds to the unilateral rupture, and with their occurrences before the Heze earthquake.

Table 3: Rupture Characteristics of Medium and Small Earthquakes That Occurred before and after Heze M 5.9 Earthquake

| No. | Date | Time | Longitude | Latitude | M_L | L_0/L | λ_1, σ_1 (°) | λ_2, σ_2 (°) | n | CF |
|--------------------------------|------------|-------|-----------|----------|-------|---------|------------------------------|------------------------------|-----|-----|
| Before Heze M 5.9 earthquake | | | | | | | | | | |
| 1 | 1981-12-23 | 06:27 | 115°26' | 35°36' | 4.6 | 1.0 | 287, 10 | | 3 | I |
| 2 | 1982-01-17 | 14:57 | 115°00' | 35°04' | 3.1 | 0.75 | 342.1, 0 | 352.1, 0 | 3 | III |
| 3 | 1982-05-29 | 18:28 | 114°57' | 36°58' | 4.8 | 1.0 | 200.4, 7.5 | 65.4, 7.5 | 3 | III |
| 4 | 1982-07-28 | 01:23 | 115°09' | 35°00' | 4.0 | 0.90 | 232.2, 11.3 | 284.7, 11.3 | 6 | III |
| After Heze M 5.9 earthquake | | | | | | | | | | |
| 5 | 1990-02-20 | 19:49 | 115°14' | 35°14' | 3.0 | 0.90 | 324.4, 11.0 | | 9 | I |
| 6 | 1990-07-12 | 07:39 | 115°22' | 35°20' | 3.0 | 0.93 | 222.7, 14.7 | | 5 | I |
| 7 | 1991-11-11 | 03:09 | 115°06' | 35°01' | 3.2 | 0.95 | 246.1, 4.6 | 311.1, 4.6 | 9 | III |
| 8 | 1993-12-03 | 03:49 | 115°25' | 35°21' | 3.0 | 0.90 | 236.8, 9.8 | | 8 | I |
| 9 | 1994-08-28 | 22:04 | 115°26' | 35°16' | 2.6 | 0.77 | 208.4, 7.5 | 313.4, 7.5 | 4 | III |
| 10 | 1995-04-14 | 10:56 | 115°44' | 35°51' | 2.7 | 0.90 | 189.1, 5 | 289.1, 5 | 4 | III |

Figure 11 shows the primary rupture directions of the small and medium earthquakes that occurred on the seismic belt before the Heze earthquake. Only three samples are available for these earthquakes and two of those had two possible primary rupture directions in each case. In Figure 11 it is observed that one of the possible primary rupture directions of the two samples is consistent with the primary rupture direction of the third sample, which is assumed as the primary rupture direction. Thus, the primary rupture directions of the earthquakes on the seismic belt are conjugated to the direction of the seismic belt and are close to the direction of the Heze fault (Zhang et al., 1990a, 1990b). As indicated by Zhang et al. (1990a, 1990b), this direction is also along the direction of the primary rupture plane of the Heze M 5.9 earthquake (i.e., NW with azimuth 114°). Figure 12 displays the primary rupture directions of the other small and medium earthquakes that occurred in the same area during the normal periods. No obvious difference is seen in the rupture directions shown in Figures 10 and 11.

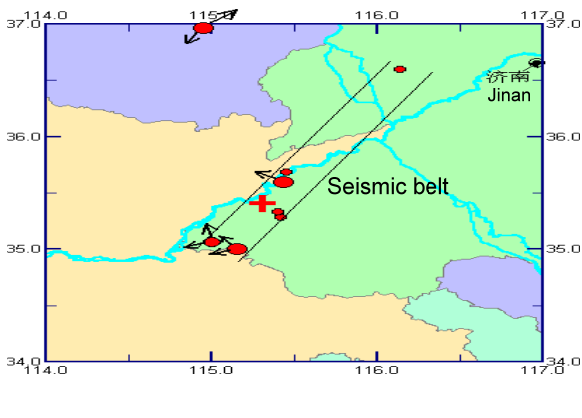


Fig. 10 Primary rupture directions of small and medium earthquakes that occurred on the seismic belt before the Heze M 5.9 earthquake

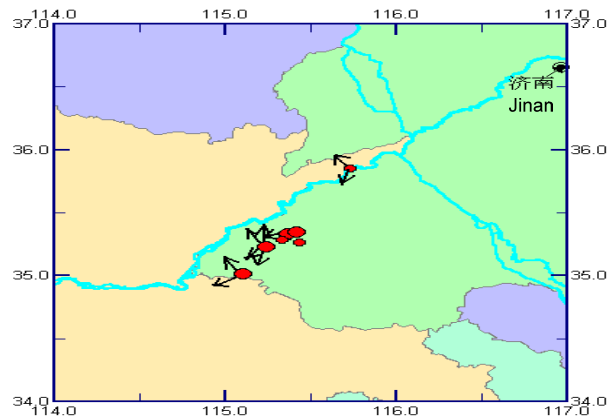


Fig. 11 Primary rupture directions of small and medium earthquakes that occurred during the normal periods in the Heze area

3.2 Calculation of Ambient Shear Stress, Temporal Periodicity of Waveform, Q Value and Width of Fourier Spectrum

Table 4 lists the ambient shear stress τ , the temporal periodicity of waveform, r , Q value, and the width of Fourier spectrum, w , of the small and medium earthquakes that occurred during the Heze M 5.9 earthquake sequence. Figure 12 shows the variation of ambient shear stress during the Heze M 5.9 earthquake sequence. From this figure and Table 4, it can be seen that similar to the Liyang earthquake, the shear stress had more and higher peak values and varied more violently before the Heze M 5.9 earthquake. As shown in Table 4, during the year and half preceding the Heze earthquake, the mean stress value was 45.17 bar with the standard deviation of 52.92 bar, and after the earthquake, the mean stress value dropped to 24.74 bar and the standard deviation became 54.85 bar. While after the earthquake, the shear stress value stayed at a lower level, it varied smoothly. It is also observed that there are two earthquakes whose shear stress values were much higher than the others. Those earthquakes are (i) the M 4.6 earthquake that occurred on December 23, 1981 and whose τ value was 170.7 bar, and (ii) the M 4.8 earthquake that occurred on May 29, 1982 and whose τ value was 104.1 bar. Both earthquakes were the cases of unilateral rupture, with the L_0/L value equal to 1.0. The M 4.6 earthquake occurred two years before the Heze earthquake and its epicentral distance was only 50 km. Further, until the occurrence of the Heze earthquake, this was the strongest earthquake that had occurred within a 100-km radius and the second strongest earthquake that had occurred within a 200-km radius. Therefore, the M 4.6 earthquake is considered as the foreshock of the Heze earthquake.

Table 4: τ, r, Q, w of Small and Medium Earthquakes That Occurred during Heze M 5.9 Earthquake Sequence

| No. | Date | Time | Longitude | Latitude | M_L | τ (bar) | r ($\times 10^{-1}$) | Q_2 | w (Hz) |
|--------------------------------|------------|-------|-----------|----------|-------|-----------------|-----------------------------|-------|-------------|
| Before Heze M 5.9 earthquake | | | | | | | | | |
| 1 | 1981-12-23 | 06:27 | 115°26' | 35°36' | 4.6 | 170.7 | 9.98 | 287 | 0.66 |
| 2 | 1982-01-17 | 14:57 | 115°00' | 35°04' | 3.1 | 7.1 | 9.93 | 282 | 0.52 |
| 3 | 1982-01-22 | 23:19 | 116°08' | 36°36' | 2.5 | | 9.97 | | |
| 4 | 1982-04-09 | 08:31 | 115°27' | 35°41' | 2.1 | | 9.88 | | |
| 5 | 1982-05-29 | 18:28 | 114°57' | 36°58' | 4.8 | 104.1 | 9.98 | 260 | 0.87 |
| 6 | 1982-07-21 | 19:33 | 115°25' | 35°17' | 2.6 | 1.7 | 9.99 | 301 | 0.25 |
| 7 | 1982-07-26 | 10:34 | 115°24' | 35°20' | 2.4 | | 9.90 | | |
| 8 | 1982-07-28 | 01:23 | 115°09' | 35°00' | 4.0 | 29.7 | 9.98 | 353 | 0.53 |
| After Heze M 5.9 earthquake | | | | | | | | | |
| 9 | 1990-02-20 | 19:49 | 115°14' | 35°14' | 3.0 | 7.2 | 9.98 | 354 | 0.65 |
| 10 | 1990-06-18 | 09:18 | 115°21' | 35°18' | 2.5 | | 9.85 | | |
| 11 | 1990-07-12 | 07:39 | 115°22' | 35°20' | 3.0 | 11.0 | 9.97 | 487 | 0.62 |
| 12 | 1991-11-11 | 03:09 | 115°06' | 35°01' | 3.2 | 10.5 | 9.98 | 437 | 0.95 |
| 13 | 1993-12-03 | 03:49 | 115°25' | 35°21' | 3.0 | 9.6 | 9.96 | 427 | 0.80 |
| 14 | 1994-08-28 | 22:04 | 115°26' | 35°16' | 2.6 | 2.0 | 9.94 | 310 | 0.89 |
| 15 | 1995-02-16 | 21:35 | 115°20' | 35°17' | 2.6 | 2.2 | 9.95 | 344 | 0.28 |
| 16 | 1995-04-14 | 10:56 | 115°44' | 35°51' | 2.7 | 2.4 | 9.97 | 323 | 0.14 |

Figure 13 shows the variation of the temporal periodicity of waveform, r . From this figure and Table 4, it is seen that r varied smoothly between 0.99 and 1.00. Due to the missing of earthquake samples that occurred during the year preceding the Heze earthquake (i.e., from November, 1982 to November, 1983), no violent variation has been observed in r during the Heze earthquake sequence.

The variations of Q_2 and width of Fourier spectrum, w , are displayed in Figures 14 and 15, respectively. These figures show that there were no obvious differences in the variations of Q_2 and w before and after the Heze earthquake.

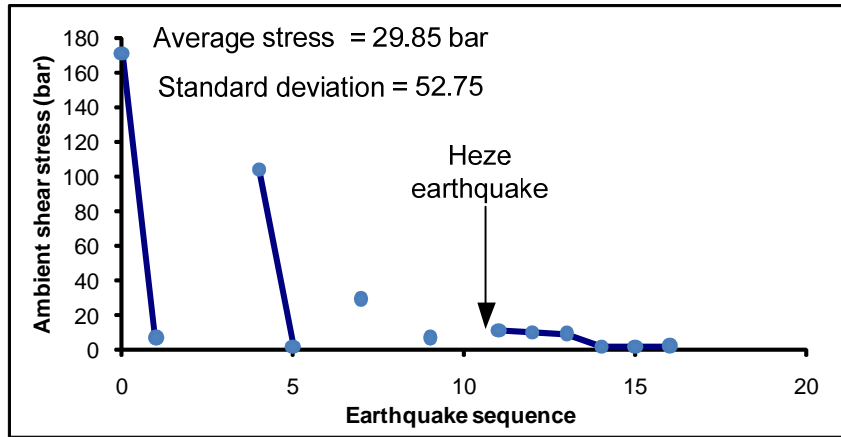


Fig. 12 Ambient shear stress τ of small and medium earthquakes in the Heze M 5.9 earthquake sequence

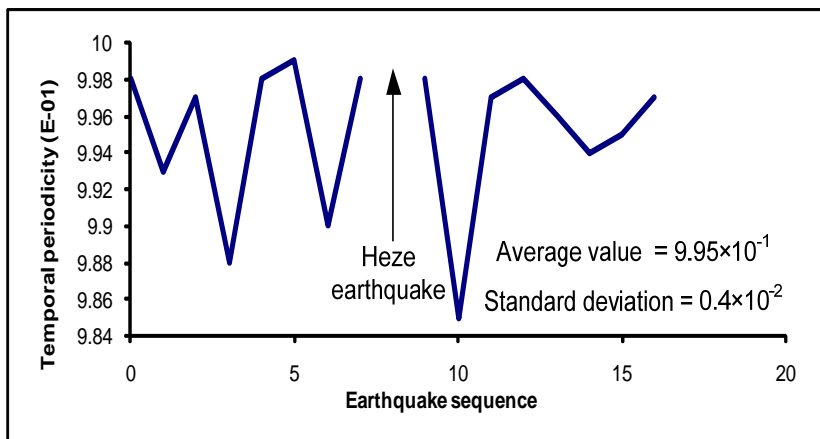


Fig. 13 Temporal periodicity of waveform, r , of small and medium earthquakes in the Heze M 5.9 earthquake sequence

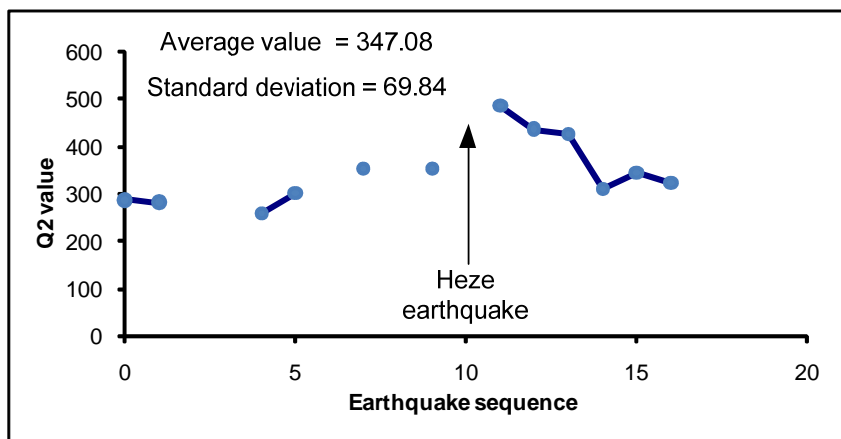


Fig. 14 Q_2 values of the P-waves of small and medium earthquakes in the Heze M 5.9 earthquake sequence

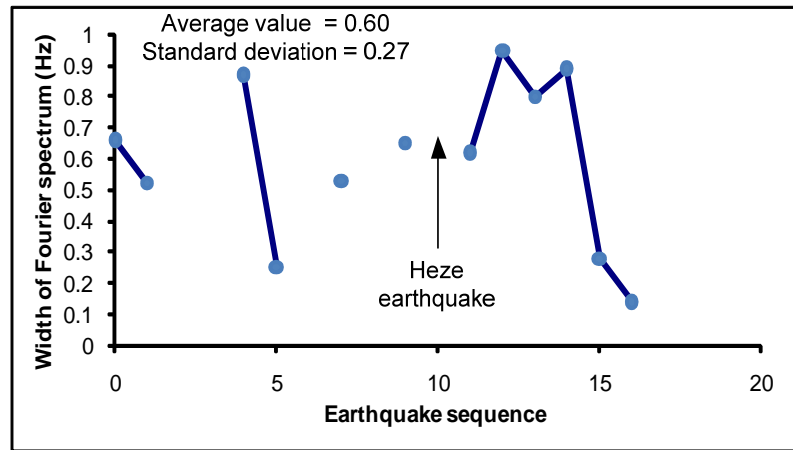


Fig. 15 Fourier spectral width w of small and medium earthquakes in the Heze M 5.9 earthquake sequence

3.3 Discussion on Heze M 5.9 Earthquake

Based on the analysis of the above data, following conclusions are drawn for the Heze earthquake sequence:

1. The primary rupture directions of the earthquakes that occurred on the Heze seismic belt are conjugated to the direction of the belt and are close to the direction of the Heze fault. These directions also coincide with the direction of the primary rupture plane of the Heze M 5.9 earthquake (Zhang et al., 1990a, 1990b).
2. A few of the high ambient shear stress values and turbulent variations in the shear stress took place during the period of year and a half preceding the main shock, and in other times, the shear stress was lower and varied smoothly. As shown in Table 4, during the year preceding the Heze earthquake, the mean stress value was 45.17 bar with the standard deviation of 52.92 bar, while after that earthquake, the mean stress value dropped to 24.74 bar and the standard deviation became 54.85 bar. The phenomenon of higher ambient shear stress before the Heze earthquake is also reflected in the median value of the ambient shear stress. The median stress value in the period of year and a half preceding the main shock was 29.7 bar, as against 7.2 bar during the other times. This proves that in the case of the Heze earthquake, the ambient shear stress was much higher before the main shock compared to that after the main shock.
3. The value of the temporal periodicity of waveform, r , was high and it varied smoothly in the range 0.99 ± 0.01 . Due to the missing of the earthquake samples that occurred in the year preceding the Heze earthquake (i.e., from November, 1982 to November, 1983), there was neither a violent variation nor a low value in r was observed.
4. The M 4.6 earthquake occurred two years before the Heze earthquake (i.e., on December 23, 1981) and its epicentral distance was 50 km. Until the occurrence of the Heze earthquake, this was the strongest earthquake that had occurred within a 100-km radius and the second strongest one that had occurred within a 200-km radius. Therefore, this earthquake is considered as the foreshock of the Heze earthquake. Similarly, the ambient shear stress τ ($= 170.7$ bar) for this earthquake (i.e., the foreshock) was much higher than the other stress values.
5. The earthquakes that occurred before the main shock were closer to a unilateral rupture than the earthquakes that occurred after it. The median r for the four events before the main shock is 0.95, and for the six events afterwards this is 0.90. However, such a difference in r is not obvious, and the mean r is 0.91 for the four events before the main shock and 0.89 for the six events afterwards.
6. No regularity has been evident in the variations of the Q values for P-waves and the width of Fourier spectrum before and after the Heze M 5.9 earthquake.

4. Analysis of Southern Yellow Sea M 6.2 Earthquake

4.1 Analysis of Rupture Characteristics

Table 5 lists the calculated results on the rupture characteristics of the medium and small earthquakes that occurred before and after the southern Yellow Sea M 6.2 earthquake. From this table, the average L_0/L value of thirteen earthquakes that occurred before the southern Yellow Sea earthquake is calculated as 0.92. Among these earthquakes, five earthquakes had the L_0/L value of 1.0, five earthquakes had the L_0/L value between 0.90 and 0.99, two earthquakes had the L_0/L value between 0.80 and 0.89, and one earthquake had the L_0/L value between 0.70 and 0.79. The average L_0/L value of the four earthquakes that occurred after the southern Yellow Sea earthquake is 0.90. For two of these earthquakes, the L_0/L values are located between 0.90 and 0.99 and for the other two earthquakes, the L_0/L values are located between 0.80 and 0.89. Comparatively, the earthquakes that occurred before the main shock were a little bit closer to the case of unilateral rupture than the earthquakes that occurred after the main shock, but such a difference was not supported by the other results. This implies that the occurrence of small earthquakes with unilateral rupture is not sufficient but only a necessary condition for the medium and strong earthquakes to occur.

Table 5: Rupture Characteristics of Medium and Small Earthquakes That Occurred before and after Southern Yellow Sea M 6.2 Earthquake

| No. | Date | Time | Longitude | Latitude | M_L | L_0/L | λ_1, σ_1 ($^\circ$) | λ_2, σ_2 ($^\circ$) | n | CF |
|---|------------|-------|-----------|----------|-------|---------|---------------------------------------|---------------------------------------|-----|-----|
| Before southern Yellow Sea M 6.2 earthquake | | | | | | | | | | |
| 1 | 1978-07-06 | 11:44 | 120°57' | 32°43' | 3.7 | 1.0 | 14.8, 0 | 134.8, 0 | 4 | III |
| 2 | 1978-07-17 | 22:48 | 120°50' | 32°45' | 3.9 | 0.90 | 47.4, 8.5 | 138.9, 8.8 | 5 | III |
| 3 | 1979-01-04 | 18:28 | 120°30' | 33°50' | 4.3 | 1.0 | 120.7, 5.8 | | 4 | I |
| 4 | 1981-01-11 | 21:30 | 120°36' | 33°34' | 3.7 | 0.95 | 155.9, 5.2 | 220.9, 5.2 | 7 | III |
| 5 | 1983-09-10 | 07:47 | 122°29' | 34°14' | 3.5 | 0.73 | | | 5 | |
| 6 | 1983-09-25 | 14:30 | 120°07' | 32°51' | 3.5 | 0.94 | 238.8, 11.6 | | 9 | I |
| 7 | 1983-10-07 | 19:38 | 122°19' | 34°26' | 3.7 | 0.80 | 229.4, 17.3 | | 3 | II |
| 8 | 1983-10-11 | 22:36 | 121°20' | 34°35' | 3.9 | 1.0 | 313.9, 4.3 | 220.5, 4.3 | 10 | III |
| 9 | 1983-10-14 | 05:00 | 121°16' | 34°40' | 3.3 | 1.0 | 313.9, 15 | 223.9, 15 | 4 | III |
| 10 | 1983-10-19 | 14:25 | 121°25' | 33°49' | 4.1 | 0.96 | 233.3, 12.4 | | 8 | I |
| 11 | 1984-05-16 | 17:16 | 120°35' | 33°05' | 3.6 | 0.93 | 213.7, 14.0 | | 7 | I |
| 12 | 1984-05-17 | 11:56 | 120°30' | 33°05' | 3.3 | 1.0 | 36.1, 13.2 | 221.1, 22.9 | 6 | III |
| 13 | 1984-05-17 | 11:59 | 120°30' | 33°05' | 3.4 | 0.80 | 198.6, 7.5 | 333.6, 7.5 | 4 | III |
| After southern Yellow Sea M 6.2 earthquake | | | | | | | | | | |
| 14 | 1992-05-29 | 16:33 | 120°38' | 33°29' | 3.3 | 0.93 | 226.8, 15 | 24.3, 22.5 | 4 | III |
| 15 | 1992-08-19 | 07:49 | 120°58' | 33°40' | 3.0 | 0.97 | 25.7, 15 | | 4 | I |
| 16 | 1992-08-25 | 03:21 | 121°42' | 34°12' | 4.1 | 0.86 | 232.6, 11.2 | | | I |
| 17 | 1992-10-25 | 17:46 | 120°34' | 32°45' | 3.5 | 0.83 | 135.4, 8.6 | | 12 | I |

Figure 16 shows the primary rupture directions of the small and medium earthquakes on the seismogenic zone that occurred before the southern Yellow Sea earthquake. From this figure, it is observed that the candidate primary rupture directions are either tangent to the edge of the gap or are

pointing outside the gap. Such characteristics are very similar to those of the earthquakes that occurred on the Liyang seismic gap.

Figure 17 displays the primary rupture directions of the small and medium earthquakes that occurred on the seismic belt before the southern Yellow Sea earthquake. From this figure, it is seen that most primary rupture directions are consistent with the direction of this seismic belt and are pointed south-west (SW) except for the following three earthquakes: the M_L 3.3 earthquake that occurred at 11:56 hours on May 17, 1984; the M_L 3.4 earthquake that occurred at 11:59 hours on May 17, 1984; and the M_L 3.3 earthquake that occurred at 5:00 hours on October 14, 1983. Each of the three earthquakes have two candidate primary rupture directions and one of those directions is pointed SW. The other rupture direction of the first earthquake is pointed northeast (NE), and the other rupture directions of the other two earthquakes is pointed northwest (NW) and is conjugated to the direction of this seismic belt. As stated in Chen et al. (2002), for this seismic belt, the azimuth of the nodal plane 1 is 350° and the azimuth of the nodal plane 2 is 77° . Based on the distribution of the plotted primary rupture directions, the nodal plane 2 is determined to be the primary rupture plane that extends in the north-east (NE) direction.

The primary rupture directions of the small and medium earthquakes that occurred in the same area (i.e., the seismic belt for the southern Yellow Sea earthquake) during the normal periods are plotted in Figure 18. These directions point either SW or NE, which is approximately consistent with the direction of the belt.

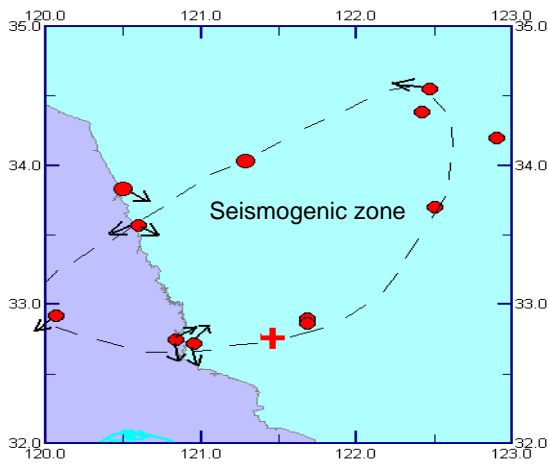


Fig. 16 Primary rupture directions of small and medium earthquakes on the seismogenic zone of the southern Yellow Sea M 6.2 earthquake

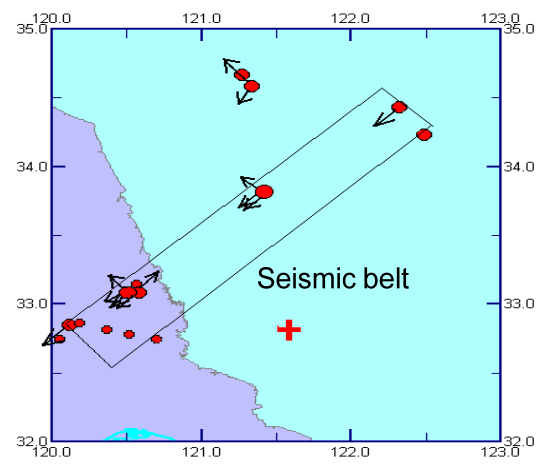


Fig. 17 Primary rupture directions of small and medium earthquakes that occurred on the seismic belt before the southern Yellow Sea M 6.2 earthquake

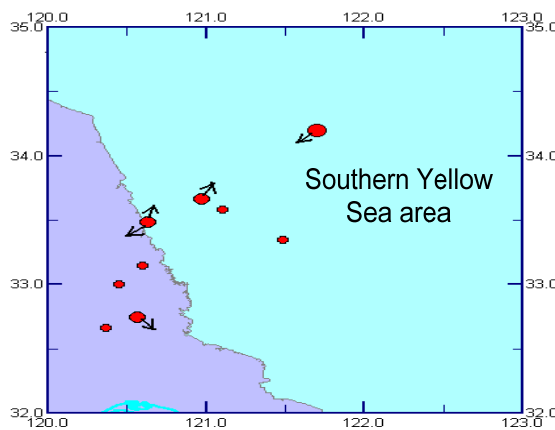


Fig. 18 Primary rupture directions of small and medium earthquakes that occurred during the normal periods in the southern Yellow Sea area

4.2 Calculation of Ambient Shear Stress, Temporal Periodicity of Waveform, Q Value and Width of Fourier Spectrum

The ambient shear stress τ , the temporal periodicity of waveform, r , Q value, and the width of Fourier spectrum, w , of the small and medium earthquakes that occurred before and after the southern Yellow Sea M 6.2 earthquake are listed in Table 6.

Table 6: τ , r , Q , w of Small and Medium Earthquakes That Occurred during the Southern Yellow Sea M 6.2 Earthquake Sequence

| No. | Date | Time | Longitude | Latitude | M_L | τ (bar) | r ($\times 10^{-1}$) | Q_1 | Q_2 | w (Hz) |
|---|------------|-------|-----------|----------|-------|-----------------|-----------------------------|-------|-------|-------------|
| Before southern Yellow Sea M 6.2 earthquake | | | | | | | | | | |
| 1 | 1975-12-30 | 12:00 | 121°17' | 34°02' | 4.3 | 8.6 | 9.99 | | | 5.10 |
| 2 | 1976-04-15 | 00:19 | 121°41' | 32°54' | 3.7 | 19.3 | 9.96 | | 545 | 0.42 |
| 3 | 1977-02-21 | 18:21 | 122°28' | 34°33' | 3.8 | 16.2 | 9.99 | | | 0.39 |
| 4 | 1977-06-09 | 00:49 | 122°25' | 34°23' | 3.6 | 3.4 | 9.94 | | 445 | 1.59 |
| 5 | 1977-07-25 | 05:25 | 122°30' | 33°42' | 3.6 | 4.0 | 9.99 | | 451 | 0.42 |
| 6 | 1978-01-24 | 04:16 | 122°54' | 34°12' | 3.8 | 29.7 | 9.91 | | | 0.26 |
| 7 | 1978-07-06 | 11:44 | 120°57' | 32°43' | 3.7 | 41.0 | 9.98 | | | 2.91 |
| 8 | 1978-07-17 | 22:48 | 120°50' | 32°45' | 3.9 | 53.0 | 9.92 | | 513 | 2.56 |
| 9 | 1979-01-04 | 18:28 | 120°30' | 33°50' | 4.3 | 49.0 | 9.92 | | 511 | 0.10 |
| 10 | 1979-04-16 | 18:49 | 121°41' | 32°52' | 3.6 | 9.4 | 9.98 | | 477 | 0.40 |
| 11 | 1981-01-11 | 21:30 | 120°36' | 33°34' | 3.7 | 46.8 | 9.98 | | 482 | 1.70 |
| 12 | 1983-09-10 | 07:47 | 122°29' | 34°14' | 3.5 | 9.3 | 9.97 | | | 2.32 |
| 13 | 1983-09-25 | 14:30 | 120°07' | 32°51' | 3.5 | 11.1 | 9.99 | | 549 | 0.74 |
| 14 | 1983-10-07 | 19:38 | 122°19' | 34°26' | 3.7 | 50.9 | 9.97 | | 689 | 1.60 |
| 15 | 1983-10-11 | 22:36 | 121°20' | 34°35' | 3.9 | 67.0 | 9.99 | | 492 | 1.49 |
| 16 | 1983-10-14 | 05:00 | 121°16' | 34°40' | 3.3 | 13.0 | 9.99 | | 393 | 2.03 |
| 17 | 1983-10-19 | 14:25 | 121°25' | 33°49' | 4.1 | 57.6 | 9.97 | | | 2.71 |
| 18 | 1983-11-20 | 08:15 | 120°03' | 32°45' | 2.2 | 2.8 | 9.98 | | | 1.04 |
| 19 | 1984-03-07 | 23:10 | 120°22' | 32°49' | 2.5 | | 9.63 | | | |
| 20 | 1984-03-20 | 04:01 | 120°42' | 32°45' | 2.5 | 2.3 | 9.83 | 209 | 302 | 0.45 |
| 21 | 1984-03-20 | 04:01 | 120°31' | 32°47' | 2.8 | 5.7 | 9.94 | | 257 | |
| 22 | 1984-05-11 | 11:37 | 120°11' | 32°52' | 2.5 | 1.3 | 9.98 | | 306 | 0.23 |
| 23 | 1984-05-15 | 22:52 | 120°34' | 33°09' | 2.7 | | 9.96 | | | |
| 24 | 1984-05-16 | 17:16 | 120°35' | 33°05' | 3.6 | 7.9 | 9.98 | | 521 | 2.60 |
| 25 | 1984-05-17 | 11:56 | 120°30' | 33°05' | 3.3 | 10.6 | 9.97 | | 551 | 2.89 |
| 26 | 1984-05-17 | 11:59 | 120°30' | 33°05' | 3.4 | 9.9 | 9.98 | | 487 | 1.36 |
| After southern Yellow Sea M 6.2 earthquake | | | | | | | | | | |
| 27 | 1992-01-27 | 18:34 | 120°22' | 32°40' | 2.5 | 2.0 | 9.98 | | 316 | 3.97 |
| 28 | 1992-02-08 | 07:46 | 121°06' | 33°35' | 2.6 | | 9.86 | | | |
| 29 | 1992-03-12 | 06:13 | 120°27' | 33°00' | 2.8 | 15.1 | 9.99 | | 353 | 3.80 |
| 30 | 1992-05-29 | 16:33 | 120°38' | 33°29' | 3.3 | 11.8 | 9.88 | | 424 | 3.38 |
| 31 | 1992-08-19 | 07:49 | 120°58' | 33°40' | 3.0 | 12.1 | 9.94 | | 446 | 2.20 |

| | | | | | | | | | | |
|----|------------|-------|---------|--------|-----|------|------|--|-----|------|
| 32 | 1992-08-20 | 05:05 | 121°29' | 33°21' | 2.9 | 11.0 | 9.99 | | 499 | 1.93 |
| 33 | 1992-08-25 | 03:21 | 121°42' | 34°12' | 4.1 | 47.4 | 9.99 | | 617 | 1.71 |
| 34 | 1992-10-13 | 17:59 | 120°06' | 34°12' | 2.6 | 1.9 | 9.86 | | 331 | 1.48 |
| 35 | 1992-10-25 | 17:46 | 120°34' | 32°45' | 3.5 | 9.5 | 9.98 | | 486 | 2.73 |

Figure 19 shows the variation of ambient shear stress during the southeastern Yellow Sea M 6.2 earthquake sequence. Similar to the above two examples, it is found that the peak value of τ was higher and that the stress itself varied violently, especially during the eight months preceding the M 6.2 earthquake. During the other periods, the τ value was low and varied smoothly.

Figure 20 displays the variation of the temporal periodicity of waveform, r . From this figure and Table 6, it is seen that the temporal periodicity r varied smoothly within the range 0.99 ± 0.01 during the normal time periods and that it reached the lowest value of 0.963 two months before the main shock.

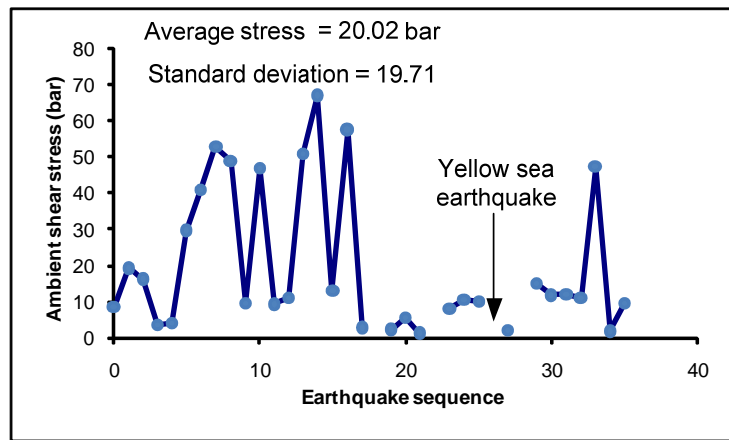


Fig. 19 Ambient shear stress τ of small and medium earthquakes in the southern Yellow Sea M 6.2 earthquake sequence

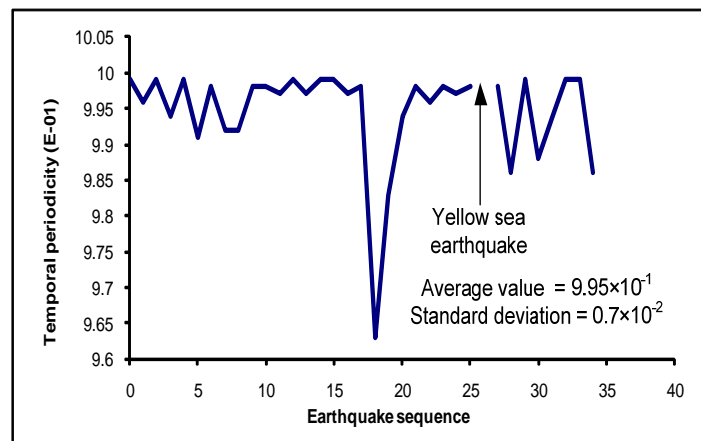


Fig. 20 Temporal periodicity of waveform, r , of small and medium earthquakes in the southern Yellow Sea M 6.2 earthquake sequence

Figures 21 and 22 respectively show the variations of Q_2 and the width of Fourier spectrum, w . From these variations, it is observed that there were no obvious differences in the variations of Q_2 and w before and after the southern Yellow Sea M 6.2 earthquake.

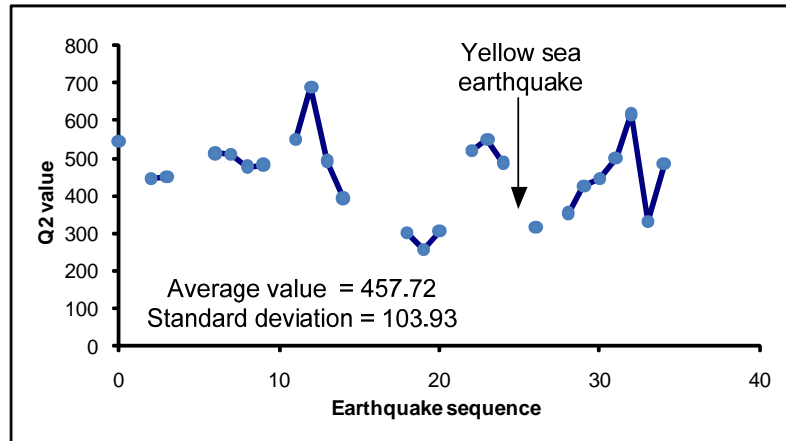


Fig. 21 Q_2 values of the P-waves of small and medium earthquakes in the southern Yellow Sea M 6.2 earthquake sequence

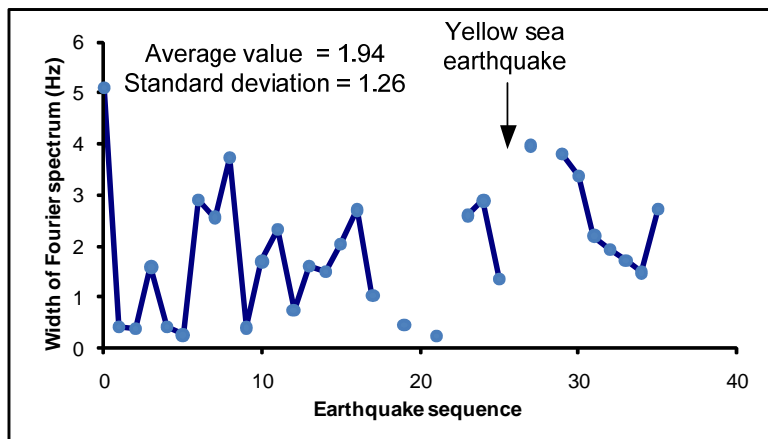


Fig. 22 Fourier spectral width w of small and medium earthquakes in the southern Yellow Sea M 6.2 earthquake sequence

4.3 Discussion on Southern Yellow Sea M 6.2 Earthquake

Based on the analysis of the above data, the following conclusions are drawn for the southern Yellow Sea earthquake sequence:

1. The primary rupture directions of the earthquakes that occurred on the seismogenic zone were parallel to the nodal plane of the following main shock, and they were either tangent to the zone or pointing towards outside the zone. However, during the normal periods, these directions were disorganized.
2. The primary rupture directions of the earthquakes that occurred on the seismic belt were close to the direction of the belt and were pointed SW. For an earthquake that occurred during the normal periods, the primary rupture direction was pointed SW or NE.
3. A few high values of ambient shear stress and turbulent variations in the shear stress were observed during the eight months preceding the main shock, while in other times, the shear stress value was lower and varied smoothly. According to Table 6, within the period of eight months preceding the main shock, the mean stress value was 25.17 bar with the standard deviation of 22.49 bar, while during the other times, the mean stress value was 12.48 bar and the standard deviation became 11.87 bar. However, the median stress value in the period of eight months preceding the main shock was only 9.9 bar and that value during the other times was 12.1 bar. Considering that the peak stress value before the main shock (i.e., 67 bar) is much higher than the peak stress during the other times (i.e., 53 bar), this phenomenon has accounted for the severe change in the ambient shear stress values before the main shock.

4. The temporal periodicity of waveform, r , changed violently and there was one really low value (of 0.96) observed within the period of two months before the main shock. During the normal periods, r varied smoothly within the range 0.99 ± 0.01 .
5. The earthquakes that occurred before the main shock were a little bit closer to a unilateral rupture than the earthquakes that occurred after it, but such a difference in L_0/L is not obvious. As shown in Table 5, the median r for the 13 events before the main shock is 0.95, and for the four events afterwards this is 0.90. However, such a difference in r is not obvious, and the mean r is 0.92 for the 13 events before the main shock and 0.90 for the four events afterwards.
6. There has been no obvious regularity in the variations for the Q values of P-waves and the widths of Fourier spectra before and after the southern Yellow Sea M 6.2 earthquake.

5. Analysis of M 6.1 and M 6.2 Earthquakes in Northern Gulf

5.1 Analysis of Rupture Characteristics

The rupture characteristics of the medium and small earthquakes that occurred before and after the northern Gulf earthquakes are shown in Table 7. From this table, the average L_0/L value of the eleven small and medium earthquakes preceding the northern Gulf earthquakes is obtained as 0.91 and the average L_0/L value of the five earthquakes that occurred afterwards is obtained as 0.89. Comparatively, the earthquakes that occurred before the main shocks were closer to a unilateral rupture than the earthquakes that occurred after the main shocks, but this difference was not supported by the other results.

Table 7: Rupture Characteristics of Medium and Small Earthquakes That Occurred before and after the Northern Gulf M 6.1, M 6.2 Earthquakes

| No. | Date | Time | Longitude | Latitude | M_L | L_0/L | λ_1, σ_1 (°) | λ_2, σ_2 (°) | n | CF |
|---|------------|-------|-----------|----------|-------|---------|------------------------------|------------------------------|-----|-----|
| Before northern Gulf M 6.1, M 6.2 earthquakes | | | | | | | | | | |
| 1 | 1991-03-09 | 12:45 | 110°46' | 21°12' | 2.9 | 1.0 | | | 2 | |
| 2 | 1992-01-12 | 10:42 | 109°42' | 20°51' | 2.1 | 1.0 | | | 2 | |
| 3 | 1992-10-28 | 10:13 | 109°50' | 21°22' | 2.6 | 1.0 | | | 2 | |
| 4 | 1993-02-22 | 03:49 | 110°52' | 19°42' | 2.9 | 1.0 | 344.4, 0 | | 3 | I |
| 5 | 1993-03-05 | 04:29 | 109°30' | 21°20' | 2.8 | 1.0 | | | 2 | |
| 6 | 1993-10-11 | 10:58 | 107°55' | 21°52' | 2.7 | 0.75 | | | 3 | |
| 7 | 1994-02-12 | 09:24 | 109°42' | 21°55' | 3.4 | 1.0 | | | 3 | |
| 8 | 1994-09-06 | 22:27 | 110°29' | 21°03' | 2.4 | 0.70 | | | 2 | |
| 9 | 1994-10-02 | 19:34 | 108°24' | 20°53' | 2.8 | 0.60 | | | 2 | |
| 10 | 1994-10-24 | 10:10 | 110°28' | 20°50' | 3.1 | 1.0 | 60.4, 13.2 | | 5 | I |
| 11 | 1994-12-28 | 15:26 | 108°32' | 21°36' | 2.8 | 1.0 | | | 2 | |
| After northern Gulf M 6.1, M 6.2 earthquakes | | | | | | | | | | |
| 12 | 1999-03-12 | 18:37 | 109°24' | 20°33' | 2.8 | 1.0 | | | 2 | |
| 13 | 1999-06-06 | 09:54 | 109°52' | 20°58' | 2.9 | 1.0 | 50.3, 22.9 | | 3 | II |
| 14 | 1999-06-30 | 16:41 | 109°22' | 20°34' | 3.2 | 0.72 | 234.1, 22.9 | 54.1, 22.9 | 6 | III |
| 15 | 1999-07-06 | 16:46 | 110°14' | 20°32' | 3.6 | 0.90 | 214.4, 17.3 | | 5 | II |
| 16 | 1999-10-30 | 04:31 | 110°31' | 20°52' | 3.2 | 0.83 | | | 5 | |

In this area, there are only a few earthquakes whose primary rupture directions have been determined. Those primary rupture directions are close to each other and point either SW or NE (see Figure 23). As stated by Chen et al. (2002), no seismogenic zone or seismic belt had been found in this area before the northern Gulf M 6.1 and M 6.2 earthquakes.

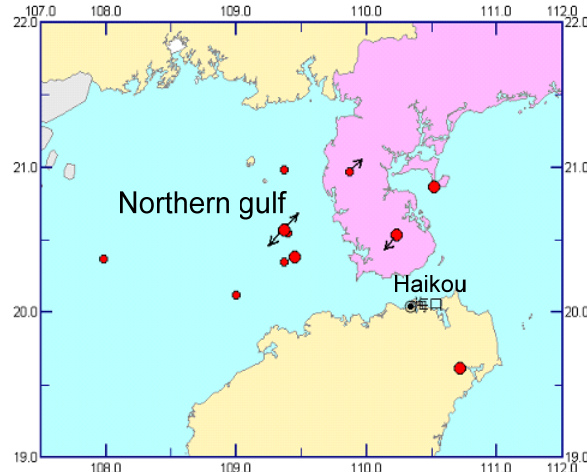


Fig. 23 Primary rupture directions of small and medium earthquakes that occurred during the normal periods in northern Gulf area

5.2 Calculation of Ambient Shear Stress, Temporal Periodicity of Waveform, Q Value and Width of Fourier Spectrum

The ambient shear stress τ , the temporal periodicity of waveform, r , Q value, and the width of Fourier spectrum, w , of the small and medium earthquakes that occurred before and after the northern Gulf M 6.1 and M 6.2 earthquakes are listed in Table 8.

Table 8: τ , r , Q , w of Small and Medium Earthquakes That Occurred during the Northern Gulf M 6.1 and M 6.2 Earthquakes Sequence

| No. | Date | Time | Longitude | Latitude | M_L | τ (bar) | r ($\times 10^{-1}$) | Q_1 | Q_2 | w (Hz) |
|---|------------|-------|-----------|----------|-------|-----------------|-----------------------------|-------|-------|-------------|
| Before northern Gulf M 6.1, M 6.2 earthquakes | | | | | | | | | | |
| 1 | 1991-03-09 | 12:45 | 110°46' | 21°12' | 2.9 | 16.2 | 9.82 | 111 | 267 | 0.31 |
| 2 | 1991-05-03 | 14:55 | 108°42' | 21°05' | 3.1 | 12.7 | 9.82 | | 289 | 0.37 |
| 3 | 1991-06-21 | 05:50 | 109°40' | 20°49' | 2.6 | | 9.67 | | | |
| 4 | 1991-10-29 | 01:55 | 108°05' | 21°38' | 2.4 | | 9.68 | | | |
| 5 | 1992-01-12 | 10:42 | 109°42' | 20°51' | 2.1 | 2.0 | 9.82 | 91 | | 0.36 |
| 6 | 1992-10-04 | 04:52 | 108°36' | 19°55' | 2.7 | 2.0 | 9.95 | | 424 | 0.12 |
| 7 | 1992-10-28 | 10:13 | 109°50' | 21°22' | 2.6 | 1.7 | 9.89 | 99 | 141 | 0.18 |
| 8 | 1992-12-16 | 03:22 | 108°28' | 21°21' | 2.2 | 2.8 | 9.96 | 276 | | 0.16 |
| 9 | 1993-01-13 | 18:20 | 108°34' | 21°42' | 2.2 | | 9.39 | | | |
| 10 | 1993-02-22 | 03:49 | 110°52' | 19°42' | 2.9 | 12.7 | 9.98 | | 262 | 0.48 |
| 11 | 1993-03-05 | 04:29 | 109°30' | 21°20' | 2.8 | 10.6 | 9.97 | 191 | 217 | 0.20 |
| 12 | 1993-03-13 | 18:04 | 108°38' | 21°47' | 2.3 | | 9.61 | | | |
| 13 | 1993-06-25 | 18:54 | 108°37' | 21°44' | 2.2 | | 9.87 | | | |
| 14 | 1993-10-11 | 10:58 | 107°55' | 21°52' | 2.7 | 2.0 | 9.97 | | 196 | 0.30 |
| 15 | 1994-01-02 | 19:34 | 108°24' | 20°53' | 2.8 | 13.4 | 9.92 | | 359 | 0.41 |
| 16 | 1994-02-12 | 09:24 | 109°42' | 21°55' | 3.4 | 9.1 | 9.97 | 238 | 449 | 0.21 |
| 17 | 1994-09-06 | 22:27 | 110°29' | 21°03' | 2.4 | 2.3 | | 72 | 187 | 0.27 |
| 18 | 1994-10-24 | 10:10 | 110°28' | 20°50' | 3.1 | 11.5 | 9.97 | 94 | 287 | 0.43 |

| | | | | | | | | | | |
|--|------------|-------|---------|--------|-----|------|------|--|-----|------|
| 19 | 1994-12-28 | 15:26 | 108°32' | 21°36' | 2.8 | 15.4 | 9.93 | | 412 | 0.34 |
| After northern Gulf <i>M</i> 6.1, <i>M</i> 6.2 earthquakes | | | | | | | | | | |
| 20 | 1999-01-02 | 16:09 | 107°59' | 20°22' | 2.6 | | 9.59 | | | |
| 21 | 1999-03-12 | 18:37 | 109°24' | 20°33' | 2.8 | 12.1 | 9.84 | | 219 | 0.22 |
| 22 | 1999-05-19 | 11:07 | 109°22' | 20°59' | 2.5 | | 9.58 | | | |
| 23 | 1999-06-06 | 09:54 | 109°52' | 20°58' | 2.9 | 12.9 | 9.83 | | 282 | 0.23 |
| 24 | 1999-06-30 | 16:41 | 109°22' | 20°34' | 3.2 | 10.8 | 9.96 | | 356 | 0.26 |
| 25 | 1999-07-06 | 16:46 | 110°14' | 20°32' | 3.6 | 9.9 | 9.99 | | 396 | 0.40 |
| 26 | 1999-08-29 | 03:42 | 109°27' | 21°23' | 3.0 | 13.2 | 9.94 | | 267 | 0.22 |
| 27 | 1999-08-31 | 16:29 | 109°00' | 20°07' | 2.7 | 2.0 | 9.93 | | 199 | 0.44 |
| 28 | 1999-10-25 | 17:46 | 120°34' | 32°45' | 3.5 | 9.5 | 9.98 | | 486 | 2.73 |
| 29 | 1999-10-30 | 04:31 | 110°31' | 20°52' | 3.2 | 12.1 | 9.97 | | 369 | 0.17 |
| 30 | 1999-12-10 | 06:11 | 110°43' | 19°37' | 3.1 | 12.7 | 9.93 | | 323 | 0.12 |
| 31 | 1999-12-11 | 21:53 | 109°22' | 20°21' | 2.5 | 2.5 | 9.93 | | 198 | 0.23 |

Figure 24 shows the variation of ambient shear stress τ in the northern Gulf *M* 6.1 and *M* 6.2 earthquake sequence. Similar to the previous samples, it is observed that the shear stress had more and higher peak values and that it varied violently during the year preceding the *M* 6.1 and *M* 6.2 earthquakes. However, during the other time periods, the shear stress remained low and varied smoothly.

Figure 25 shows the variation of the temporal periodicity of waveform, r , in the northern Gulf earthquake sequence. From this figure, it is observed that the temporal periodicity r was on the higher side and varied smoothly during most of the normal time periods (except during the first four earthquakes following the northern Gulf earthquakes), while it reached the lowest value of 0.939 and varied violently during the two years preceding the *M* 6.1 and *M* 6.2 earthquakes.

Figures 26–28 show the variations of Q values and the width of Fourier spectrum, w . From these figures, it is observed that similar to the previous samples, there are no obvious differences in the variations of Q_1 , Q_2 and w before and after the northern Gulf *M* 6.1 and *M* 6.2 earthquakes. The fact that the Q_2 values are higher than the Q_1 values again proves that the quality factors for a deep medium are higher than those for a shallow medium.

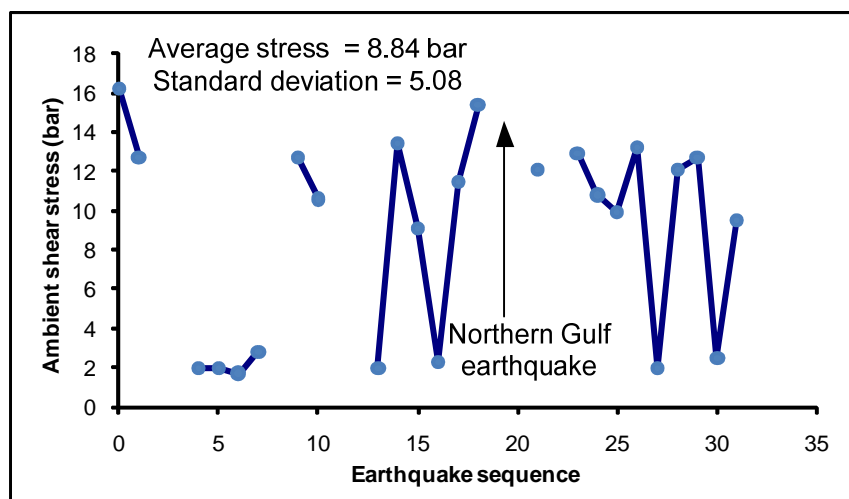


Fig. 24 Ambient shear stress τ of small and medium earthquakes in the northern Gulf *M* 6.1 and *M* 6.2 earthquakes sequence

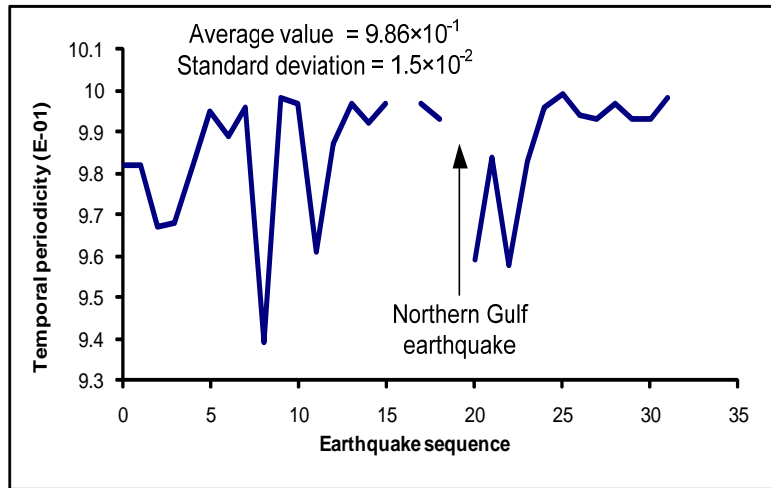


Fig. 25 Temporal periodicity of waveform, r , of small and medium earthquakes in the northern Gulf M 6.1 and M 6.2 earthquakes sequence

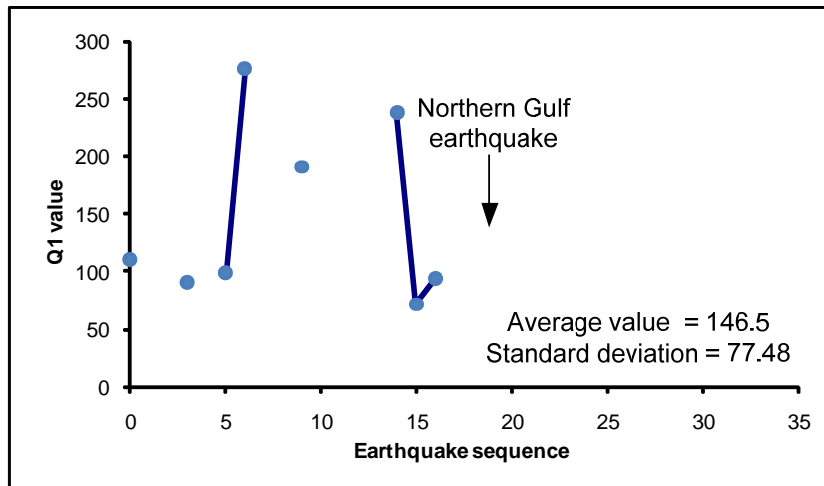


Fig. 26 Q_1 values of the P-waves of small and medium earthquakes in the northern Gulf M 6.1 and M 6.2 earthquakes sequence

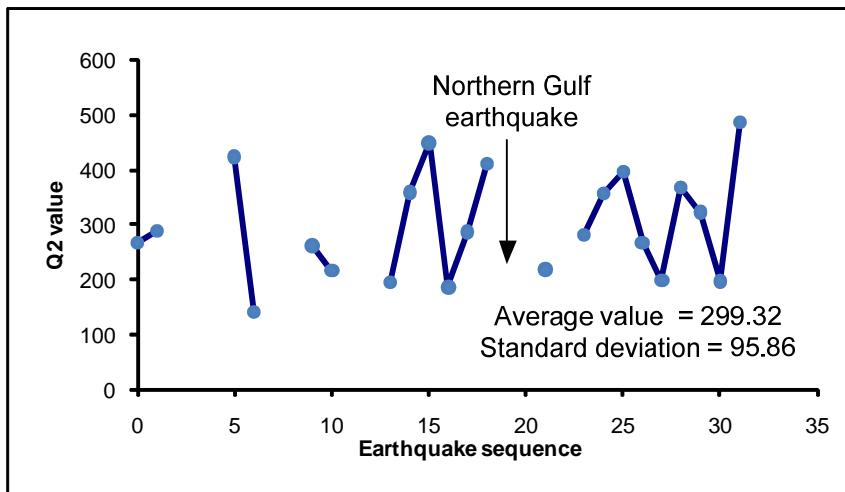


Fig. 27 Q_2 values of the P-waves of small and medium earthquakes in the northern Gulf M 6.1 and M 6.2 earthquakes sequence

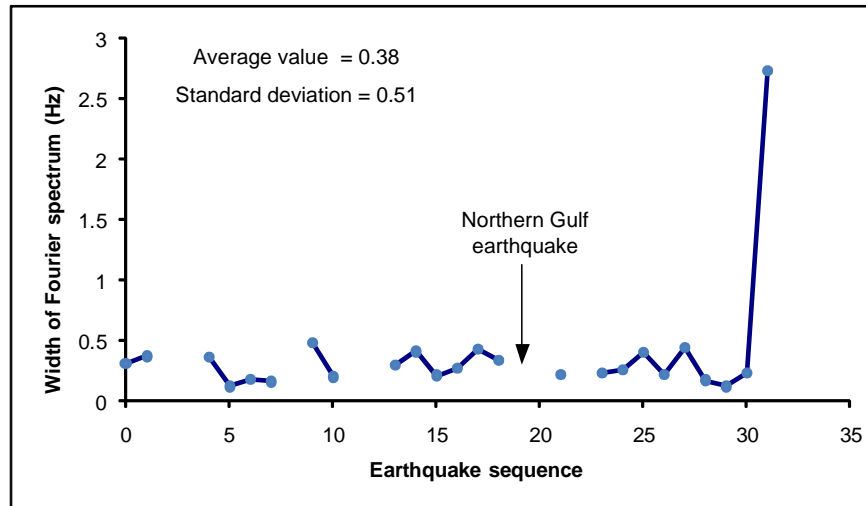


Fig. 28 Fourier spectral width w of small and medium earthquakes in the northern Gulf M 6.1 and M 6.2 earthquakes sequence

5.3 Discussion on Northern Gulf M 6.1 and M 6.2 Earthquakes

On investigating the parameters listed in Tables 7 and 8, following observations have been made for the northern Gulf earthquake sequence:

1. The primary rupture directions of the earthquakes that occurred in the northern Gulf area were close to each other and were pointed SW or NE.
2. A few of the high ambient shear stress values were observed before the main shocks. The mean stress value was 10.34 bar with the standard deviation of 5.70 bar during the year preceding the main shocks, while during the other times, the mean stress value was 8.44 bar and the standard deviation was 4.16 bar. This trend was even reflected in the median stress values, with the median stress value being 11.5 bar during the year preceding the main shocks and 10.6 bar during the other times.
3. The temporal periodicity of waveform, r , changed a little bit more evidently and several lower values of r were observed within the period of two years preceding the main shocks. The minimum value observed was 0.939. However, r varied smoothly during the normal time periods. Whereas the standard deviation of r was 0.02 within the two-year period before the main shocks, this was only 0.013 in the other times.
4. The earthquakes that occurred before the main shocks were closer to a unilateral rupture (i.e., L_0/L was closer to 1.0) than the earthquakes that occurred after them, but such a difference in L_0/L is not obvious. From Table 7, the median r for the 11 events before the main shocks is obtained as 1, and for the five events afterwards this is obtained as 0.9. However, such a difference in r is not obvious, and the mean r is 0.91 for the 11 events before the main shocks and 0.89 for the four events afterwards.
5. No regularity has been evident in the variations of the Q values of P-waves and the width of Fourier spectrum before and after the northern Gulf M 6.1 and M 6.2 earthquakes. Also, it has not been possible to obtain the Q values after the main shocks because (1) most aftershocks were small earthquakes and could only be detected by local seismic stations, and the analog records mixed with P waves could hardly be used for digitization and spectral analysis, (2) in a certain amount of time after the main shocks and within the area around the epicenter, the ambient stress and Q values were in a severe adjustment disorder and it was impossible to use one data to represent the Q value in the whole area.

ERROR ESTIMATION

1. Errors in Determining Rupture Directions

1.1 Errors Caused by Digitization

Digitization is the representation of an original analog record $f(t)$ by a discrete set of points sampled at an equal time interval. The maximum error caused by this discretization, Δf , is

$$\Delta f = \frac{(\Delta t)^2}{8} |f''(x)|_{\max} + \frac{A}{2} \quad (20)$$

where A is the digitization precision (~ 0.05 mm). The resolution ratio of the scanner is 300 dpi and the dot pitch is 0.085 mm. On using Equation (20), it can be estimated that in our study, the error caused by the discretization Δf is about 1.1%.

1.2 Errors Caused by Simplified Hypocenter and Medium Model

In the asymmetric bilateral rupture model used in our studies, it is assumed that the focal depth is zero. Therefore, the radiation pattern factor R_α is simplified as $R_\alpha = \sin 2\theta \cos \varphi = \sin 2\theta$. If the actual focal depth is 15 km and the epicentral depth is 200 km, we have $\varphi = \tan^{-1}(15/200)$ and thus $R_\alpha = \sin 2\theta \cos \varphi = 0.9972 \sin 2\theta$. The relative error in this estimate is only 0.28%. Also, other errors caused by the uneven distribution of the quality factor (i.e., Q value) of the medium are eliminated because the generalized directional function is a ratio between two spectra.

1.3 Errors Generated in Plotting Generalized Directional Function Curves

As mentioned before, in determining the primary rupture directions of the above earthquake samples, we have chosen twelve θ values from 0° to 180° with the equal increment of 15° to calculate and plot the generalized directional function curves. This implies that the maximum error generated in the above process could be 15° , which is the major factor that causes errors in measuring rupture directions.

2. Errors in Evaluating Ambient Stress τ

In evaluating the ambient stress τ , it has been assumed that the average stress field is reduced to zero after an earthquake and that the yield strength of crust is the value of 200 MPa measured in laboratory. Besides the above assumptions, the precision in determining ambient stress is also influenced by the surface wave magnitude m_s and the hypocentral radius r_h .

2.1 Influence of m_s on Errors

On using Equation (5) and assuming $\nu = 0.252$, $\eta = 0.05$, and $\mu = 33$ GPa, we obtain

$$\tau = 10^{0.75m_s - 1.5 \log 2a - 0.77} \quad (21)$$

The allowable error in measuring m_s is 0.3, and hence the error of τ is

$$\tau + \Delta\tau = 10^{0.75(m_s + 0.3) - 1.5 \log 2a - 0.77} = 10^{0.75 \times 0.3} \tau = 1.7\tau \quad (22)$$

The relative error $\Delta\tau/\tau$ can be as large as 70%.

2.2 Influence of a on Errors

There are two types of errors in determining the hypocentral radius r . The first error is caused by the use of the mean value of $\sin \theta$ on the focal sphere for evaluating the radiation pattern factor expressed as

$$t_{2\alpha} = r_h \left(\frac{1}{v_f} + \frac{\sin \theta}{v_p} \right) \quad (23)$$

By using the mean value of $\sin \theta$ on the focal sphere, Equation (23) becomes

$$t_{2\bar{\alpha}} = r_h \left(\frac{1}{v_f} + \frac{\pi}{4v_p} \right) \quad (24)$$

Here, we use $v_f = 0.775 v_s$, and assume that $v_s = 3.38$ km/s (Wu et al., 1997) and $v_p = 5.7$ km/s (Giovambattista and Barba, 1997) within the crust. Also, we use \bar{r}_h to denote the hypocentral radius evaluated using the mean value of $\sin \theta$ on the focal sphere, $(r_h)_{\max}$ to denote the radius evaluated by using the maximum value of $\sin \theta$ equal to 1, and $(r_h)_{\min}$ to denote the radius evaluated by using the maximum value of $\sin \theta$ equal to 0. The range of error in determining r_h can be calculated as

$$\frac{|\bar{r}_h - (r_h)_{\max}|}{(r_h)_{\max}} = \frac{\left| \frac{t_{2\alpha}}{\frac{1}{v_f} + \frac{\pi}{4v_p}} - \frac{t_{2\alpha}}{\frac{1}{v_f} + \frac{1}{v_p}} \right|}{\frac{t_{2\alpha}}{\frac{1}{v_f} + \frac{1}{v_p}}} \approx 0.073 \quad (25)$$

$$\frac{|\bar{r}_h - (r_h)_{\min}|}{(r_h)_{\min}} = \frac{\left| \frac{t_{2\alpha}}{\frac{1}{v_f} + \frac{\pi}{4v_p}} - \frac{t_{2\alpha}}{1/v_f} \right|}{\frac{t_{2\alpha}}{1/v_f}} \approx 0.265 \quad (26)$$

From Equations (25) and (26), it is found that the relative error of r_h varies from 7.3% to 26.5%. From Equations (21) and (22), it can be determined that the relative error in τ caused due to using the average value of $\sin \theta$ (in determining the hypocentral radius r_h) varies from 2.0% to 13.7%.

Another type of error is caused by the estimation of the corner frequency f_{ca} . As shown in Equation (9), r_h can be estimated from f_{ca} . We choose the window length T as 4 s and then the resolution becomes 0.25 Hz. For an earthquake whose magnitude is about M 3.0 and whose epicentral distance is 200 km, the corner frequency f_{ca} will be around 2.5 Hz. Thus, the relative error of f_{ca} may become 0.1. On substituting this value into Equation (8), it is found that the resulting relative error in a will be $1/(1+0.1) \times 100\% \approx 9.1\%$. The consequent relative error in τ will be 2.7%. Based on the above discussion, it can be concluded that the error in evaluating the ambient stress τ is mainly caused by the error in estimating the earthquake magnitude m_s and that this error can be as much as 70%.

3. Summary

Based on the discussion in the last two sections, following conclusions are drawn:

1. The errors in determining the primary rupture directions are basically caused during the making of the generalized directional function plot. If the theoretical function curves are plotted versus θ at the interval of 15° , the maximum resultant error would be obtained as 15° .
2. The errors in evaluating the ambient stress τ are mainly caused by the error made in estimating the earthquake magnitude m_s . If the error caused in m_s is 0.3, the relative error caused in τ will be 70%.
3. The relative error in τ (between 2% and 14%) caused by using the mean value of $\sin \theta$ on the focal sphere may induce 7.3% to 26.5% error in the estimation of hypocentral radius r_h .

4. The use of f_{ca} to determine r_h generates a relative error of about 9.1%, which in turn leads to an error of 2% to 14% in determining the τ value.
5. The error due to digitization is about 1%, which may be considered acceptable.

CONCLUSIONS

This study has been based on four earthquake samples, which had the magnitudes of about 6.0 and which occurred in the southern and eastern China since 1970. Six seismic wave parameters of these earthquakes have been analyzed and compared in order to investigate the abnormal phenomena taking place before the earthquakes, such as seismogenic zones and seismic belts. These parameters include the rupture characteristic L_0/L , primary rupture direction, the ambient shear stress τ , the temporal periodicity of waveform r , the Q value of P-waves, and the width of Fourier spectrum, w . Based on the analyses and discussions on the four earthquake samples, following remarks have been concluded:

1. The primary rupture directions of the earthquakes occurring on seismogenic zones are parallel to the nodal plane of the following main shock and those either are tangent to the zone or point outside the zone. However, during the normal periods, the primary rupture directions are disorganized.
2. The primary rupture directions of the earthquakes occurring on seismic belts are either close to the direction of the belt or conjugated to it (i.e., close to the direction of the primary rupture plane of the main shock), and are pointed in the same direction. For an earthquake that occurs during the normal periods, the primary rupture direction of the earthquake becomes different for a different area.
3. The strongest earthquake that occurs within 100 km from where the main shock occurs and within two years preceding the main shock can be defined as the foreshock. It has been found in the case of the earthquake samples considered that the ambient shear stress of the foreshock is much higher than that for the other earthquakes that occur in the same time period and that the foreshock shows a unilateral rupture.
4. As observed from the first three earthquake samples, there have been a few high values of ambient shear stress as well as acute changes in the shear stress during the small and medium earthquakes that occurred in the year preceding the main shock and within 200 km from where the main shock occurred, while during the other time periods, the shear stress stayed lower and varied smoothly. Shear stress is also correlated with the ranges of the magnitudes of small and medium earthquakes that occur before and after a main shock. Such a correlation has been observed from Tables 2, 4, 6, 8 with corresponding values of earthquakes magnitudes and larger values of shear stress have been obtained for those earthquakes with magnitudes ranging from 3.7 to 4.6 that mainly occurred before the main shock. Further, lower shear stress values have been obtained for the weaker earthquakes with magnitudes ranging from 2.5 to 3.5, most of which occurred after the main shock.
5. Except for the Heze earthquake, it has been found that during the period of several months to two years preceding the main shock, the temporal periodicity of waveform, r , changes violently, or at least more evidently, and several lower values may appear. In the normal periods, however, r is high and changes gently. Such a phenomenon has not been observed for the Heze earthquake due to the recorded data missing for the year before the earthquake (i.e., from November, 1982 to November, 1983).
6. The earthquakes that occur before the main shock are closer to a unilateral rupture (i.e., L_0/L is closer to 1.0) than those earthquakes that occur after the main shock, but this difference is not so distinct.
7. There is no distinct regularity in the variations for the Q values of P-waves and the width of Fourier spectrum before and after the main shock.
8. The quality factors (i.e., Q values) of a deep medium are higher than those of a shallow medium.

A limitation of this study is that the temporal variations have not been considered. In future, advanced statistical approaches would need to be developed in order to validate our conclusions regarding the relationship between the eventual changes in the trends and the occurrence of main shocks. In that case, a precursor would need to be associated with some of the changes occurring before a main shock. Further, the above eight remarks have been concluded based on the study of the analog records of only the earthquake examples considered with a limited number of shocks. Later on, it will be desirable to take the

help of advanced monitoring instruments and more complete and precise digital records, and to analyze more earthquake samples by following a similar approach to validate our conclusions. A systematic statistical analysis on the complete digital seismic records will help us to justify the conclusions drawn from this study better and to acquire more reliable correlations between the seismic parameters and seismic activities.

REFERENCES

1. Chen, P.-S., Gu, J.-C. and Li, W.-X. (1977). "Study of Earthquake's Rupture Process and Prediction Applying Rupture Mechanics", Chinese Journal of Geophysics, Vol. 20, No. 3, pp. 185–201 (in Chinese).
2. Chen, P.-S., Zhuo, Y.-R., Jin, Y., Wang, Z.-G., Huang, W.-Q., Li, W.-X. and Hu, R.-S. (1978). "Stress Field of Beijing, Tianjin, Tangshan, and Zhangjiakou Area before and after Tangshan Earthquake", Chinese Journal of Geophysics, Vol. 21, No. 1, pp. 24–58 (in Chinese).
3. Chen, Q.-F., Zheng, D.-L. and Che, S. (editors) (2002). "Earthquake Cases in China (1992–1994)", Seismological Press, Beijing, China (in Chinese).
4. Davies, J., Sykes, L., House, L. and Jacob, K. (1981). "Shumagin Seismic Gap, Alaska Peninsula: History of Great Earthquakes, Tectonic Setting, and Evidence for High Seismic Potential", Journal of Geophysical Research: Solid Earth, Vol. 86, No. B5, pp. 3821–3855.
5. Dorel, J. (1981). "Seismicity and Seismic Gap in the Lesser Antilles Arc and Earthquake Hazard in Guadeloupe", Geophysical Journal of the Royal Astronomical Society, Vol. 67, No. 3, pp. 679–695.
6. Feng, D.-Y. and Yu, X.-J. (1994). "Application of Seismic Wave's Dynamic Characteristics in Short Term Earthquake Prediction", Earthquake, Vol. 1, pp. 12–22 (in Chinese).
7. Gaudemer, Y., Tapponnier, P., Meyer, B., Peltzer, G., Guo, S.-M., Chen, Z.-T., Dai, H.-G. and Cifuentes, I. (1995). "Partitioning of Crustal Slip between Linked, Active Faults in the Eastern Qilian Shan, and Evidence for a Major Seismic Gap, the 'Tianzhu Gap', on the Western Haiyuan Fault, Gansu (China)", Geophysical Journal International, Vol. 120, No. 3, pp. 599–645.
8. Giovambattista, R.D. and Barba, S. (1997). "An Estimate of Hypocentre Location Accuracy in a Large Network: Possible Implications for Tectonic Studies in Italy", Geophysical Journal International, Vol. 129, No. 1, pp. 124–132.
9. Kagan, Y.Y. and Jackson, D.D. (1991). "Seismic Gap Hypothesis: Ten Years After", Journal of Geophysical Research: Solid Earth, Vol. 96, No. B13, pp. 21419–21431.
10. Kagan, Y.Y. and Jackson, D.D. (1995). "New Seismic Gap Hypothesis: Five Years After", Journal of Geophysical Research: Solid Earth, Vol. 100, No. B3, pp. 3943–3959.
11. Kostoglodov, V., Singh, S.K., Santiago, J.A., Franco, S.I., Larson, K.M., Lowry, A.R. and Bilham, R. (2003). "A Large Silent Earthquake in the Guerrero Seismic Gap, Mexico", Geophysical Research Letters, Vol. 30, No. 15, Paper 1807.
12. Lahr, J.C. and Plafker, G. (1980). "Holocene Pacific-North American Plate Interaction in Southern Alaska: Implications for the Yakataga Seismic Gap", Geology, Vol. 8, No. 10, pp. 483–486.
13. Lidaka, T., Kato, A., Kurashimo, E., Iwasaki, T., Hirata, N., Katao, H., Hirose, I. and Miyamachi, H. (2009). "Fine Structure of P-Wave Velocity Distribution along the Atotsugawa Fault, Central Japan", Tectonophysics, Vol. 472, No. 1-4, pp. 95–104.
14. Liu, W.-L., Wu, P.-Z. and Chen, Y.-W. (1996). "Determination of Earthquake's Rupture Characteristics Using Directional Function", Earthquake Research in China, Vol. 12, No. 1, pp. 93–99 (in Chinese).
15. Liu, Z.-K., Wang, W., Zhang, R., Yu, N.-H., Zhang, T.-Z. and Pan, J.-Y. (2001). "A Seismogram Digitization and Database Management System", Acta Seismologica Sinica, Vol. 14, No. 3, pp. 333–341 (in Chinese).
16. Peacock, S., Crampin, S., Booth, D.C. and Fletcher, J.B. (1988). "Shear Wave Splitting in the Anza Seismic Gap, Southern California: Temporal Variations as Possible Precursors", Journal of Geophysical Research: Atmospheres, Vol. 93, No. B4, pp. 3339–3356.

17. Venkataraman, A. (2002). "Investigating the Mechanics of Earthquakes Using Macroscopic Seismic Parameters", Ph.D. Thesis, Division of Geological and Planetary Sciences, California Institute of Technology, Pasadena, U.S.A.
18. Wu, F.T., Levshin, A.L. and Kozhevnikov, V.M. (1997). "Rayleigh Wave Group Velocity Tomography of Siberia, China and the Vicinity", *Pure and Applied Geophysics*, Vol. 149, No. 3, pp. 447–473.
19. Zhang, Z.-C., Luo, L.-G., Li, H.-H., Chen, L.-D. and Li, X.-H. (editors) (1990a). "Earthquake Cases in China (1976–1980)", Seismological Press, Beijing, China (in Chinese).
20. Zhang, Z.-C., Luo, L.-G., Li, H.-H., Chen, L.-D. and Li, X.-H. (editors) (1990b). "Earthquake Cases in China (1981–1985)", Seismological Press, Beijing, China (in Chinese).